Electronic Supplementary Material (ESI) for Chemical Science.

Supplementary Information for

Temperature artifacts in protein structures bias ligand-binding predictions

Shanshan Y.C. Bradford [1,#], Léa El Khoury [2,#], Yunhui Ge [2], Meghan Osato [2], David L. Mobley [2,3], Marcus Fischer[1,4 *]

[1] Department of Chemical Biology & Therapeutics, St. Jude Children's Research Hospital, Memphis, TN 38105, USA.

[2] Department of Pharmaceutical Sciences, University of California, Irvine, CA 92697, USA.

[3] Department of Chemistry, University of California, Irvine, CA 92697, USA.

[4] Department of Structural Biology, St. Jude Children's Research Hospital, Memphis, TN 38105, USA.

# These authors contributed equally.

* correspondence to: marcus.fischer@stjude.org

Supplementary methods

Absolute binding free energy calculations.

A) System setup. Crystallographic structures of T4 lysozyme (L99A) bound to toluene (PDB code: 4W53), ethylbenzene (PDB code: 4W54), n-propylbenzene (PDB code: 4W55), n-butylbenzene (PDB code: 4W57), p-xylene (PDB code: 187L), o-xylene (PDB code: 188L), and iodobenzene (PDB code: 3DN4) [1] were downloaded from the RCSB Protein Data Bank (rcsb.org) [2]. We extracted the coordinates of the ligands (toluene, ethylbenzene, n-propylbenzene, n-butylbenzene, p-xylene, o-xylene, and iodobenzene) from the PDB structures of the respective L99A-ligand complexes. There are no crystal structures available in the RCSB Protein Data Bank for L99A complexed with 3-iodotoluene, 4-iodotoluene, and benzylacetate. Based on the concept that similar ligands are more likely to interact with the active site of a protein in a similar trend, we manually created benzylacetate in Chimera based on the bound structure of butylbenzene (PDB code: 4W57). The receptor structure prepared from the L99A:butylbenzene complex was used to form the L99A:benzylacetate complex. For 3-iodotoluene, we used a PDB file of the L99A:3-iodotoluene complex from a previous study by Gill et al. (9), where BLUES technique was used to sample and identify the binding modes of 3-iodotoluene. The resulting dominant binding mode was used in our study. For L99A:4-iodotoluene, we used the same PDB file of L99A:3-iodotoluene (Gill et al. [3]) for the receptor structure, and to generate the 3D structure of 4-iodotoluene based on that of 3-iodotoluene, using Chimera. Using the prepared PDB files of the receptors and the mol2 files of the ligands, the protein-ligand complexes were generated, parametrized, and solvated with YANK 0.17.0 (http://getyank.org/0.17.0).

Classical MD simulations to study the conformational change of L99A upon ligand binding.

In addition to binding free energy calculations, we performed a separate set of long MD simulations to study conformational changes of the protein. Our general protocol for MD simulations was described in the main text. Here we first give some additional details about our protocol for MD simulations, then we describe which specific systems we prepared, how they were set up, and details of our production simulations (from which we collected data for analysis).

A) MD simulations. During the NVT simulations (used to heat up the system from 10 to 278K or from 10 to 300K), we used Langevin dynamics with a collision frequency of 1 ps^{-1} to control the temperature. Production simulations (lengths specified below) were done in the NPT ensemble; the temperature was

controlled through Langevin dynamics and a constant pressure was maintained using Monte Carlo barostat. During heating, equilibration, and production simulations, we used the hydrogen mass repartitioning (HMR) approach [4, 5] with a simulation step of 4 fs. Long-range electrostatic interactions were calculated using the particle mesh Ewald method, with a cutoff of 10 Å for the real space electrostatics and Lennard-Jones forces.

B) Systems setup. We carried out MD simulations on the different protein-ligand sets described below:

a) MD simulations on L99A complexes (100ns) used to estimate the absolute binding free energies as described in the previous section.

b) To test whether the conformational state of the F-helix depends on its starting conformation, we used 3 PDB structures of L99A with 3 conformational states of the F-helix or loop (residues 107-115): i) a closed loop conformation (PDB code: 4W51), ii) an intermediate loop conformation (PDB code: 4W55), and an open loop conformation (PDB code: 4W59). We used pdbfixer 1.4 to remove the ligands and the water molecules and to add the missing heavy atoms to the receptor [6]. Then, we used PDB2PQR web server to protonate the receptors residues at pH 7 and to rename the residue/atom according to the AMBER naming scheme. Then, we converted the outputted receptor files to PDB files using Parmed 2.7.4. Next, we superimposed each of the L99A complexes prepared in the previous section (toluene, PDB code: 4W51; ethylbenzene, PDB code: 4W53; n-propylbenzene (PDB code: 4W55); n-butylbenzene (PDB code: 4W57); iodobenzene (PDB code: 3DN4); p-xylene (PDB code 187L), o-xylene (PDB code: 188L), 3-iodotoluene [3], 4-iodotoluene [3], and benzylacetate (PDB code: 4w57)) to each of the prepared receptors with different F-helix conformation (PDB codes: 4W51, 4W55, and 4W59) using Chimera. For L99A:3-iodotoluene, we have also prepared a second complex, where we used the PDB structure of L99A:toluene (PDB code: 4W53) to manually generate the structure of 3-iodotoluene using Chimera, with respect to the receptor structure of the same PDB file (4w53). Next, we saved the coordinates of each ligand in the plane of the receptors having different F-helix conformations. As a result, we obtained 3 protein-ligand systems with three different F-helix conformation for each of the ligands. On each of these systems, we ran 100 ns of MD simulations.

c) To study the impact of sampling on the conformational state of the F-helix, we performed 3 different 1 μs long MD simulations on the apo L99A: i) apo L99A with a closed loop conformation (PDB code: 4W51), ii) apo L99A with an intermediate loop conformation (PDB code: 4W55), and iii) apo L99A with an open loop conformation (PDB code: 4W59).

d) In order to evaluate the accuracy of the force field we used in all our MD simulations, we prepared 9 different systems using a combination of three different amber force fields (AMBER ff14SB [7], AMBER ff15ipq [8], and AMBER FB-15 [9]) and the three protein structures with different F-helix conformation. On each of these 9 systems, we ran 200ns of MD simulations.

e) To study the effect of the temperature on MD simulations, we started 2 simulations of 100 ns each on the new RT structures of apo L99A with a closed and intermediate loop conformations, respectively.

For each separate system considered, we used YANK to generate, parametrize, solvate, and neutralize the complexes with the same options and parameters used and described in section (number of the section above).

BLUES simulations to enhance the sampling of ligand binding mode and side chain torsions.

Because sampling of ligand binding modes and protein torsional degrees of freedom was in some cases quite slow in our simulations, we wanted to use enhanced sampling techniques to help ensure our sampling was adequate. Thus, we used BLUES (Binding modes of Ligands Using Enhanced Sampling) simulations package to i) enhance sampling of ligand binding modes [3] and 2) accelerate the sampling of side chain rotamers in the protein's residues [10]. More details about BLUES approach and protocols can be found in literature [3, 10] and in the BLUES documentation ((https://github.com/MobleyLab/blues) and (https:// mobleylab-blues.readthedocs.io)).

The BLUES simulations were executed using OpenMM 7.1.1 using 4 femtoseconds (fs) time steps with the hydrogen-mass repartitioning approach.

We performed BLUES side chain sampling on apo and holo L99A complexed with iodobenzene, where we enhanced the side chain sampling of two residues belonging to the protein's binding site (Val 111 and Leu 118). We used BLUES version 0.2.4+86.g364cfe1.dirty to promote small randomized side chain moves and ran a total of 100 ns MD on each system.

For the BLUES binding mode simulations, BLUES version 0.2.2 was used to propose random ligand rotation moves. We performed a total of 200 ns MD per simulation.

All the input files and scripts used to set up and run the BLUES simulations in this work can be found in the GitHub repository associated with this paper (https://github.com/MobleyLab/T4L-temperature-effects).

Docking of a library of small ligands to the cryo and room temperature structures of L99A.

We wanted to evaluate the performance of a standard docking algorithm: -- Autodock Vina [11] -- on T4 lysozyme L99A and compare the results to those of OEdock. We used the PDB structures output by OEdock – our library of actives and decoys (98 binders and 3152 decoys) -- and performed docking in the same PDB structures of the six protein structures as we used for OEdock (as described in Methods section on docking). We converted the PDB files of the proteins and the T4 compounds to pdbqt format using scripts from Autodock Tools [12]. The exhaustiveness was set to 50. The input files and scripts used with Autodock Vina are available in the GitHub repo. In some cases, docking scores for multiple ligands were identical on the first pass, impairing ranking, so, since the docking scores contain only one decimal, we reprocessed the scores of the best docking poses using the –score_only flag (for single-point energy calculation on the best docked pose) generating scores with 5 decimals and thus accurate ranks. Autodock Vina uses a completely empirically-weighted scoring function, including Gaussian steric interactions, a repulsion term, linear hydrophobic and hydrogen-bond interaction terms, and torsion terms [13]. For OEdock, we used two different scoring functions: Chemgauss3 [14] for the exhaustive search scoring followed by Chemscore [15] for an optimization scoring. The former uses Gaussian smoothed potentials to evaluate the complementarity between ligand poses and the binding site and entails the following terms: steric, hydrogen bond, metal-ligand, ligand and protein desolvation. Chemscore, a universal empirical scoring function used to score the poses during optimization, is a sum of the following contributions: lipophilic, hydrogen bonding, metal-chelator, clashes, rotatable bonds, a term to penalize excessive flexibility, favorable interactions that occur when: i) two non-polar heavy atoms (one ligand atom and one protein atom) are placed near each other, ii) acceptor-donor interactions are formed between the ligand and the protein, or acceptor atoms on the ligand are placed near metal atoms on the protein. In terms of the search algorithm, the OEdock method used here produces the docking poses by rotating the ligand conformations pre-generated by OMEGA (from OEtoolkits) to complement the protein binding site. On the other hand, Autodock Vina applies a hybrid global-local search to sample the pose space [11]. Also, we applied rigid receptor approach with both OEdock and Autodock Vina. We used a reference ligand to indicate the binding site for OEdock and one of this ligand's atoms was considered the center of the Autodock Vina docking box.

For all other systems, we used the same protocol as the T4L-L99A case. We selected 11, 23 experimentally confirmed binders from previous work for thrombin [16] and PTP1B [17], respectively. 26 and 25 additional binders for thrombin and PTP1B found on BindingDB database [18] (https://bindingdb.org) were also included in this work. A number of 2961 and 2641 DUD-E "decoys" [19, 20] were generated. OEdock (OpenEye Scientific Software) was used to dock these ligands to both raw RT and raw cryo

structure and equilibrated structure extracted from MD simulations (after 50 ns) for both temperatures of thrombin and PTP1B.

A reference ligand (thrombin PDB: 2ZFF, PTP1B PDB: 2QBS) was used to localize the binding site. Then the scores were ranked and the metrics (AUC, logAUC) were calculated. The same scoring functions (Chemgauss3 and Chemscore) as we used in the T4L-L99A study were used.

Details of calculations on additional systems

Systems setup. We built the apo structure of these systems using the following PDB code: PTP1B (RT: 6B8X, cryo: 6B90), galectin-3 (RT: 3ZSM, cryo: 3ZSK), thrombin (RT: 3VXF, cryo: 3VXE), CCP (RT: 4NVA, cryo: 4OQ7). We used pdbfixer 1.4 to remove the ligands and the water molecules and to add the missing heavy atoms to the receptor. Then, we used PDB2PQR web server to protonate the receptors residues at experimental pH values and to rename the residue/atom according to the AMBER naming scheme. The AMBER ff14SB force field [21] was used for protein parameterization in conjunction with TIP3P water model. OpenMM package was used to generate, parametrize, solvate, and neutralize the systems.

MD simulations. Langevin dynamics with a collision frequency of 1 ps^{-1} was used in the NVT ensemble simulation. Production simulations were done in the NPT ensemble; the temperature was controlled through Langevin dynamics and a constant pressure was maintained using Monte Carlo barostat. Long-range electrostatic interactions were calculated using the particle mesh Ewald method, with a cutoff of 10 Å for the real space electrostatics and Lennard-Jones forces.

MD simulations were performed to study the conformational change of protein tyrosine phosphatase 1B (PTP1B), galectin-3, thrombin and cytochrome c peroxidase (CCP) using OpenMM package. The systems were firstly minimized until forces were below a tolerance of 10 kJ/mol, followed by 1 ns NVT equilibration and 10 ns NPT equilibration. The production run was performed in the NPT ensemble for 50 ns of a single trial (5 parallel trails) and was extended for at least 4 times, resulting in at least 200 ns for each trial and 1 μs in total.

Free energy calculations. The ligand was parameterized using Open Force Field version 1.0.0 (codenamed "Parsley") [22]. Hybrid structures and topologies for the ligand pairs were generated using pmx [23, 24] following a single topology approach. The workflow established a mapping between atoms of two ligands based on the maximum common substructure and conformational alignment while minimizing perturbation and stabilizing the system. The AMBER ff14SB force field [21] was used for protein parameterization.

Dodecahedral boxes were filled with TIP3P explicit solvent model solvated ligand pairs/ligand-protein complexes and counterions (150 mM NaCl). The stochastic dynamics thermostat was used to control the temperature in the simulations. The Parrinello-Rahman barostat [25] was applied to keep the pressure constant. All bond lengths were constrained using the LINCS algorithm [26]. The van der Waals interactions were smoothly switched off between 1.0 and 1.1 nm. A dispersion correction for energy and pressure was used. The non-bonded interactions for the alchemical transitions were treated with a modified soft-core potential [27].

Detailed SI Results

Conformational states of T4 lysozyme complexes.

To assess T4 lysozyme L99A conformational change upon ligand binding, we carried out MD simulations to identify the F-helix conformation of the protein when complexed to several ligands, namely toluene, o-xylene, p-xylene, iodobenzene, 3-iodotoluene, 4-iodotoluene, ethylbenzene, butylbenzene, propylbenzene, hexylbenzene, and benzylacetate. The MD simulations were done using the crystal structures of these complexes. For 3-iodotoluene and benzylacetate, we chose the co-crystal structure of the closest congeneric ligand which we manually modified to generate the 3D structure of these four ligands. . For another 3-iodotoluene complex and 4-iodotoluene, we used the PDB structure of L99A:3-iodotoluene from Gill et al. [3]; more details describing the set-up of these systems are provided in the SI methods.

Our results show that all the studied complexes adopt a dominant closed F-helix conformation (Figure S27). However, the F-helix of L99A:3-iodotoluene and L99A:hexylbenzene show higher occupancy for the intermediate and the open conformations, respectively.

In order to identify whether the conformation of the F-helix depends on its starting conformation, we performed MD simulations on all the above mentioned L99A complexes, beginning from the protein's open, intermediate, and closed conformations. Our results illustrated in Figures S26 and S28 highlight that the F-helix conformational state is independent from the starting conformation, as it ought to be when our simulations are long enough, except when binding o-xylene, p-xylene, 3-iodotoluene, and hexylbenzene. To further understand the differences observed for the occupancy of the loop conformation of these latter four complexes, we analyzed the rotamer distributions of four important amino acid residues belonging to the F-helix sequence: Glu108, Thr109, Val111 as well as Met106 located near the binding site (Figures S41-S44). This analysis showed that the rotamer distributions of these residues are different when starting with closed, intermediate, and open conformations, indicating

protein motions are particularly slow when bound to these ligands, causing sampling problems for our simulations.

Also, we calculated the population of the F-helix states during 100 ns of MD simulations performed starting with the room temperature structure of apo-L99A beginning from, alternately, both closed and an intermediate F-helix conformation. Our results, as presented in Figure S29, show a dominant occupancy of the F-helix conformation (97%) when starting from either the closed or intermediate RT structure. These findings are consistent with the F-helix occupancy observed experimentally at RT.

Absolute binding free energy calculations.

We performed a binding free energy calculation on iodobenzene using the PDB structure of L99A in complex with toluene, where we manually modified toluene to create a 3D structure of iodobenzene. We used the same binding free energy protocol described in (Methods section: absolute binding free energy calculation-B). As a result, we obtained an absolute binding free energy of -5.10 kcal/mol which differs by 0.6 kcal/mol than from the binding free energy calculated starting with the cryo structure (-4.5 kcal/mol), where iodobenzene (binding mode A) is co-crystallized with L99A (Table 1). Overall, our binding free energy results using different iodobenzene binding modes suggest that such calculations are sensitive to the binding mode of the ligand and the receptor structure due to the slow timescales involved for receptor conformational changes and binding mode changes.

BLUES simulations for ligand binding mode.

Using BLUES, a non-equilibrium candidate Monte Carlo approach coupled with MD simulations [3], we have accelerated the sampling of the binding of iodobenzene, benzylacetate, ethylbenzene, propylbenzene, o-xylene, p-xylene, and butylbenzene within the L99A protein structure. BLUES simulations enhance sampling of ligand binding modes, allowing us to explore multiple candidate binding modes or "metastable binding modes". Following BLUES simulations, we evaluated whether the favorable binding modes sampled during BLUES simulations are close to the native binding modes by computing the average RMSD of each macrostate or metastable binding mode relatively to the respective crystallographic binding mode. Here, a binding pose is considered close to the crystallographic binding mode if an RMSD accuracy of < 2 Å is achieved.

For iodobenzene, there are two crystallographic binding modes A and B obtained at room temperature as shown in Figure S30 (These are the same binding modes identified in the cryo structure).

The analysis of our BLUES simulations shows two metastable binding modes; the dominant binding mode represented by the red cluster has an average RMSD of 1.64 Å relatively to the binding mode A while the green cluster is closer to the binding mode B with an RMSD of 2.19 Å. The closest pose to the crystallographic binding mode B has a minimum RMSD of 0.52 Å and the closest pose to the crystallographic binding mode A has a minimum RMSD of 0.39 Å (SI Figs. S30-S31). It is interesting to note that we started our BLUES simulations with the crystallographic binding mode A. Whereas a ligand is usually confined in its starting configuration during standard MD simulations, the BLUES approach accelerated the binding mode sampling of iodobenzene, allowing it to visit a native configuration distinct from the starting binding mode.

For o-xylene, ethylbenzene, propylbenzene, and butylbenzene, the dominant binding mode of each during BLUES simulations also reflects the corresponding crystallographic binding mode. More details about the BLUES findings can be found in the SI (Figures S31-36).

Impact of sampling on the MD trajectories.

To study whether an adequate sampling would impact the conformational state as well as the rotamer populations, we performed 1μs length MD simulations on apo L99A starting with closed, intermediate, and open conformations. Mostly the same conformational states of apo L99A were sampled when starting with the three different states (Figure S15).

Table 1 **Data collection and refinement statistics**

	apo cryo	apo RT	toluene cryo	toluene RT
PDB code	7L38	7L37	7L3A	7L39
Wavelength	1	1	1	1
Resolution range	51.82 - 1.33 (1.378 - 1.33)	36.03 - 1.439 (1.491 - 1.439)	45.67 - 1.11 (1.15 - 1.11)	46.52 - 1.35 (1.398 - 1.35)
Space group	P 32 2 1	P 32 2 1	P 32 2 1	P 32 2 1
Unit cell	59.8351 59.8351 96.3339 90 90 120	61.0056 61.0056 98.5292 90 90 120	59.907 59.907 96.255 90 90 120	61.0164 61.0164 98.0512 90 90 120
Total reflections	281014 (19919)	386524 (33648)	646311 (17280)	309107 (30011)
Unique reflections	46429 (4545)	39100 (3822)	74845 (4880)	47033 (4593)
Multiplicity	6.1 (4.4)	9.9 (8.8)	8.6 (3.4)	6.6 (6.5)
Completeness (%)	99.06 (98.95)	99.34 (96.72)	93.42 (62.15)	99.19 (97.80)
Mean I/sigma(I)	9.07 (1.17)	15.51 (1.78)	15.63 (1.35)	13.21 (1.87)
Wilson B-factor	18.28	19.68	12.03	17.08
R-merge	0.07008 (0.9907)	0.06086 (0.8267)	0.04888 (0.6393)	0.05458 (0.7523)
R-meas	0.07661 (1.126)	0.06427 (0.8781)	0.05182 (0.7553)	0.05917 (0.8155)
R-pim	0.03031 (0.5252)	0.02036 (0.292)	0.01687 (0.388)	0.02231 (0.3094)
CC1/2	0.995 (0.891)	0.999 (0.54)	1 (0.532)	0.999 (0.582)
CC*	0.999 (0.971)	1 (0.838)	1 (0.833)	1 (0.858)
Reflections used in refinement	46268 (4512)	39096 (3744)	74286 (4878)	47031 (4495)
Reflections used for R-free	2347 (196)	1985 (203)	1993 (134)	2376 (202)
R-work	0.1782 (0.3399)	0.1550 (0.3393)	0.1835 (0.3544)	0.1498 (0.3256)
R-free	0.1995 (0.3492)	0.1845 (0.3761)	0.2032 (0.3878)	0.1670 (0.3584)
CC(work)	0.959 (0.908)	0.958 (0.812)	0.952 (0.794)	0.968 (0.845)
CC(free)	0.976 (0.870)	0.940 (0.845)	0.944 (0.788)	0.976 (0.756)
Number of non-hydrogen atoms	1511	1556	1580	1589
macromolecules	1361	1463	1398	1472
ligands	21	21	14	27
solvent	129	72	168	90
Protein residues	162	162	162	162
RMS(bonds)	0.005	0.005	0.006	0.005
RMS(angles)	0.72	0.75	1.14	0.74
Ramachandran favored (%)	98.12	98.75	98.75	99.38
Ramachandran allowed (%)	1.88	1.25	1.25	0.62
Ramachandran outliers (%)	0	0	0	0
Rotamer outliers (%)	0	0	1.37	0.63
Clashscore	2.13	1.66	0.7	1.31
Average B-factor	26.46	26.15	16.05	22.68
macromolecules	25.51	25.25	14.85	21.63
ligands	35.07	38.24	15.27	27.31
solvent	35.03	40.87	26.06	38.5

iodobenzene RT	o-xylene RT	3-iodotoluene cryo	3-iodotoluene RT	4-iodotoluene cryo
7L3B	7L3C	7L3E	7L3D	7L3G
1	1	1	1	1
30.37 - 1.27 (1.315 - 1.27)	35.92 - 1.31 (1.357 - 1.31)	52.1 - 1.13 (1.17 - 1.13)	46.55 - 1.35 (1.398 - 1.35)	35.41 - 1.27 (1.315 - 1.27)
P 32 2 1	P 32 2 1	P 32 2 1	P 32 2 1	P 32 2 1
60.7496 60.7496 97.9211 90 90 120	61.0384 61.0384 97.8957 90 90 120	60.1622 60.1622 96.2956 90 90 120	61.1304 61.1304 97.7489 90 90 120	60.1876 60.1876 96.5073 90 90 120
457737 (45454)	338735 (33956)	432372 (15216)	311251 (30455)	335065 (19462)
55817 (5492)	51356 (5117)	70577 (4649)	46533 (4575)	53862 (5191)
8.2 (8.3)	6.6 (6.6)	6.1 (3.3)	6.7 (6.6)	6.2 (3.7)
99.53 (98.67)	99.58 (98.85)	92.66 (61.69)	97.65 (95.27)	99.41 (96.61)
14.13 (2.21)	9.03 (1.96)	16.61 (4.35)	11.12 (2.03)	17.33 (2.06)
13.93	16.06	11.3	15.76	14.8
0.07108 (0.8381)	0.09735 (0.7518)	0.05822 (0.227)	0.07037 (0.7694)	0.03793 (0.3968)
0.07615 (0.8928)	0.1059 (0.8156)	0.0634 (0.266)	0.0764 (0.8343)	0.04133 (0.4575)
0.02674 (0.3044)	0.041 (0.3127)	0.02462 (0.1346)	0.02913 (0.3177)	0.01587 (0.2204)
0.994 (0.63)	0.991 (0.616)	0.997 (0.94)	0.994 (0.555)	0.999 (0.859)
0.999 (0.879)	0.998 (0.873)	0.999 (0.985)	0.999 (0.845)	1 (0.961)
55816 (5420)	51354 (5067)	70548 (4651)	46527 (4430)	53859 (5158)
2758 (237)	2624 (284)	3411 (201)	2349 (194)	2638 (211)
0.1488 (0.3070)	0.1521 (0.3257)	0.1482 (0.1419)	0.1443 (0.3051)	0.1562 (0.2661)
0.1672 (0.3467)	0.1770 (0.3404)	0.1534 (0.1567)	0.1621 (0.3325)	0.1741 (0.2751)
0.963 (0.841)	0.966 (0.830)	0.963 (0.958)	0.971 (0.827)	0.963 (0.930)
0.954 (0.750)	0.953 (0.853)	0.957 (0.945)	0.976 (0.713)	0.958 (0.913)
1585	1569	1716	1570	1698
1461	1454	1466	1445	1489
31	21	21	25	29
93	94	229	100	180
162	162	162	162	164
0.005	0.005	0.005	0.005	0.005
0.75	0.75	0.81	0.72	0.79
99.38	99.38	98.75	99.38	98.77
0.62	0.62	1.25	0.62	1.23
0	0	0	0	0
0	0.65	0	0	0.64
1.65	1.34	0.33	1.01	2.29
20.34	21.69	15.8	22.27	20.2
19.22	20.73	13.81	21.12	18.55
24.82	27.32	16.63	31.19	21.73
36.54	35.35	28.48	36.64	33.59

4-iodotoluene RT	ethylbenzene RT	propylbenzene RT	benzylacetate cryo	benzylacetate RT
7L3F	7L3H	7L3I	7L3K	7L3J
1	1	1	1	1
30.56 - 1.49 (1.543 - 1.49)	35.92 - 1.39 (1.44 - 1.39)	29.09 - 1.46 (1.512 - 1.46)	30.1 - 1.11 (1.15 - 1.11)	52.93 - 1.49 (1.543 - 1.49)
P 32 2 1	P 32 2 1	P 32 2 1	P 32 2 1	P 32 2 1
61.129 61.129 97.868 90 90 120	61.066 61.066 97.8872 90 90 120	60.977 60.977 97.2679 90 90 120	60.2013 60.2013 96.3778 90 90 120	61.1132 61.1132 97.9617 90 90 120
210620 (21128)	279652 (26580)	244048 (22409)	867449 (23531)	232996 (23497)
35206 (3448)	43109 (4237)	36984 (3650)	77322 (5876)	33548 (3284)
6.0 (6.1)	6.5 (6.3)	6.6 (6.1)	11.2 (4.0)	6.9 (7.2)
98.69 (96.81)	98.64 (97.07)	99.60 (98.74)	96.07 (74.32)	94.70 (93.46)
8.76 (1.75)	12.57 (2.02)	13.50 (1.85)	27.05 (5.02)	11.90 (2.25)
18.63	16.68	16.13	12.01	18.06
0.07524 (0.7262)	0.06314 (0.7225)	0.06471 (0.715)	0.04225 (0.231)	0.07733 (0.7167)
0.08252 (0.7937)	0.06873 (0.7881)	0.07035 (0.7831)	0.04424 (0.267)	0.08374 (0.7724)
0.03341 (0.3169)	0.02672 (0.3111)	0.02722 (0.3145)	0.01274 (0.1301)	0.03162 (0.2856)
0.998 (0.508)	0.998 (0.655)	0.999 (0.541)	0.998 (0.944)	0.994 (0.667)
1 (0.821)	1 (0.89)	1 (0.838)	0.999 (0.986)	0.998 (0.894)
35204 (3340)	43108 (4114)	36982 (3608)	77260 (5876)	33547 (3242)
1740 (203)	2139 (216)	1759 (171)	3949 (265)	1664 (187)
0.1475 (0.2830)	0.1495 (0.3235)	0.1483 (0.2991)	0.1536 (0.1473)	0.1540 (0.3054)
0.1702 (0.3217)	0.1721 (0.3307)	0.1680 (0.3226)	0.1667 (0.1657)	0.1735 (0.3308)
0.967 (0.858)	0.968 (0.860)	0.973 (0.824)	0.956 (0.962)	0.964 (0.844)
0.964 (0.859)	0.955 (0.843)	0.979 (0.768)	0.950 (0.931)	0.959 (0.836)
1545	1576	1582	1669	1542
1425	1444	1426	1446	1429
25	33	27	35	24
95	99	129	188	89
162	162	162	162	162
0.005	0.005	0.005	0.005	0.005
0.73	0.72	0.7	0.82	0.73
99.38	98.75	99.38	98.12	98.75
0.62	1.25	0.62	1.88	1.25
0	0	0	0	0
0	0	0.66	0.65	0.66
1.71	0.67	1.02	0.67	1.02
23.9	22.37	21.9	16.32	24.07
22.85	21.15	20.65	14.95	22.94
24.1	27.25	23.71	18.02	32.22
39.52	38.63	35.34	26.54	40.02

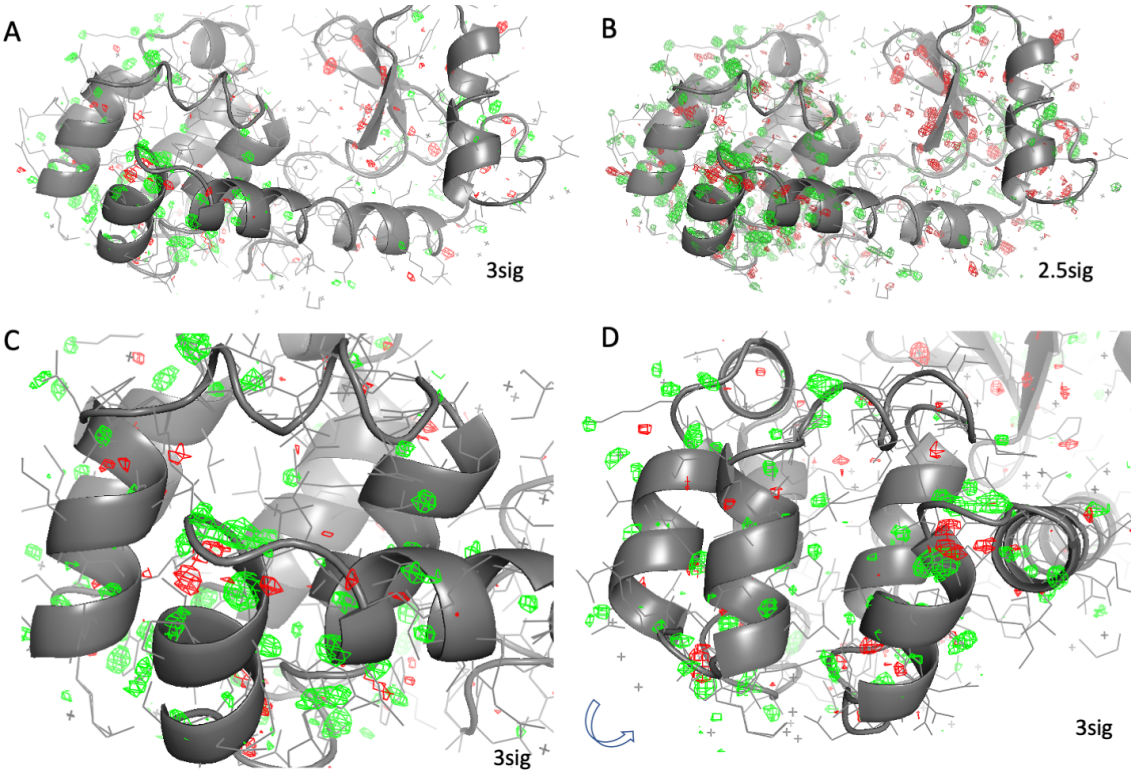

Figure S1. Binding sites are affected by temperature artifacts. Isomorphous Fo-Fo maps of the apo structure collected at cryo vs RT show differences in the electron density (green mesh, positive difference electron density; red mesh, negative difference density). This indicates idiosyncratic temperature effects, especially around the binding site in the lobe on the left hand side. Sigma levels are shown in Figure panel; C-D show zoom of A with ~90 deg rotation from C to D.

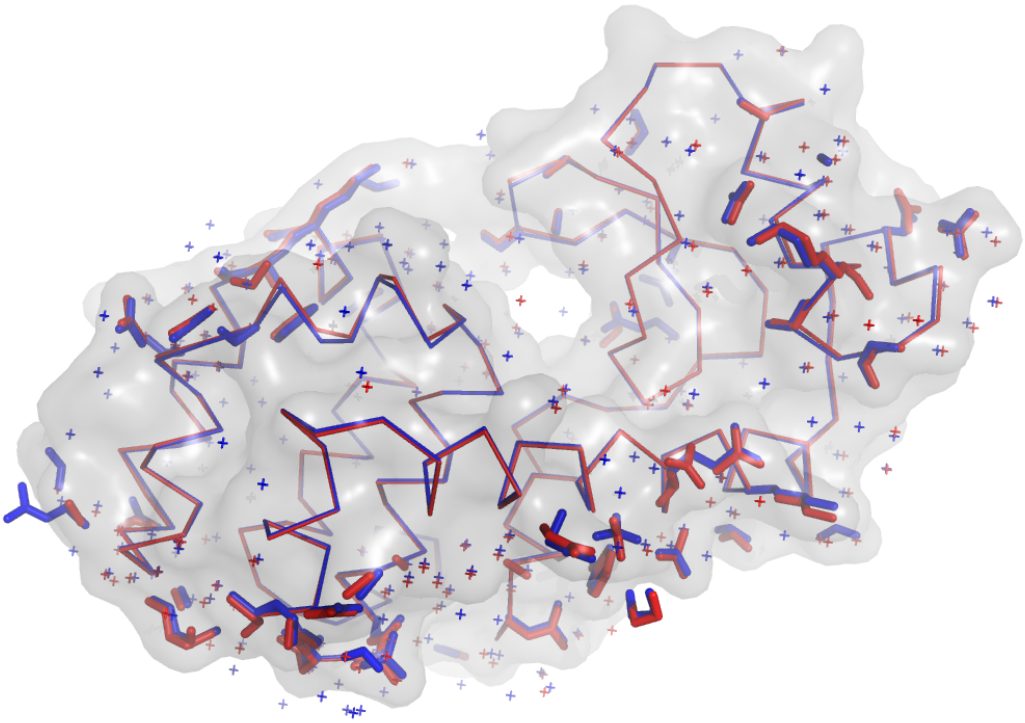

Figure S2. Crystal contact comparison of RT and cryo apo structures. Residues involved in crystal contacts of the apo structures at RT (red) and cryo (blue) are shown as sticks, as calculated by AreaIMol and with a similar orientation as Fig 1B-C. Only few residues at the crystal-packing interface are systematically affected by the UC compression in response to temperature across several datasets.

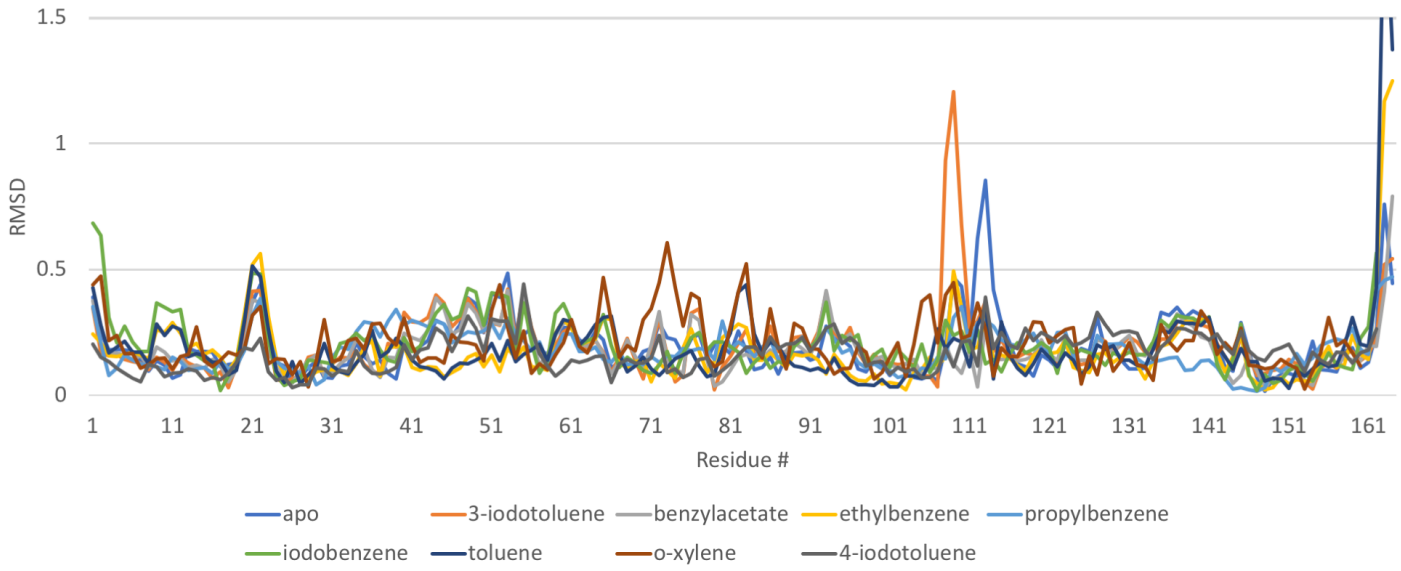

Figure S3. **Per residue RMSD values (Å) of aligned RT-cryo pairs with respective ligands.** Most residues have RMSDs < 0.5 Å; only the flexible C-terminus and residue T109 in the F-helix of 3-iodotoluene have an RMSD > 1 Å. The electron density in the region is less defined due to flexibility and modelled as two conformations for both RT and cryo. While this may exaggerate the RMSD, the placement of each conformation of the F-helix is supported by the respective electron density, indicating differences in response to temperature. Average RMSD are reported in Table S1. Residue RMSDs were calculated between equivalent, most occupied 'A' conformations, if multiple conformations were present.

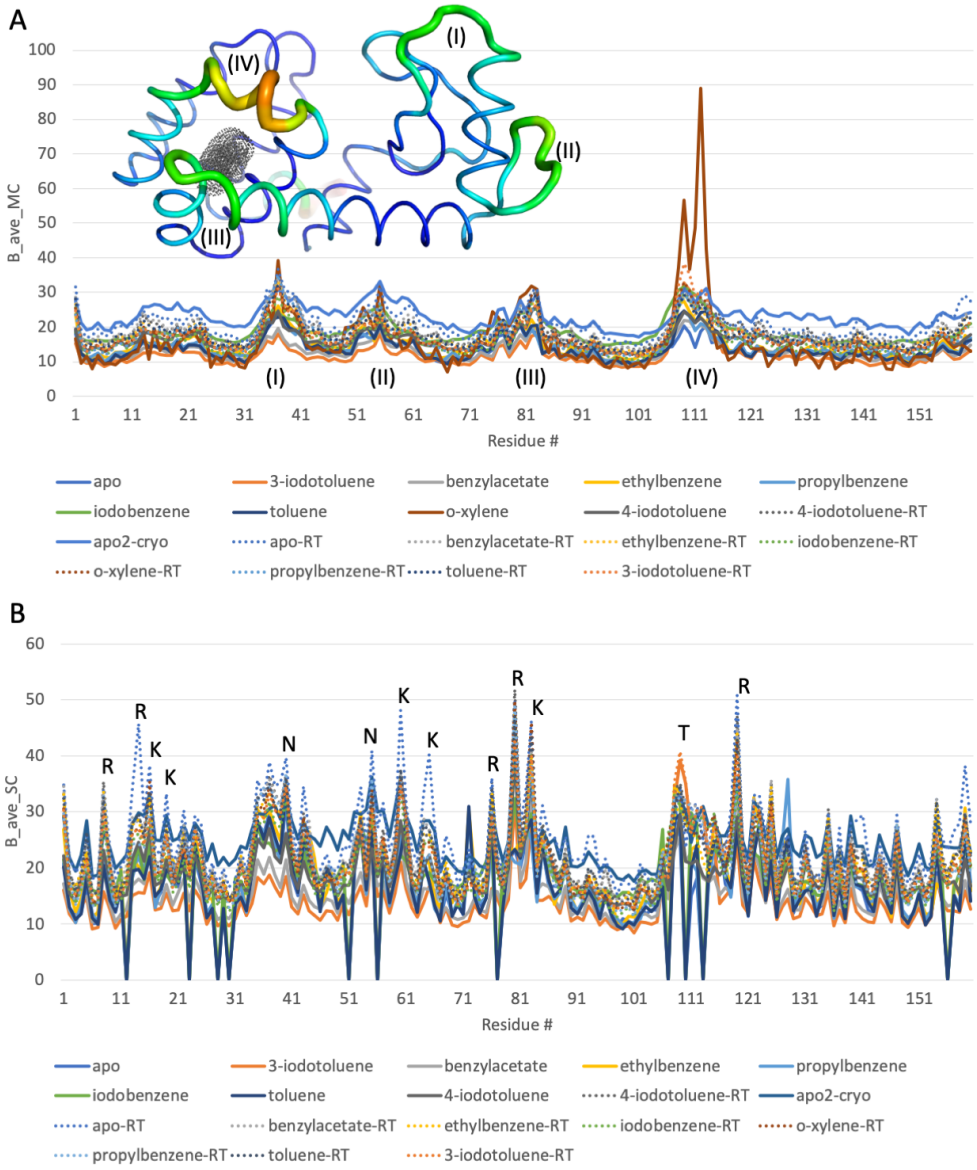

Figure S4. **B factor plots of all structures.** Per residue average B factors of the main chain and side-chains for all cryo (solid line) and RT (dashed line) pairs calculated with Baverage [28]. A) Across all temperature pairs, we mapped 4 regions with increased main chain B factors onto the protein surface, two of which are proximal to the binding site. B) The side-chains level B factor analysis shows no clear temperature trends beyond showing increased B factors for intrinsically flexible residues such as Arg, Lys and Asn.

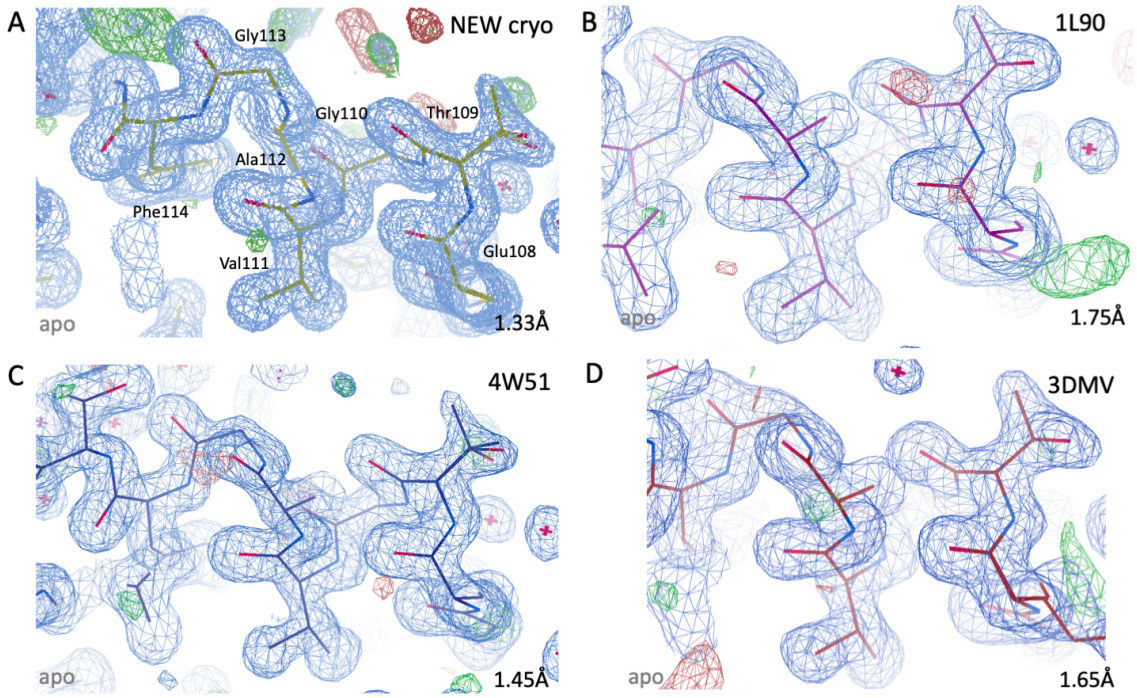

Figure S5. Electron density maps of cryo apo structures only show closed conformation. Comparison of electron density maps of apo binding site across high resolution PDB structures (resolution and PDB-ID indicated in each panel), show no evidence for the alternative F-helix conformation we observe in the RTX electron density map.

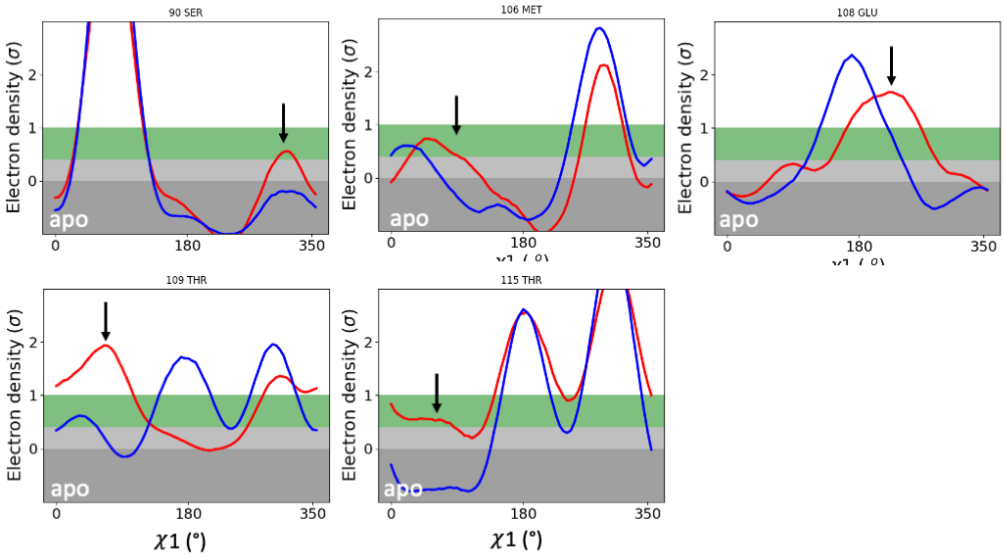

Figure S6. Binding site residues in apo T4L that respond to changes in temperature.
Ringer plots [29] visualize the electron density distribution per residue as a function of the Chi angles (here Chi1). Arrows indicate significant differences between cryo (blue) and RT (red) dataset.

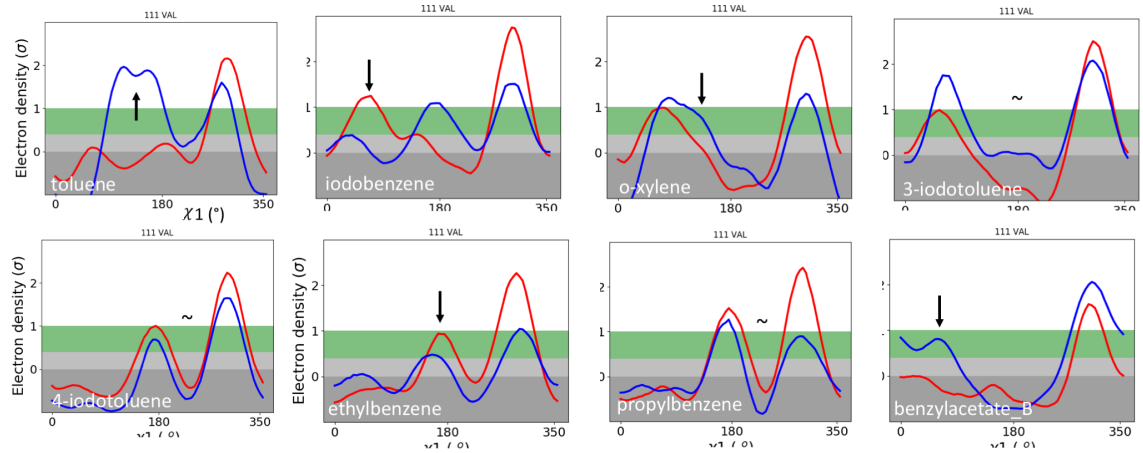

Figure S7. Val111 shows temperature-sensitivity in several ligand structures
Temperature induced changes of V111 across all ligand structures. Val111 has previously been shown to complicate ligand-binding predictions. Arrow indicates change shifting from cryo (blue) to RT (red), tilde indicates no major change in the distribution of side chains.

Table S2. Pairwise Tanimoto coefficients of L99A ligands calculated with a path-based fingerprint using OEFingerprint from OEtoolkits. The structural features used to perform the similarity search between the different ligands are: the atom type, the bond type, and the aromaticity. https://docs.google.com/spreadsheets/d/1tSevn6dI8urGoP3uICBK8ioyPsZN73nSwl7VPlapccw/edit#gid=0

Tanimoto (A, B)	Toluene	Ethylbenzene	Propylbenzene	Butylbenzene	Hexylbenzene	Iodobenzene	3-iodotoluene	4-iodotoluene	O-xylene	P-xylene	Benzylacetate
Toluene	-	0.65	0.52	0.45	0.41	1	0.94	0.94	0.94	0.94	0.36
Ethylbenzene	0.65	-	0.79	0.68	0.62	0.65	0.63	0.35	0.63	0.63	0.55
Propylbenzene	0.52	0.79	-	0.87	0.79	0.52	0.5	0.5	0.5	0.5	0.7
Butylbenzene	0.45	0.68	0.87	-	0.91	0.45	0.44	0.44	0.44	0.44	0.81
Hexylbenzene	0.41	0.62	0.79	0.91	-	0.41	0.4	0.4	0.4	0.4	0.75
Iodobenzene	1	0.65	0.52	0.45	0.41	-	0.94	0.94	0.9	0.94	0.36
3-iodotoluene	0.94	0.63	0.5	0.44	0.4	0.94	-	0.9	0.9	0.9	0.35
4-iodotoluene	0.94	0.63	0.5	0.44	0.4	0.94	0.9	-	0.9	1	0.35
O-xylene	0.94	0.63	0.5	0.44	0.4	0.94	0.9	0.9	-	0.9	0.35
P-xylene	0.94	0.63	0.5	0.44	0.4	0.94	0.9	1	0.9	-	0.35
Benzylacetate	0.36	0.55	0.7	0.81	0.75	0.36	0.35	0.35	0.35	0.44	-

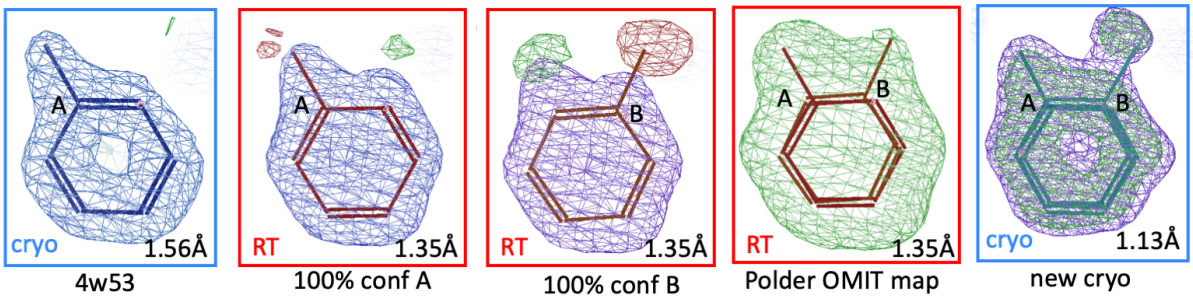

Figure S8. RTX reveals alternative toluene conformation. Toluene's alternative ligand conformations at RT are indicated by the presence of green Fo-Fc difference density when only the major conformer is included in refinement (panel 2 and 3 from left). An unbiased Polder OMIT map that excludes all ligands (superposed into map for clarity) confirms presence of both ligand conformers A and B (panel 4). Re-solving the cryo structure of toluene to atomic resolution of 1.13 A revealed the alternate conformer B also at cryo (panel 5).

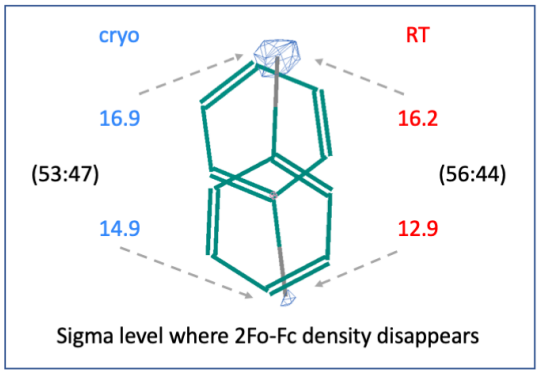

Figure S9. Iodobenzene occupancies differ with temperature.
While occupancy refinement converged to occupancies 33% for conformer A and 18% for conformer B, i.e. almost a 2:1 ratio, values based on the relative disappearance of peaks in the electron density maps indicate closer agreement between both datasets. Compared to other ligands studied here, the presence of electron-rich iodine in iodobenzene allows us to have high confidence in iodobenzene's two binding modes (I points up conformer A, down in conformer B). Sigma levels at which the 2Fo-Fc density (lightblue mesh) disappears are indicated in color for cryo (blue) and RT (red). Using sigma values of 16.9 vs 14.9 and 16.2 vs 12.9 to derive relative occupancies would result in a 53%:47% vs 56%:44% occupancy ratio, respectively.

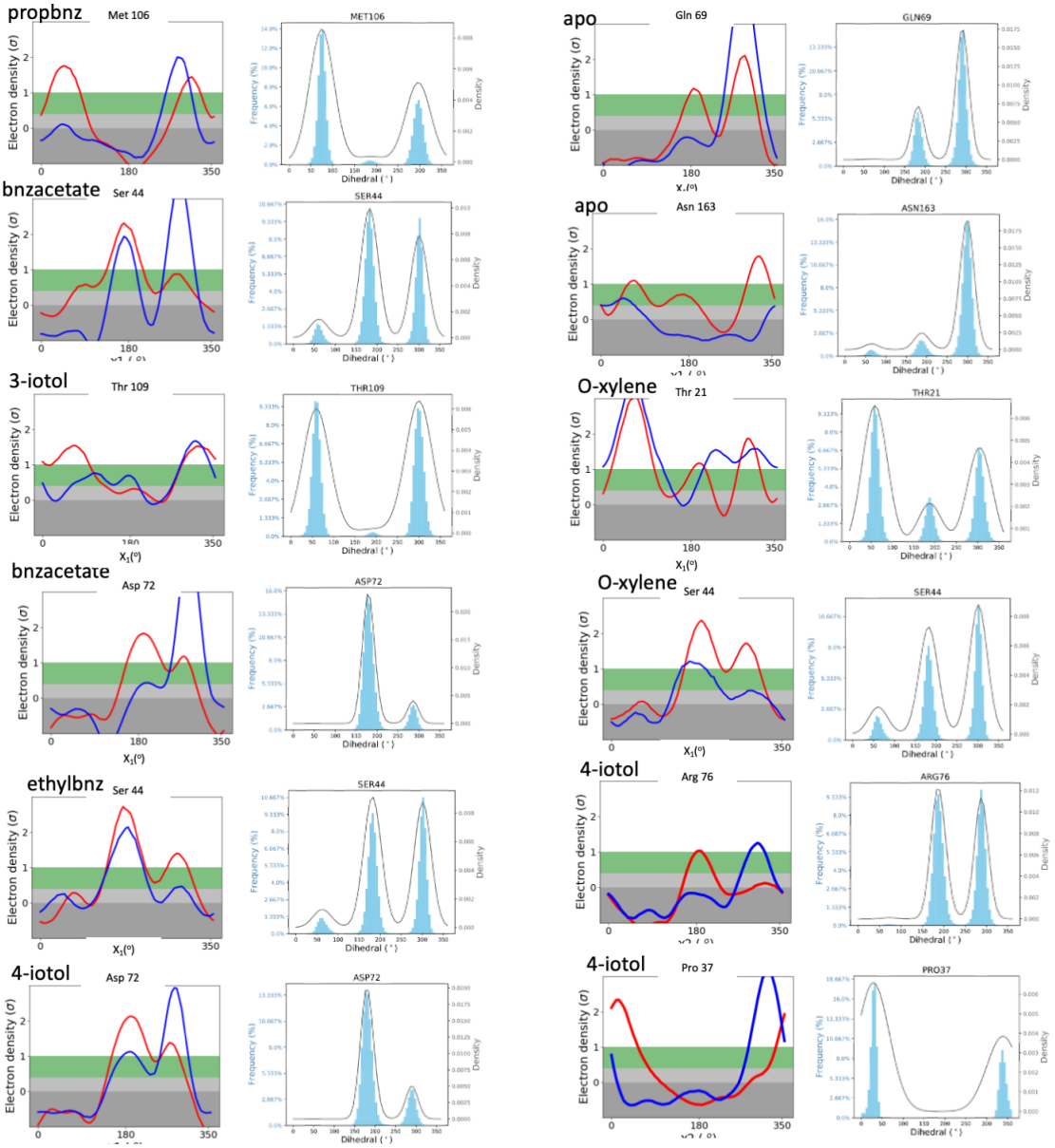

Figure S10. Further examples of false negatives in addition to main text Fig. 3. "False negatives" is used to describe the category of results where the Ringers-*Cringer* comparisons shows that MD simulations disagree with cryo data but, in fact, agree with RTX data.

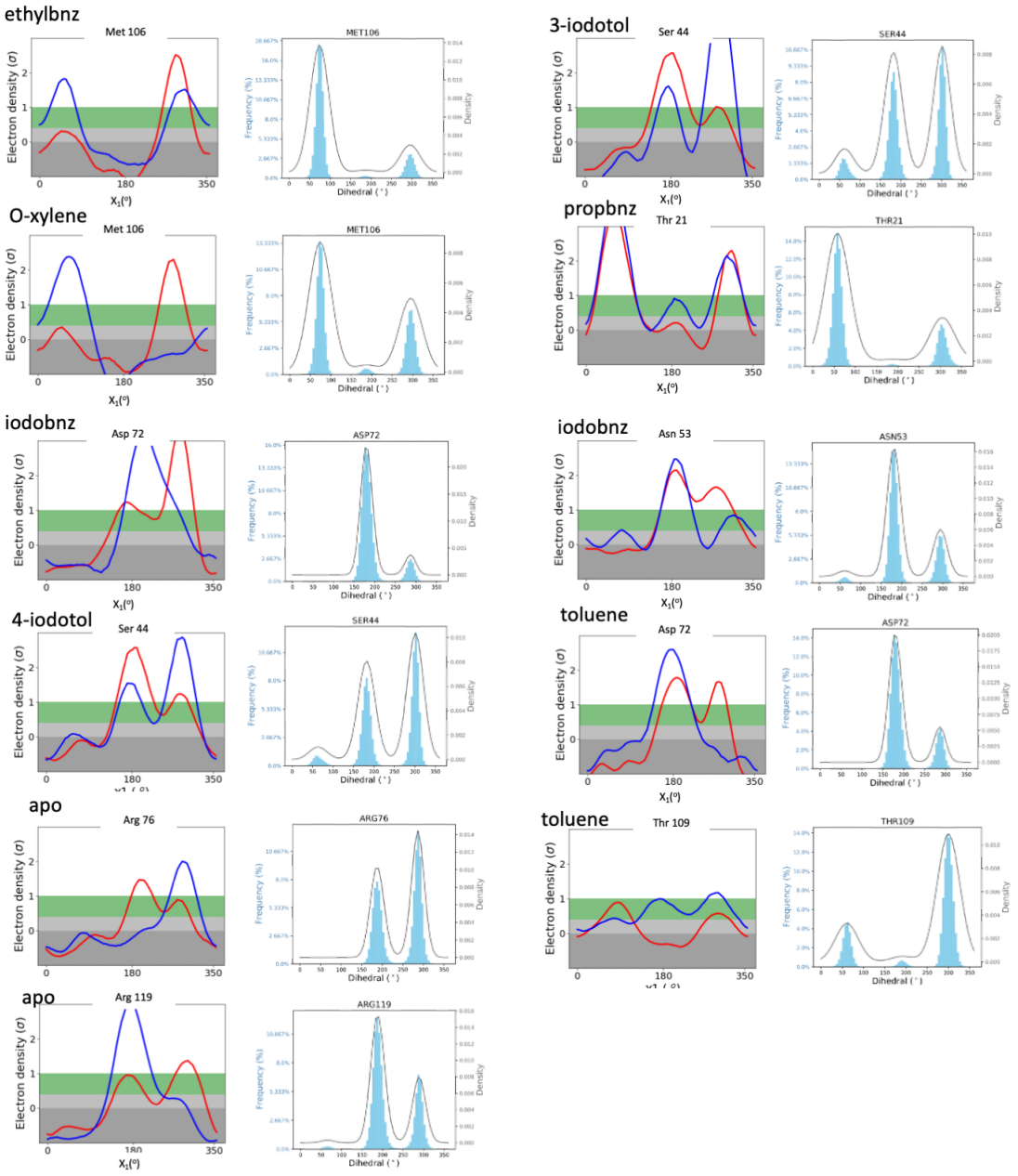

Figure S11. Further examples of false positives in addition to main text Fig. 3. "False positives" are results where the Ringer-*Cringer* comparison shows that MD data agree with cryo data, but disagree with RTX data.

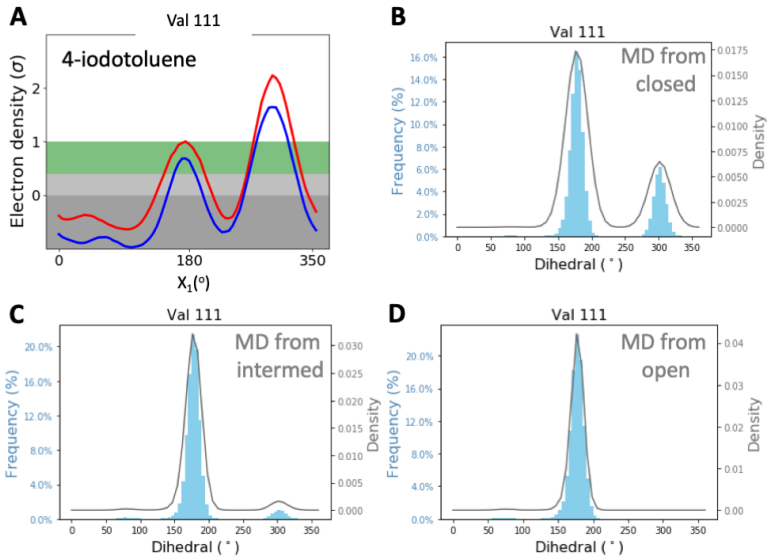

Figure S12. *Cringer*-Ringer comparison of Val111 for 4-iodotoluene. MD simulations started from "closed" (B), "intermediate" (C) and "open" (D) input structures 4W51, 4W55, and 4W59, respectively

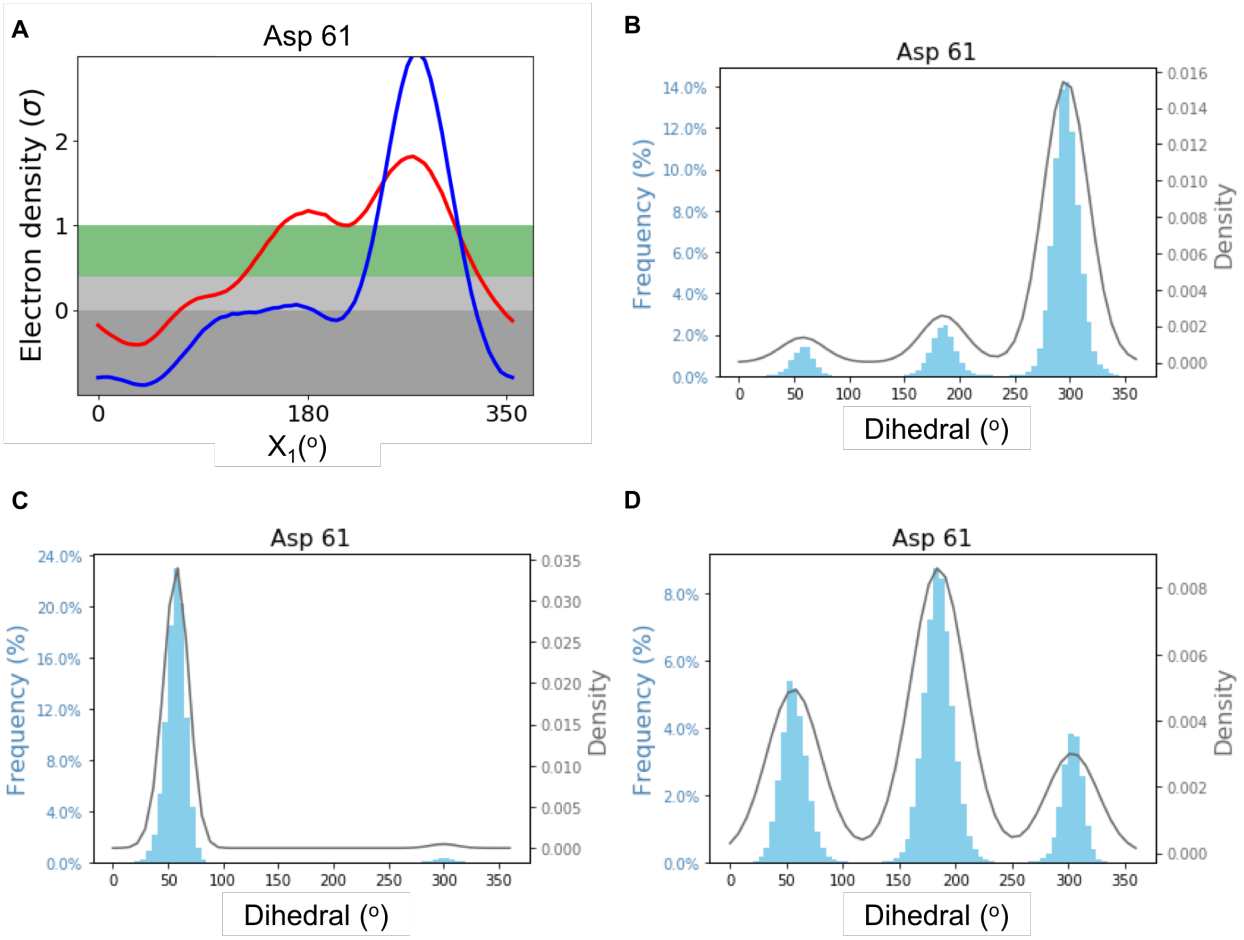

Figure S13. AMBER ff14SB captures the right rotamer distributions observed experimentally for Asp61 in apo L99A. 200 ns of MD simulations on apo L99A using: B) AMBER ff14SB protein force field, C) AMBER ff15ipq protein force field, and D) AMBER FB-15 protein force field. Only AMBER ff14SB captures the right dominant rotamer (around 270°) observed in cryo and RT structures and the second rotamer observed in RT structure (around 180°). The rotamer distributions are plotted using Gaussian kernel density estimation. The PDB code used to prepare the apo L99A structures with different protein force fields and run the simulations is 4W51.

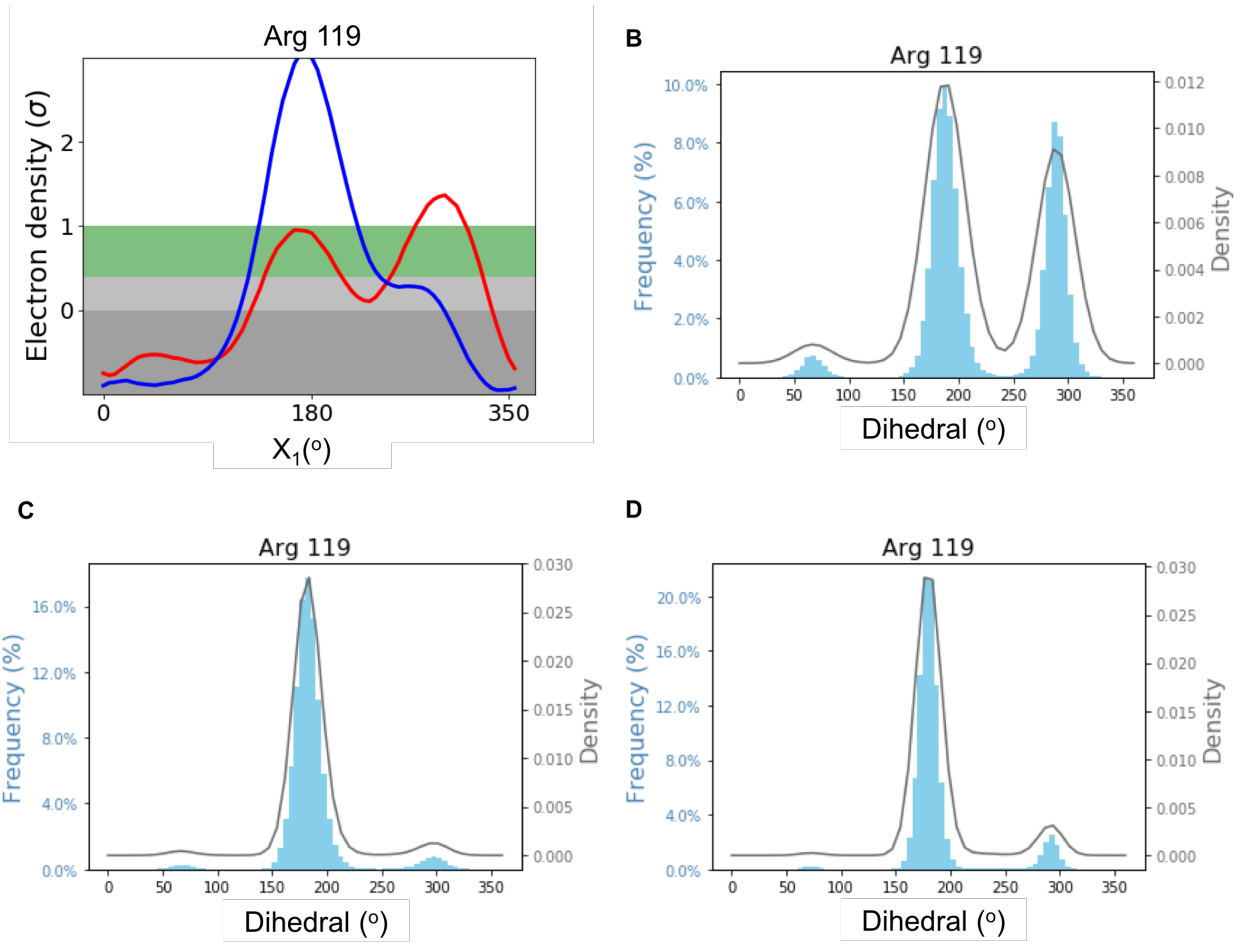

Figure S14. AMBER ff14SB shows a better sampling of the two rotamers of Arg 119 observed in the RT structure of apo L99A (around 180° and 290°), compared to AMBER ff15ipq and AMBER FB-15. 200 ns of MD simulations on apo L99A using: B) AMBER ff14SB protein force field, C) AMBER ff15ipq protein force field, and D) AMBER FB-15 protein force field. The rotamer distributions are plotted using Gaussian kernel density estimation. The PDB code used to prepare the apo L99A structures with different protein force fields and run the simulations is 4W51.

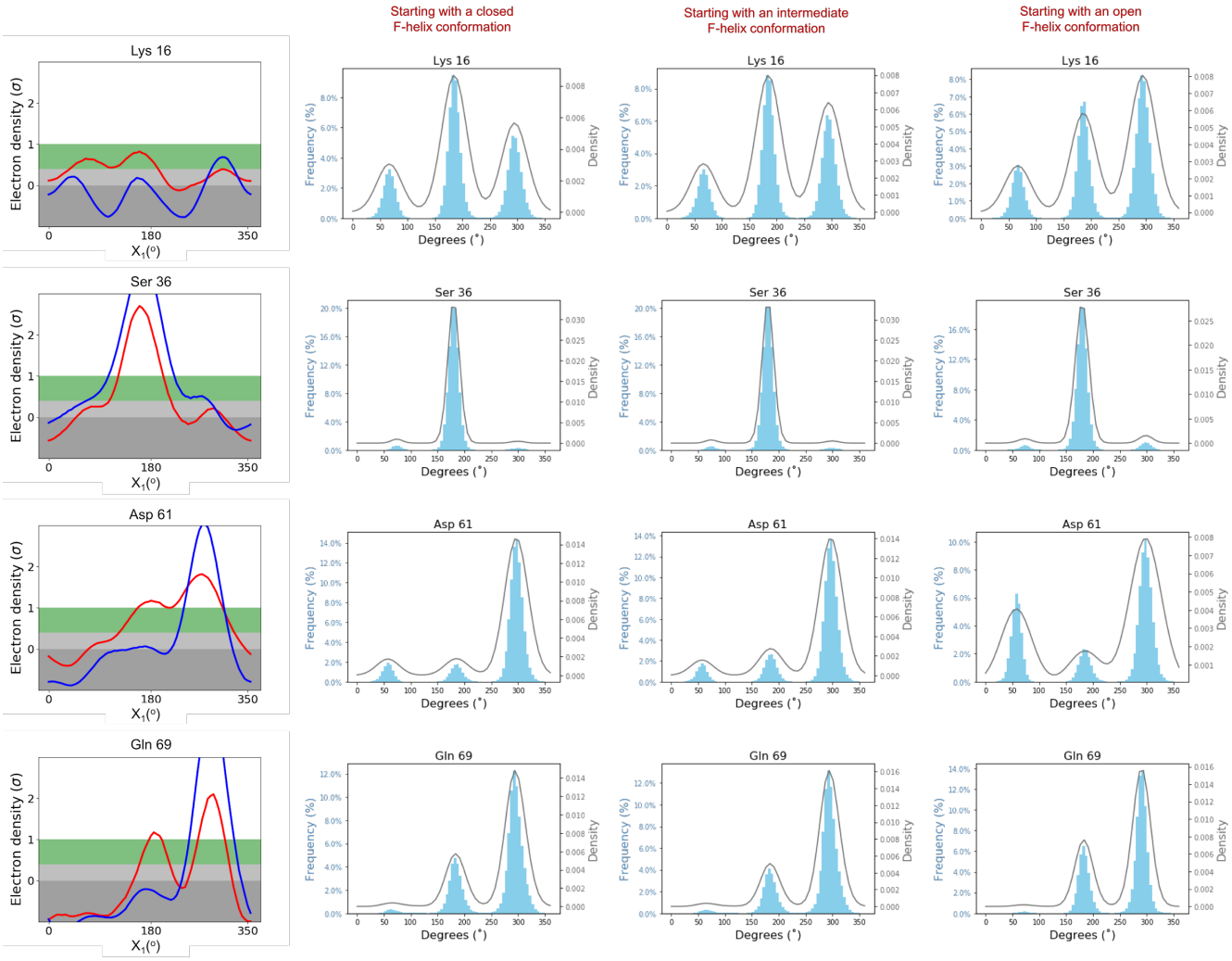

Figure S15. **Starting with different F-helix conformations, MD simulations converged to the same rotamers.** *Cringers* of Lys16, Ser36, Asp61, and Gln69 for apo L99A when starting with: i) a closed F-helix conformation, ii) an intermediate F-helix conformation, and iii) an open F-helix conformation. 3 different 1µs long MD simulations were performed on each of the three apo L99A systems. The PDB codes used to prepare L99A with a closed F-helix conformation, L99A with an intermediate F-helix conformation, and L99A with an open F-helix conformation are 4W51, 4w55, and 4W59, respectively. The rotamers are plotted using Gaussian kernel density estimation.

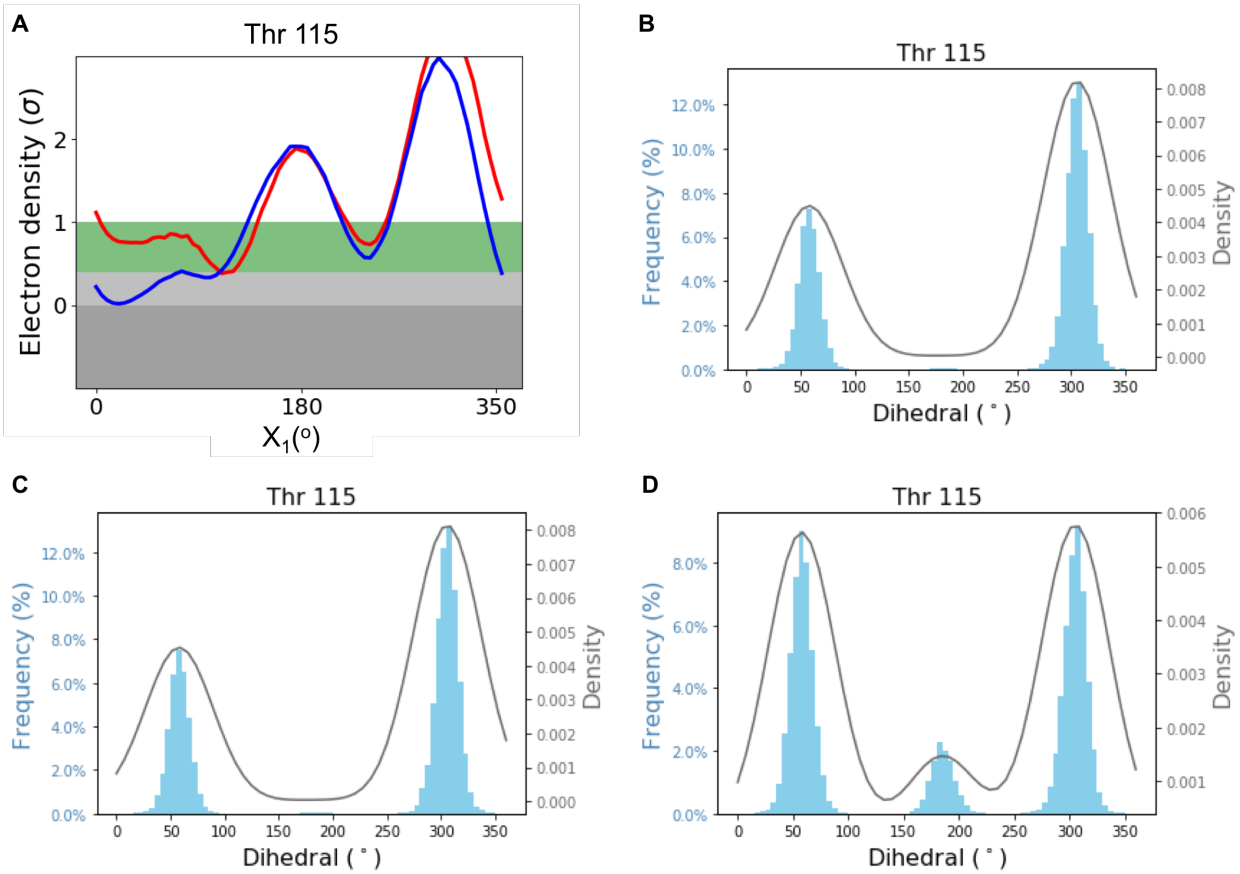

Figure S16.1. The input structure affects the rotamer sampling of Thr115 in L99A:ethylbenzene complex. 100 ns of MD simulations on L99A:ethylbenzene using B) a closed F-helix conformation (PDB code: 4W51), C) an intermediate F-helix conformation (PDB code:4W55) and D) an open F-helix conformation (PDB code: 4W59). Starting with an open F-helix conformation only (panel D), our simulations sampled a rotamer observed experimentally around 180° in the cryo and the RT structures of L99A:ethylbenzene complex. This rotamer was not captured using a closed (panel B) or an intermediate (panel C) loop conformations. Also, the second large peak in the computational results (around 50°) is only populated in the RT experiment. The rotamer distributions are plotted using Gaussian kernel density estimation.

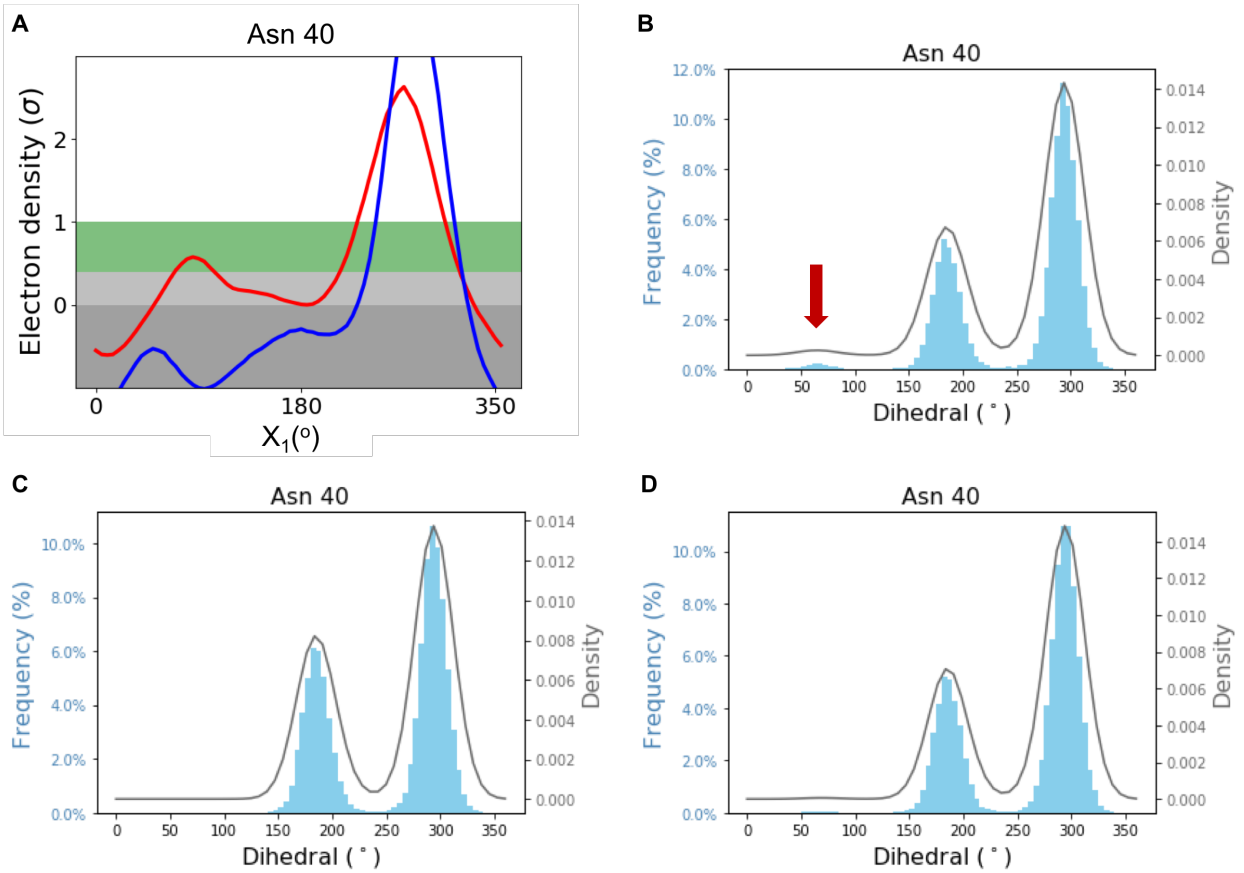

Figure S16.2. The input structure affects the rotamer sampling of Asn40 in L99A:3-iodotoluene complex. 100 ns of MD simulations on L99A:3-iodotoluene using B) a closed F-helix conformation (PDB code: 4W51), C) an intermediate F-helix conformation (PDB code:4W55) and D) an open F-helix conformation (PDB code: 4W59). Starting with a closed F-helix conformation only (panel B), our simulations sampled a minor rotamer observed at RT around 90° (highlighted on panel B with a red arrow). This rotamer was not captured using an intermediate loop conformation (panel C) and was barely observed during MD simulations using the open F-helix conformation (panel D). The rotamer distributions are plotted using Gaussian kernel density estimation.

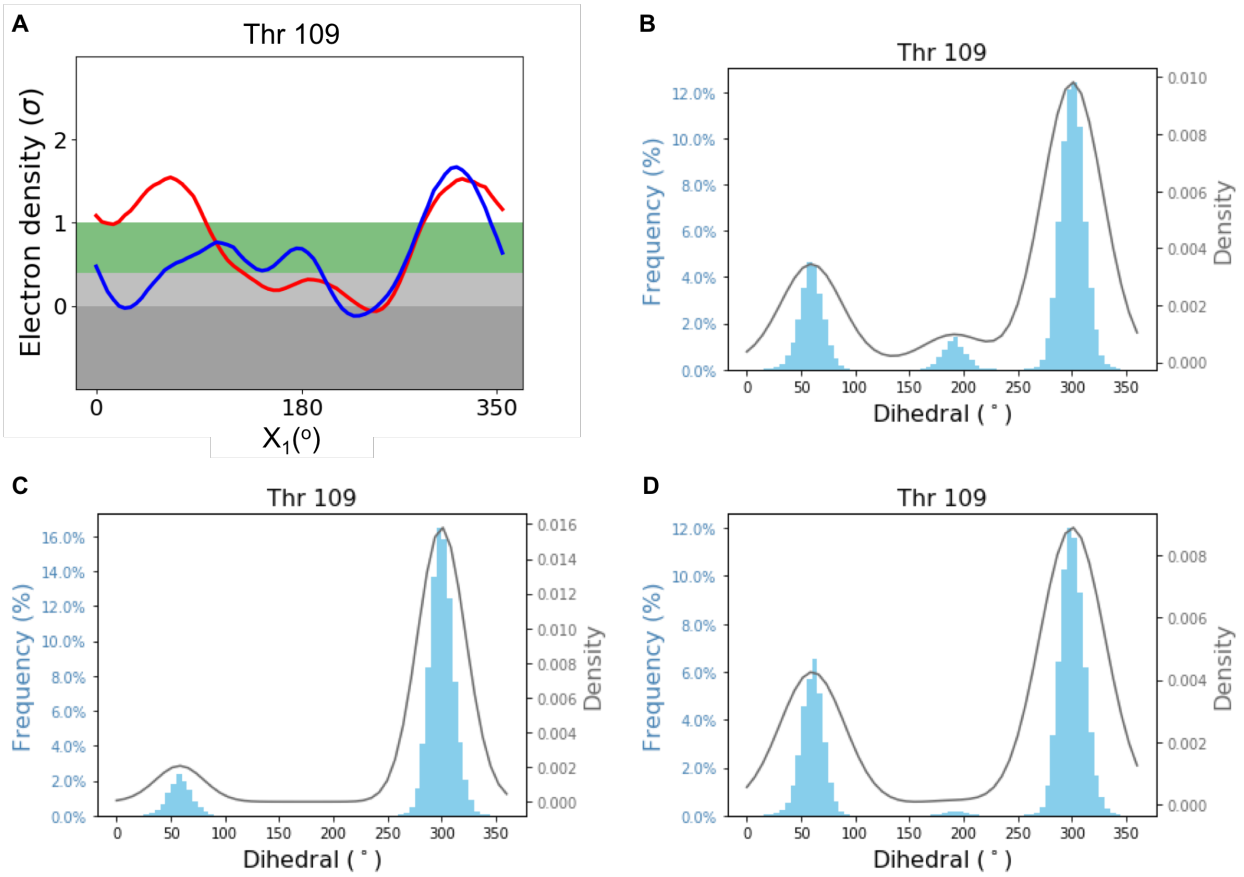

Figure S16.3. The input structure affects the rotamer sampling of Thr109 in L99A:3-iodotoluene complex. 100 ns of MD simulations on L99A:3-iodotoluene using B) a closed F-helix conformation (PDB code: 4W51), C) an intermediate F-helix conformation (PDB code:4W55) and C) an open F-helix conformation (PDB code: 4W59). Starting with a closed F-helix conformation only (panel B), our simulations sampled a minor rotamer observed experimentally around 180° in the cryo structure of L99A:3-iodotoluene complex. This rotamer was not captured using an intermediate loop conformation (panel C) and poorly sampled during MD simulations using the open F-helix conformation (panel D). The rotamer distributions are plotted using Gaussian kernel density estimation.

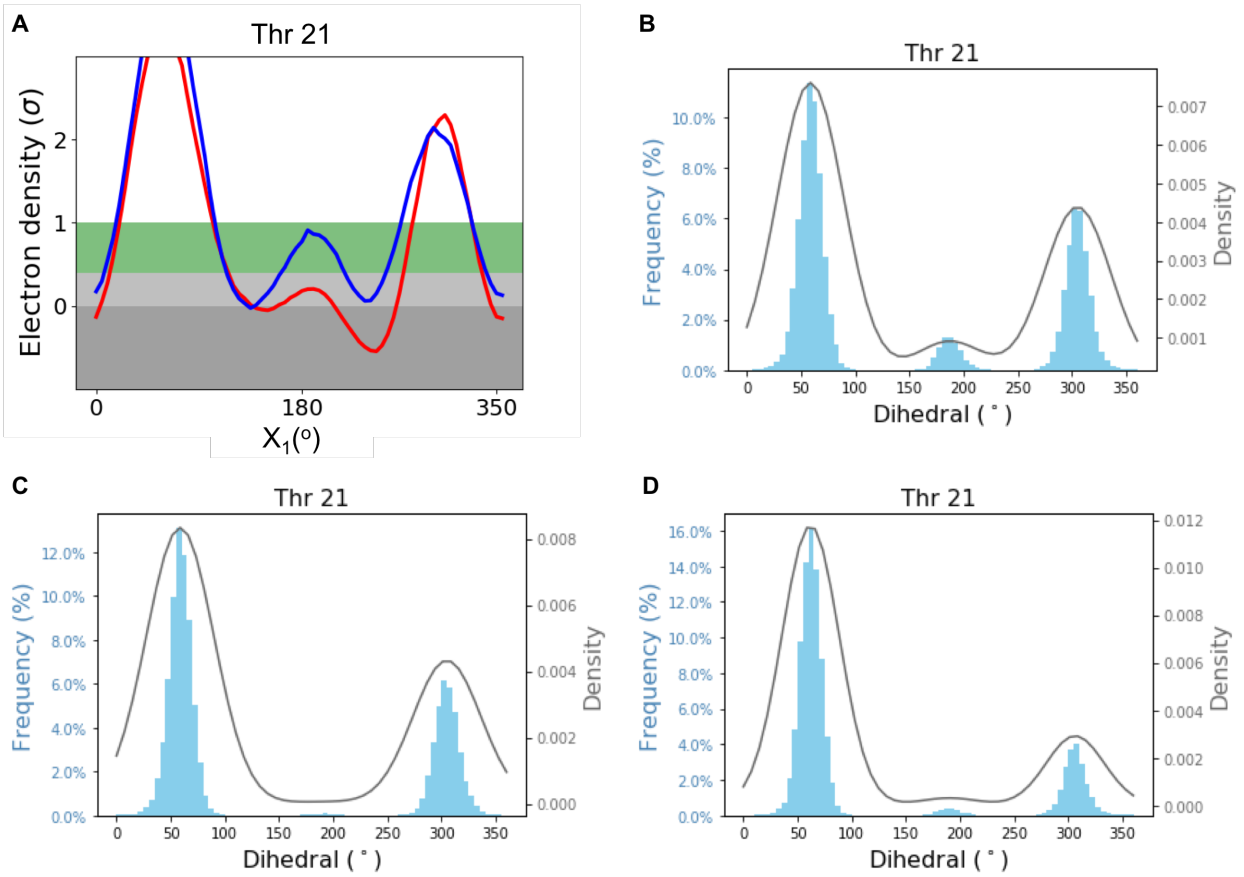

Figure S16.4. The input structure affects the rotamer sampling of Thr21 in L99A:propylbenzene complex. 100 ns of MD simulations on L99A:propylbenzene using B) a closed F-helix conformation (PDB code: 4W51), C) an intermediate F-helix conformation (PDB code:4W55) and C) an open F-helix conformation (PDB code: 4W59). Starting with a closed F-helix conformation (panel B), our simulations sampled better a rotamer around 180°, compared to the simulations using intermediate and open F-helix conformations. This sampled rotamer is observed experimentally in the cryo structure of L99A:propylbenzene complex. The rotamer distributions are plotted using Gaussian kernel density estimation.

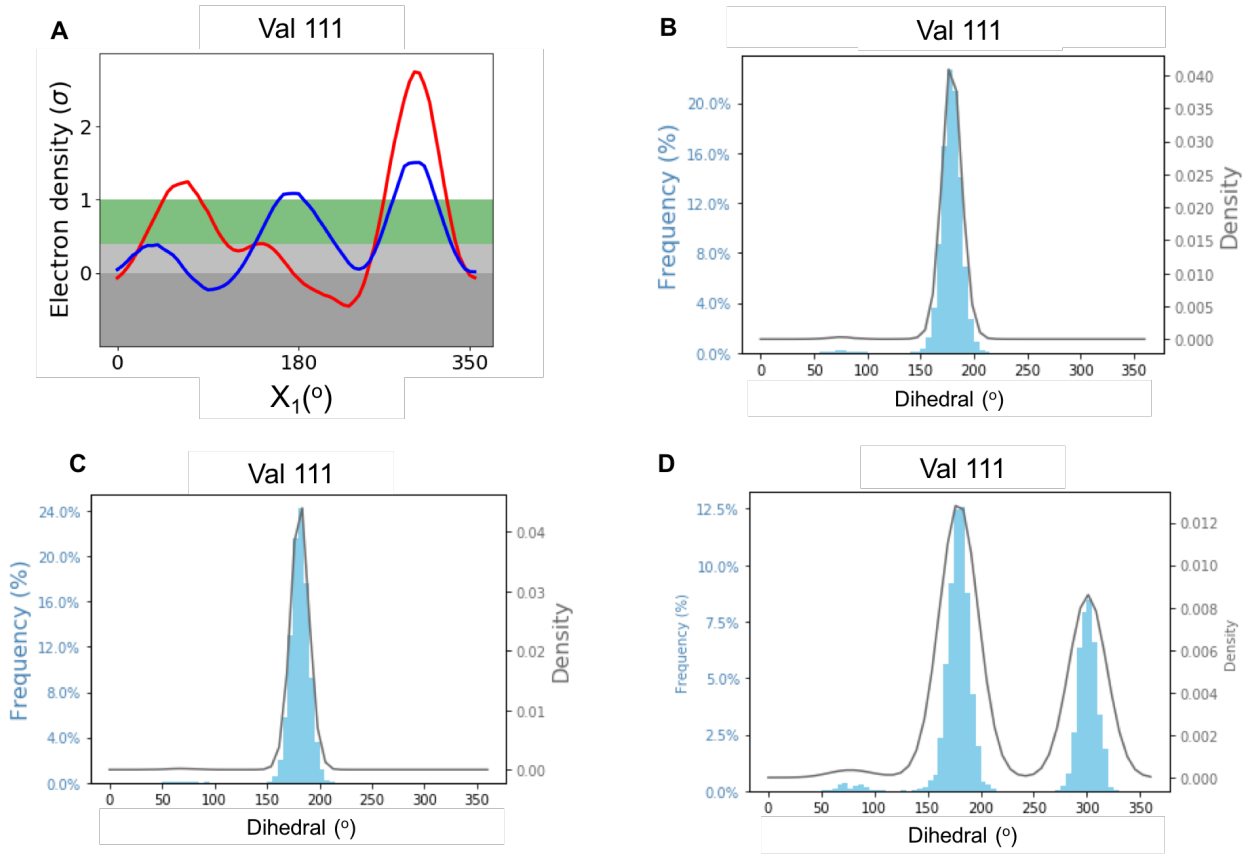

Figure S17. BLUES simulations recovered additional rotamers observed experimentally for Val111 in L99A:iodobenzene complex. 100 ns of MD simulations were done on: B) the cryo structure of L99A:iodobenzene complex (PDB code: 3dn4), C) the RT structure of L99A:iodobenzene complex. D) 100 ns of BLUES simulations on the RT structure of L99A:iodobenzene complex, where we enhanced the side chain sampling of Val111 and Leu118. Compared to standard MD (panels B and C), BLUES simulations using the RT structure recovered an additional rotamer observed experimentally around 180 degrees, which is the dominant experimental rotamer with RTX. The rotamers in panels B, C, and D are plotted using Gaussian kernel density estimation. The PDB code used to prepare the L99A:iodobenzene complex is 3dn4.

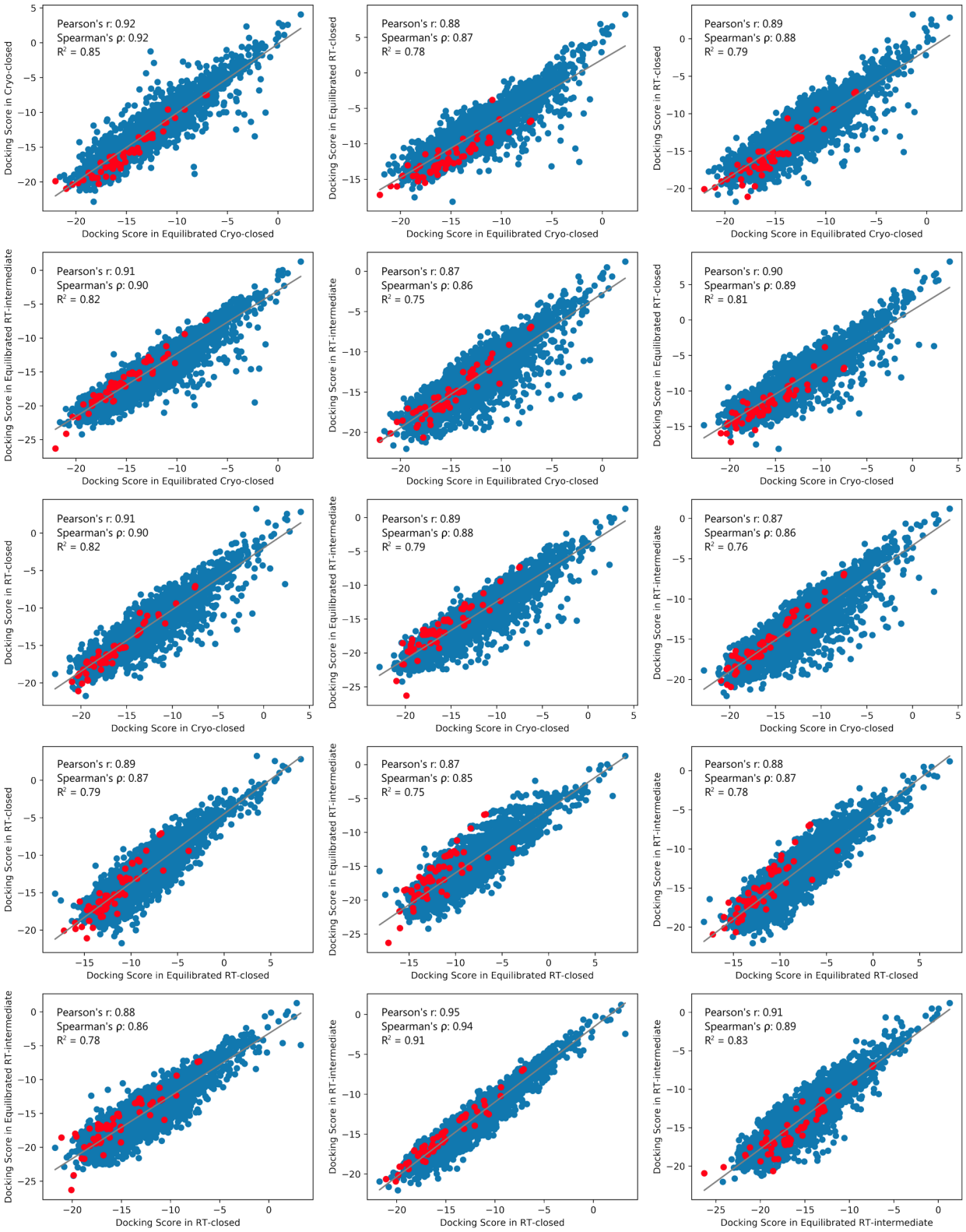

Figure S18: The correlation coefficients show that OEdock scores of the different L99A structure combinations are positively correlated. Correlation coefficients of the docking scores of

L99A compounds when docked in different structures using OEdock. The plots represent the scores of the docked compounds in structure X vs structure Y with X and Y representing one of the following structures: i) the cryo structure of apo L99A with a closed F-helix conformation, ii) the room temperature structure of apo L99A with a closed F-helix conformation, iii) the room temperature structure of apo L99A with an intermediate F-helix conformation, iv) the cryo structure of apo L99A with a closed F-helix conformation extracted after 50 ns of MD simulations, v) the room temperature structure of apo L99A with a closed F-helix conformation extracted after 50 ns of MD simulations, or vi) the room temperature structure of apo L99A with an intermediate F-helix conformation extracted after 50 ns of MD simulations. We use “equilibrated” structures in the Figure above to refer to the structures extracted after 50 ns of MD simulations. R^2 is Pearson’s correlation coefficient. Known binders are shown in red.

Table S3. Details of OEdock RMSD calculations.

RMSD values corresponding to the active compounds which have available L99A co-crystal structures in the Protein Data Bank, when docked in A) the cryo structure of apo L99A, B) the room temperature structure of apo L99A with a closed F-helix conformation, C) the room temperature structure of apo L99A with an intermediate F-helix conformation, D) the cryo structure of apo L99A with a closed F-helix conformation extracted after 50 ns of MD simulations, E) the room temperature structure of apo L99A with a closed F-helix conformation extracted after 50 ns of MD simulations, and F) the room temperature structure of apo L99A with an intermediate F-helix conformation extracted after 50 ns of MD simulations. The RMSD were calculated relatively to the crystal structure of each ligand as reported in the table A and relatively to the RT structure of Toluene, o-xylene, and iodobenzene (Table B). For some ligands, the calculated RMSD values are affected by the choice of the protein structure. We used Chimera to align the active site of each L99A complex used for docking to its corresponding crystal structure. The alignment of the active site was done within 5 Å of the ligand. Then, we computed the RMSD values with Chimera, where we accounted for ligand symmetry.

A)

	Experimental structures			Equilibrated structures			PDB	Conformation
	A	B	C	D	E	F		
Benzene	1.30	1.71	1.72	1.70	1.43	1.52	4w52	C
Toluene	1.00	1.00	1.84	1.50	2.73	1.45	4w53	C
O-xylene	2.16	2.10	1.94	2.15	2.75	1.76	188l	I
Iodobenzene - A	0.91	1.27	0.94	1.29	3.66	0.91	3dn4	I
Iodobenzene - B	3.76	3.60	3.89	3.99	1.74	3.80	3dn4	I
Ethylbenzene	0.65	3.38	2.38	1.28	3.42	1.57	4w54	C
Propylbenzene	0.34	0.49	0.69	1.31	1.44	0.90	4w55	C
Butylbenzene	1.92	1.71	1.62	1.79	4.67	1.62	4w57	I
Sec-butylbenzene	2.60	2.68	1.65	2.28	1.86	1.38	4w56	I
Hexylbenzene	2.75	3.06	2.96	2.86	3.22	2.42	4w59	O
N-methylaniline	0.31	0.77	2.11	1.10	3.55	1.04	2otz	C
Isobutylbenzene	1.44	1.90	1.44	1.39	1.21	1.57	184l	C
P-xylene	1.54	1.17	1.03	1.19	0.93	0.68	187l	C
3-methylbenzylazide	1.42	1.82	0.83	1.44	5.06	1.57	2rb2	I
2-ethoxyphenol	2.24	2.17	2.21	2.44	0.71	2.20	2rb1	I
2,6-difluorobenzyl bromide	0.62	1.05	1.39	1.35	3.53	2.43	2rb0	I
1-methylpyrrole	1.52	1.57	1.52	2.20	2.92	1.54	2ou0	C
1,2-dichlorobenzene	3.01	3.05	3.90	1.73	1.37	3.21	2oty	I
4-(methylthio)nitrobenzene	2.00	1.89	1.51	4.84	5.11	1.30	2raz	I
Indene	1.14	1.57	1.63	3.10	3.22	1.29	183l	I
Benzofuran	1.05	0.46	2.07	0.65	3.09	2.17	182l	C
Indole	1.98	3.74	3.74	1.00	3.71	1.64	185l	C
Pentylbenzene	3.56	3.51	3.02	3.13	3.58	3.37	4w58	O

B)

	Experimental structures			Equilibrated structures			Conf
	A	B	C	D	E	F	
Toluene	0.98	1.02	1.84	1.53	2.75	1.21	C
O-xylene	1.82	1.73	1.64	1.92	2.74	1.79	I
Iodobenzene - A	0.85	1.26	0.87	0.89	3.67	0.86	I
Iodobenzene - B	3.88	3.72	3.99	4.20	1.58	3.94	I

Table S4. Details of Autodock Vina RMSD calculations.

A) RMSD values corresponding to the active compounds which have available L99A co-crystal structures in the Protein Data Bank, when docked using Autodock Vina in A) the cryo structure of apo L99A, B) the room temperature structure of apo L99A with a closed F-helix conformation, C) the room temperature structure of apo L99A with an intermediate F-helix conformation, D) the cryo structure of apo L99A with a closed F-helix conformation extracted after 50 ns of MD simulations, E) the room temperature structure of apo L99A with a closed F-helix conformation extracted after 50 ns of MD simulations, and F) the room temperature structure of apo L99A with an intermediate F-helix conformation extracted after 50 ns of MD simulations. The RMSD were calculated relatively to the crystal structure of each ligand as reported in the table above. The F-helix conformation of L99A in each co-crystal structure (C: closed; I: intermediate; O: open) were evaluated using three reference structures (4w51 for closed, 4w55 for intermediate, and 4w59 for open). For some ligands, the calculated RMSD values are affected by the choice of the protein structure. We used Chimera to align the active site of each L99A complex used for docking to its corresponding crystal structure. The alignment of the active site was done within 5 Å of the ligand. Then, we computed the RMSD values with Chimera, where we accounted for ligand symmetry.

	Experimental structures			Equilibrated structures			PDB	Conformation
	A	B	C	D	E	F		
Benzene	0.94	1.68	1.20	0.69	0.82	0.77	4w52	C
Toluene	0.45	1.09	0.93	0.49	2.80	0.41	4w53	C
O-xylene	2.10	2.28	1.87	2.12	2.24	2.33	188l	I
Iodobenzene - A	0.73	1.02	0.59	1.00	1.42	0.54	3dn4	I
Iodobenzene - B	3.20	3.57	3.79	3.27	4.01	3.58	3dn4	I
Ethylbenzene	0.72	1.46	1.18	0.53	0.70	1.01	4w54	C
N-propylbenzene	0.71	1.40	1.01	0.63	0.74	0.82	4w55	C
N-butylbenzene	1.38	1.97	1.54	1.52	2.06	1.79	4w57	I
Sec-butylbenzene	1.53	1.70	1.59	1.51	4.40	1.30	4w56	I
N-hexylbenzene	3.07	2.66	5.11	3.13	2.93	2.96	4w59	O
N-methylaniline	0.30	1.32	0.56	0.27	1.30	0.84	2otz	C
Isobutylbenzene	0.66	1.78	0.75	0.81	0.98	0.95	184l	C
P-xylene	0.97	1.45	0.76	1.05	1.33	0.67	187l	C
3-methylbenzylazide	1.26	2.31	2.11	1.54	2.64	1.92	2rb2	I
2-ethoxyphenol	0.45	2.61	0.67	0.55	0.89	0.49	2rb1	I
2,6-difluorobenzyl bromide	0.78	2.10	0.58	0.72	3.39	1.42	2rb0	I
1-methylpyrrole	0.60	1.02	1.12	0.55	2.61	0.40	2ou0	C
1,2-dichlorobenzene	2.97	3.96	3.04	2.91	3.05	3.03	2oty	I
Indene	1.12	1.25	0.63	1.22	3.21	0.61	183l	I
Benzofuran	1.98	2.11	0.90	2.12	3.21	1.98	182l	C
Indole	0.37	1.02	2.26	0.36	3.70	1.53	185l	C
Pentylbenzene	3.41	3.49	3.06	3.71	3.57	3.44	4w58	O

B) RMSD values corresponding to toluene, o-xylene, iodobenzene, when docked using Autodock Vina in A) the cryo structure of apo L99A, B) the room temperature structure of apo L99A with a closed F-helix conformation, C) the room temperature structure of apo L99A with an intermediate F-helix conformation, D) the cryo structure of apo L99A with a closed F-helix conformation extracted after 50 ns of MD simulations, E) the room temperature structure of apo L99A with a closed F-helix conformation extracted after 50 ns of MD simulations, and F) the room temperature structure of apo L99A with an intermediate F-helix conformation extracted after 50 ns of MD simulations. The RMSD were calculated relatively to the RT structure of each ligand. For some ligands, the calculated RMSD values are affected by the choice of the protein structure. We used Chimera to align the active site of each L99A complex used for docking to its corresponding crystal structure. The alignment of the active site was done within 5 Å of the ligand. Then, we computed the RMSD values with Chimera, where we accounted for ligand symmetry.

	Experimental structures			Equilibrated structures			Conformation
	A	B	C	D	E	F	
Toluene	0.42	1.03	0.93	0.74	1.86	0.39	C
O-xylene	1.82	1.95	1.57	1.81	4.09	1.87	I
Iodobenzene - A	0.72	0.92	0.53	1.04	1.91	0.54	I
Iodobenzene - B	3.73	4.04	3.89	3.73	2.79	3.70	I

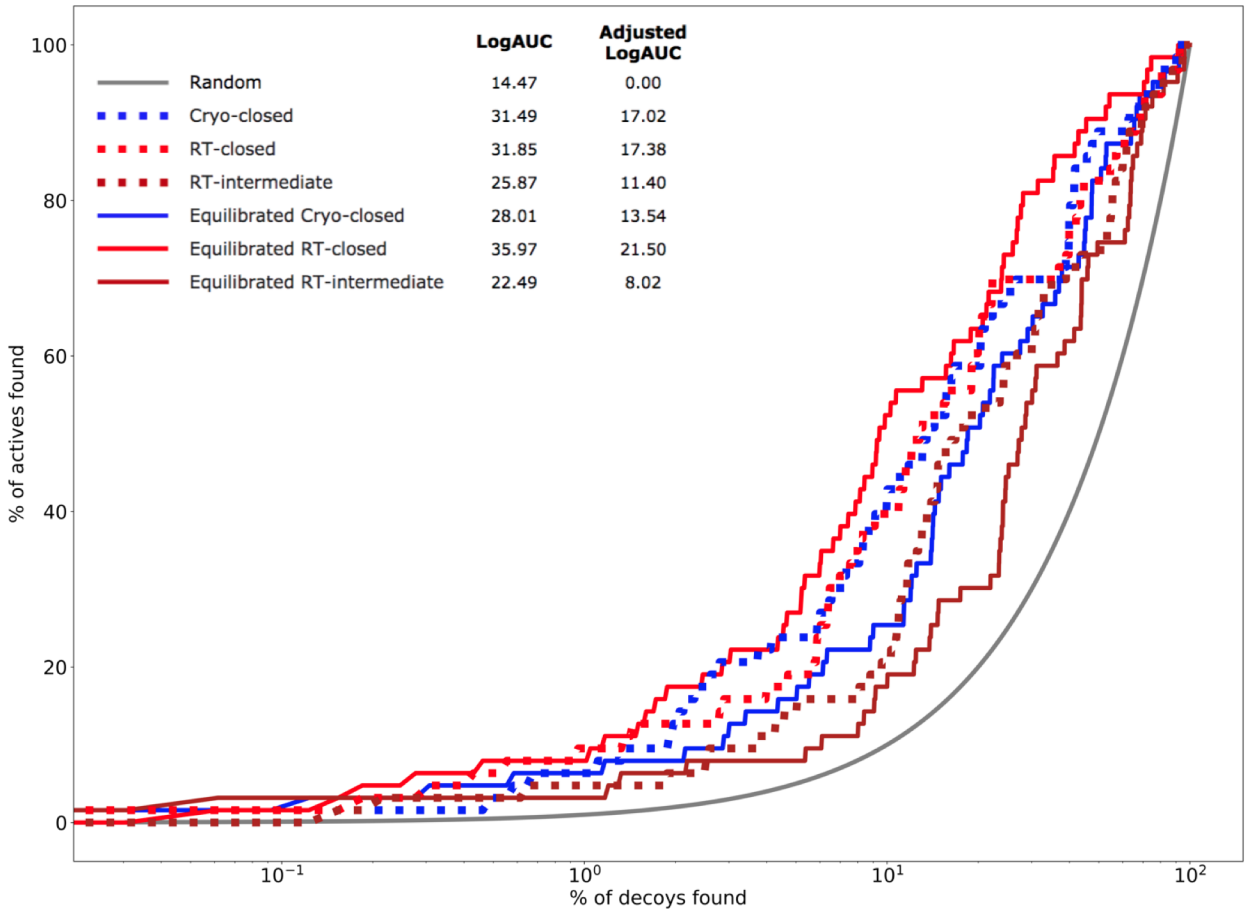

Figure S19. The choice of the protein structure impacts docking. Enrichment plots (semilog ROC plots) using a library of L99A decoys and active compounds showing the % of active compounds found. Docking was done using OEdock in i) the cryo structure of apo L99A, ii) the room temperature structure of apo L99A with a closed F-helix conformation, iii) the room temperature structure of apo L99A with an intermediate F-helix conformation, iv) the cryo structure of apo L99A with a closed F-helix conformation extracted after 50 ns of MD simulations, v) the room temperature structure of apo L99A with a closed F-helix conformation extracted after 50 ns of MD simulations, and vi) the room temperature structure of apo L99A with an intermediate F-helix conformation extracted after 50 ns of MD simulations. We use "equilibrated" structures in the Figure above to refer to the structures extracted after 50 ns of MD simulations. A comparison of the plots and the adjusted logAUC values shows that the choice of the structure impacts docking. We found that the early enrichment was improved the most with the equilibrated room temperature structure of L99A with a closed F-helix conformation compared to the other five structures. Also, L99A with a closed F-helix conformation shows a better early enrichment than L99A with an intermediate F-helix conformation. The plots and the adjusted logAUC were calculated as described by Mysinger and Shoichet. 3152 decoys were obtained using DUD-E.

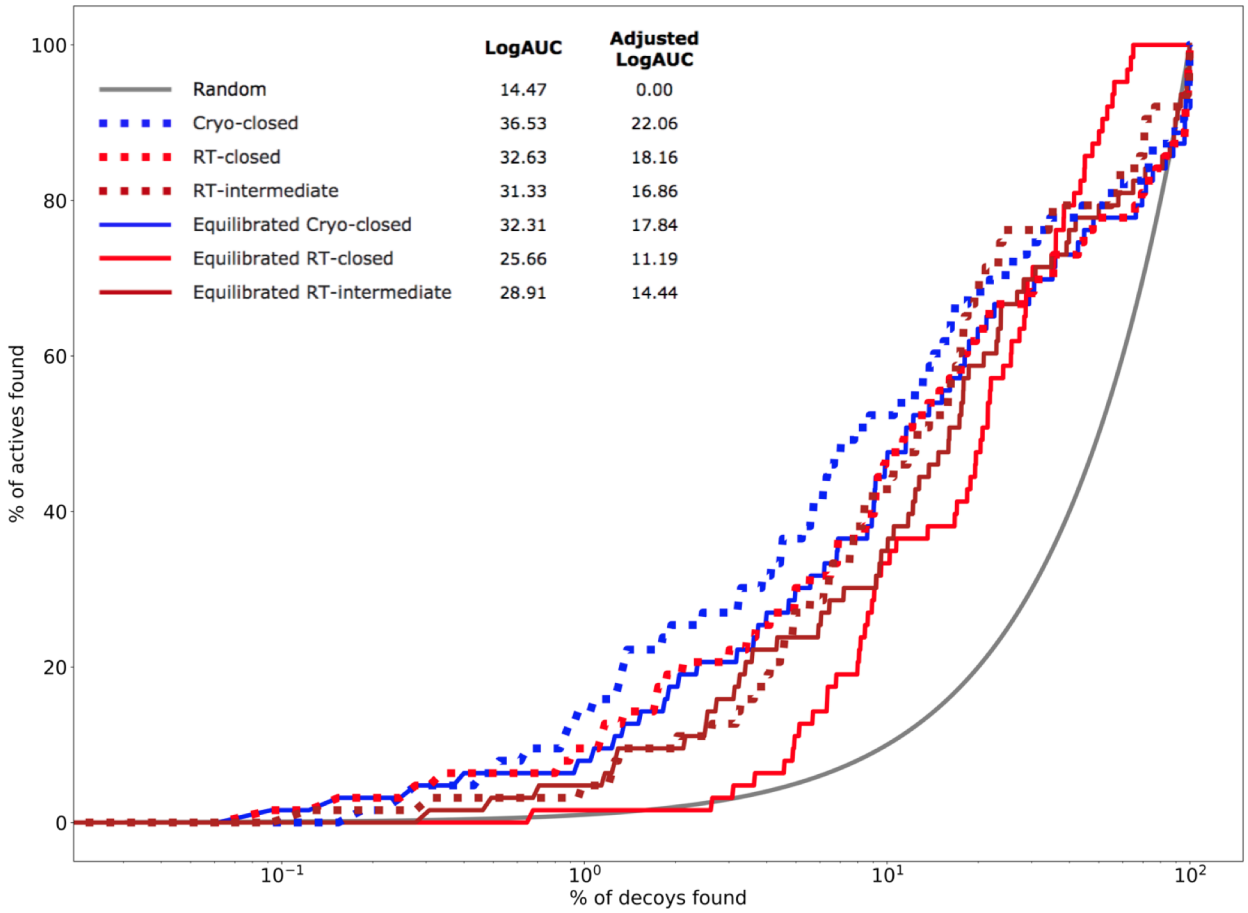

Figure S20. The choice of the protein structure impacts docking. Enrichment plots (semilog ROC plots) using a library of L99A decoys and active compounds showing the % of active compounds found. Docking was done using Autodock Vina in i) the cryo structure of apo L99A, ii) the room temperature structure of apo L99A with a closed F-helix conformation, iii) the room temperature structure of apo L99A with an intermediate F-helix conformation, iv) the cryo structure of apo L99A with a closed F-helix conformation extracted after 50 ns of MD simulations, v) the room temperature structure of apo L99A with a closed F-helix conformation extracted after 50 ns of MD simulations, and vi) the room temperature structure of apo L99A with an intermediate F-helix conformation extracted after 50 ns of MD simulations. We use “equilibrated” structures in the Figure above to refer to the structures extracted after 50 ns of MD simulations. A comparison of the plots and the adjusted logAUC values shows that the choice of the structure impacts docking. We found that the early enrichment was improved the most with the cryo structure of L99A with a closed F-helix conformation compared to the other five structures. The plots and the adjusted logAUC were calculated as described by Mysinger and Shoichet. 3152 decoys were obtained using DUD-E.

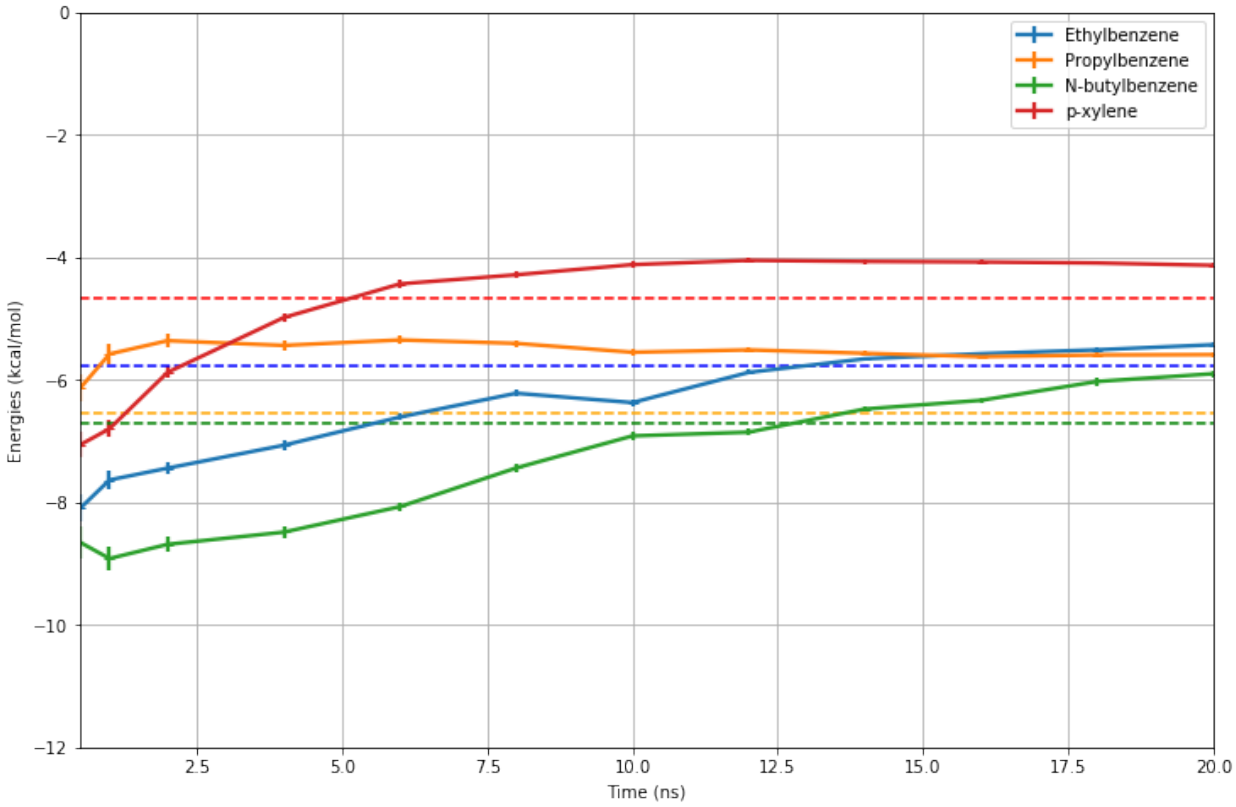

Figure S21. Computed binding free energies are close to their respective experimental binding free energies. Computed absolute binding free energy calculations of L99A complexed with ethylbenzene in blue, propylbenzene in orange, n-butylbenzene in green, and p-xylene in red. The respective experimental binding affinities are represented in dashed lines using the same color code and reported in Table 1. The calculated binding free energies are close to the experimental binding free energies with an error less than 1 kcal/mol. The absolute binding free energies were computed in explicit solvent after 20 ns/thermodynamic state using a thermodynamic cycle of 29 states.

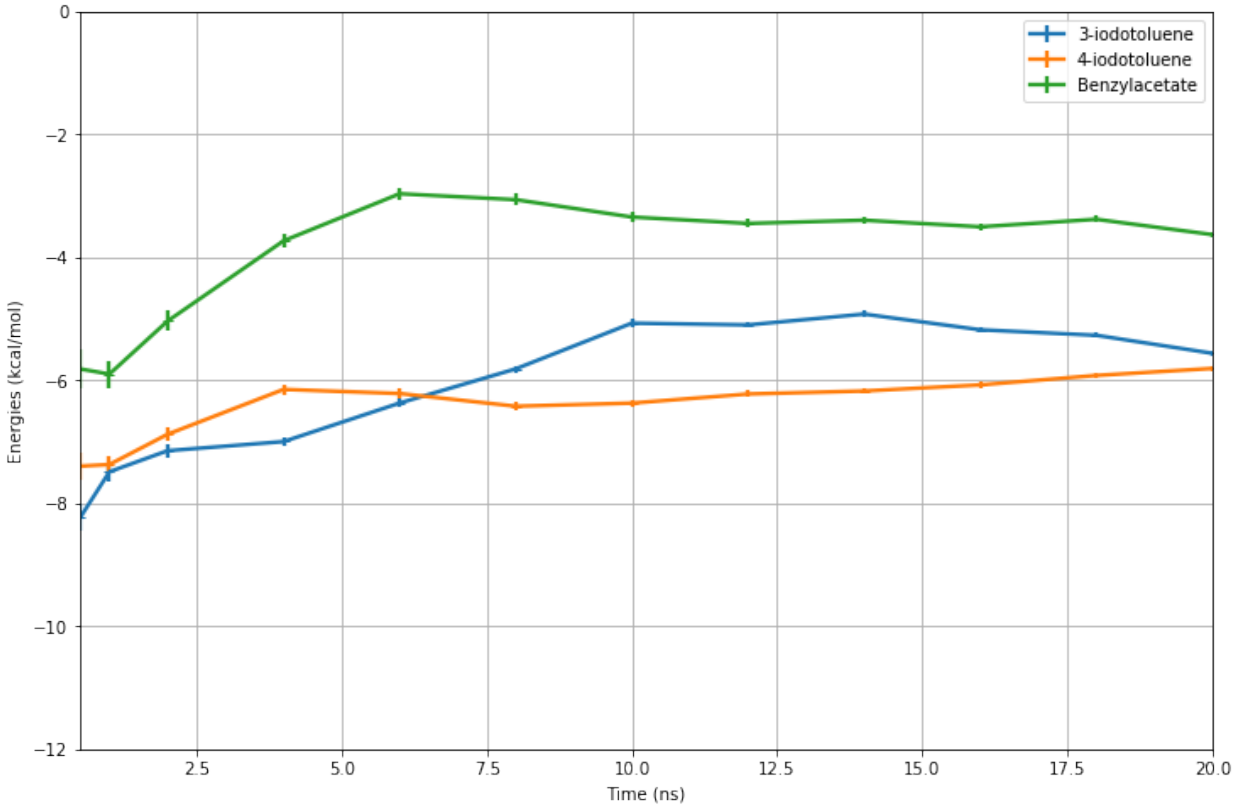

Figure S22. Computed absolute binding free energy calculations of L99A complexed with 3-iodotoluene in blue, 4-iodotoluene in orange, and benzylacetate in green. The absolute binding free energies were computed in explicit solvent after 20 ns/thermodynamic state using a thermodynamic cycle of 29 states. Overall, the convergence of the binding free energies occurred around 10 ns/thermodynamic state. There are no experimental binding affinities available for these complexes.

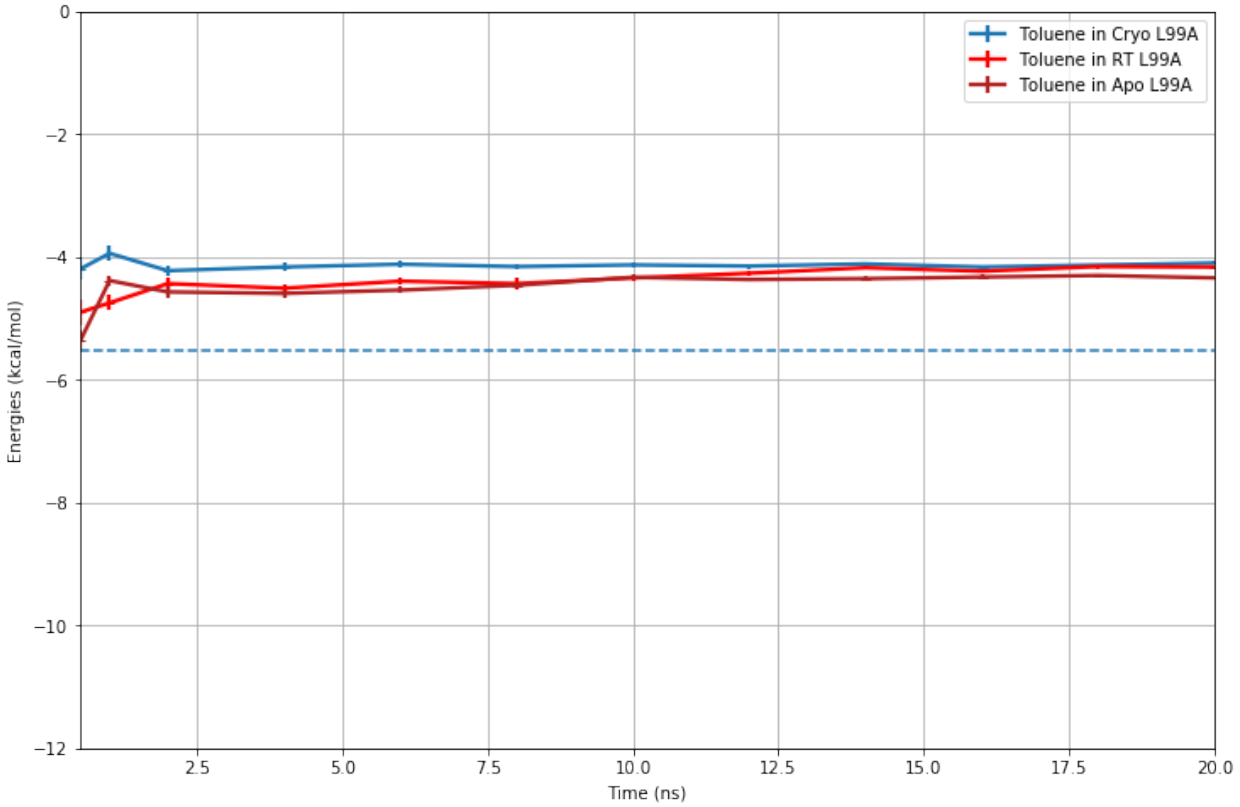

Figure S23. Using different L99A:toluene complexes, we reached the same binding free energy value. Computed absolute binding free energy calculations of L99A complexed with toluene using: i) the cryo structure of L99A:toluene (in blue; PDB code: 4W53), ii) the RT structure of L99A:toluene (in red), and iii) the RT structure of apo L99A (in –dark red). The respective experimental binding free energy is represented in a blue dashed line and reported in Table 1. The three computed binding free energies converged to almost the same value: -4.10 kcal/mol for the cryo structure of L99A: toluene (Table 1), -4.16 kcal/mol for the RT structure of L99A:toluene (Tables 1 and S30), and -4.34 kcal/mol (Table S30) for toluene in the RT structure of apo L99A. The absolute binding free energies were computed in explicit solvent after 20 ns/thermodynamic state using a thermodynamic cycle of 29 states.

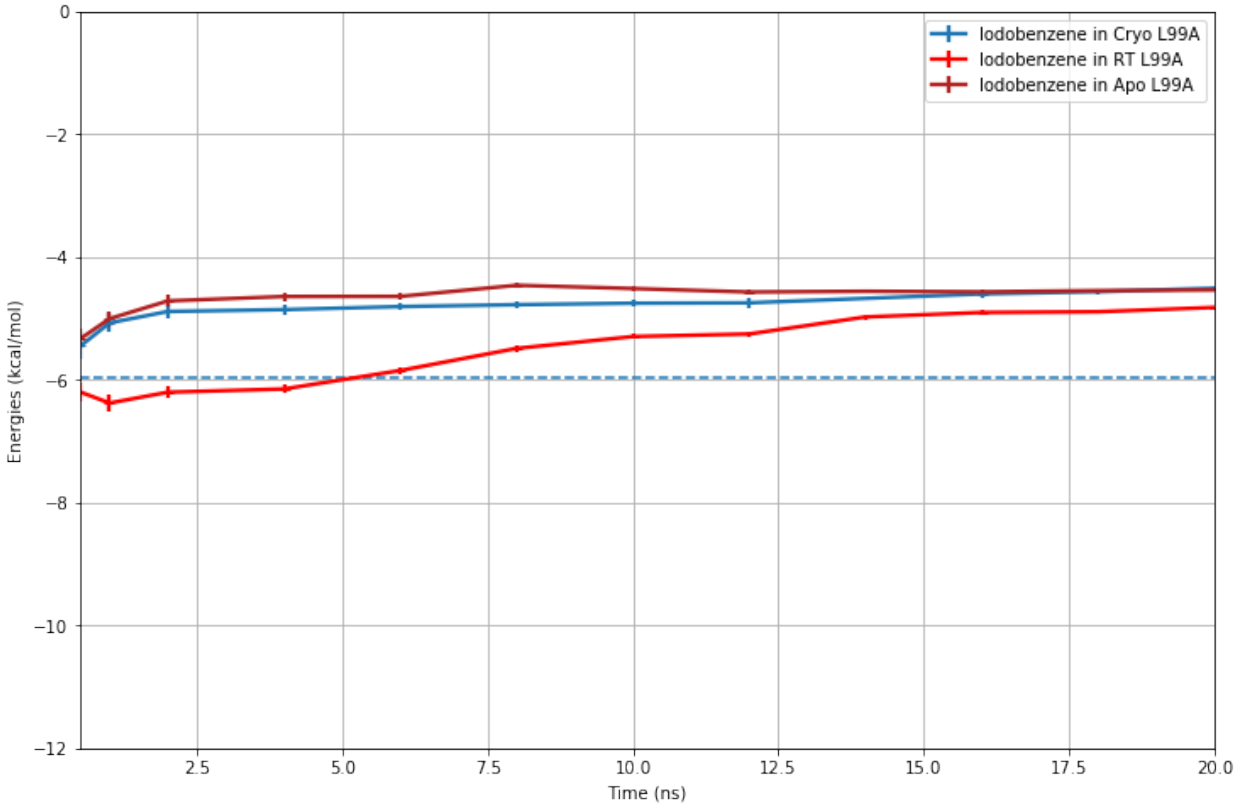

Figure S24. The RT structure of L99A:iodobenzene gave the closest binding free energy to the experimental one. Computed absolute binding free energy calculations of L99A complexed with iodobenzene using: i) the cryo structure of L99A:iodobenzene (in blue; PDB code: 3dn4), ii) the RT structure of L99A:iodobenzene (in red), and iii) in the RT structure of apo L99A (in dark red). The respective experimental binding free energy is represented in a blue dashed line and reported in Table 1. The binding free energy obtained using the room temperature structure of L99A:iodobenzene (Table 1) is more favorable and closer to the experimental binding free energy, compared to the binding free energy done using the cryo structure of L99A:iodobenzene and the binding free energy done using the apo-L99A:iodobenzene (Table 1).

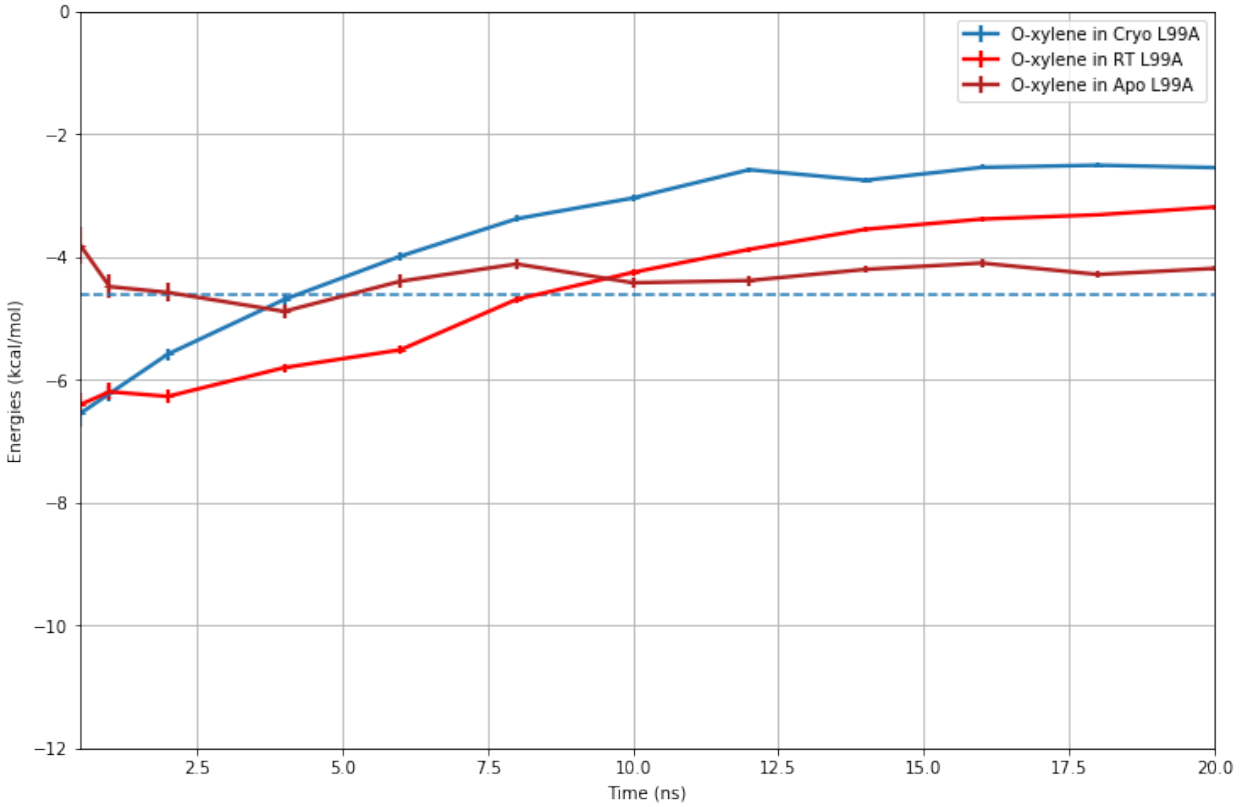

Figure S25. The RT structures gave close binding free energies to the experimental one. Computed absolute binding free energy calculations of L99A complexed with o-xylene: i) in the cryo structure of L99A:o-xylene (in blue; PDB code: 188L), ii) in the RT structure of L99A:o-xylene (in red), and iii) in the RT structure of apo L99A (in dark red). The respective experimental binding free energy is represented in a blue dashed line and reported in Table 1. The binding free energies obtained using the room temperature structure of L99A:o-xylene and o-xylene in the room temperature structure of apo L99A (Table 1) are more favorable and closer to the experimental binding free energy, compared to the binding free energy done using the cryo structure of L99A:o-xylene (Table 1).

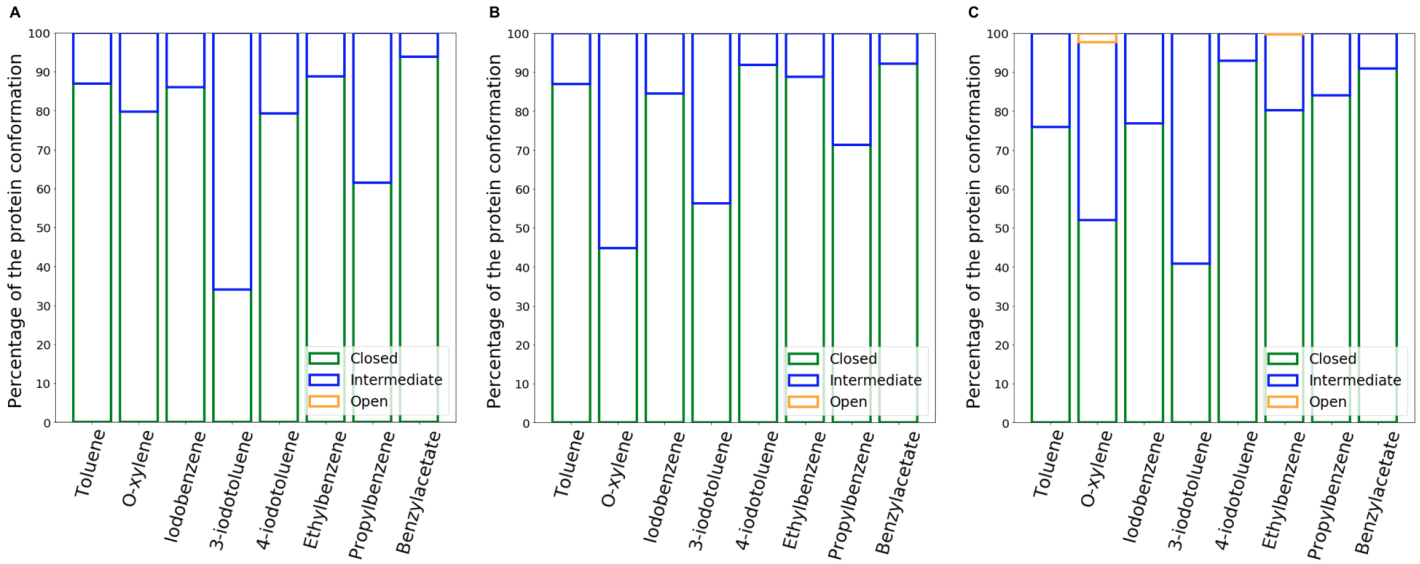

Figure S26. The F-helix conformational state is independent from the starting conformation. The histograms represent the percentage of the F-helix conformational states for L99A complexed with toluene, o-xylene, iodobenzene, 3-iodotoluene, 4-iodotoluene, ethylbenzene, propylbenzene, and benzylacetate during 100 ns of MD simulations starting with: A) L99A with a closed F-helix conformation (PDB code 4W51), B) L99A with an intermediate F-helix conformation (PDB code 4W55), and C) L99A with an open F-helix conformation (PDB code 4W59). The populations of the conformational state during MD were calculated as described by Lim et. al. [30], by computing the RMSD of the protein backbone atoms spanning the F-helix relative to their positions in the reference structures of the closed (PDB code 4W51), intermediate (PDB code 4W55), and open (PDB code 4W59) F-helix conformations.

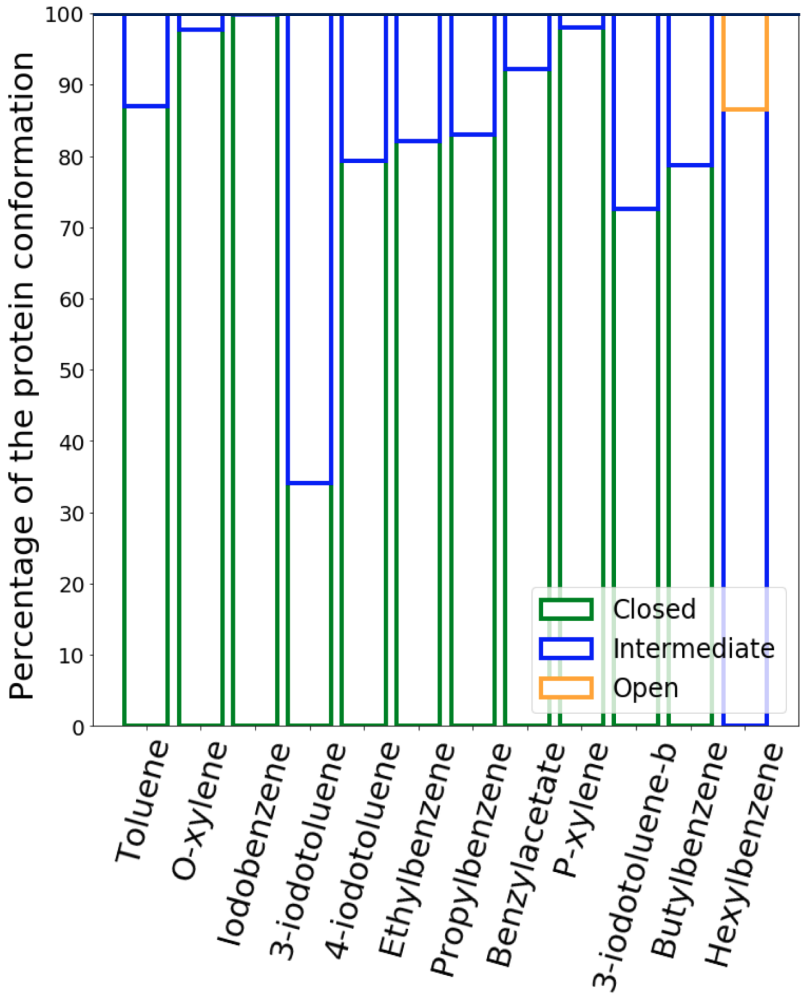

Figure S27. All these L99A complexes adopt a dominant closed F-helix conformation. The histograms represent the percentage of the F-helix conformational states for L99A bound to toluene (PDB code: 4W53), ethylbenzene (PDB code: 4W54), propylbenzene (PDB code: 4W55), n-butylbenzene (PDB code: 4W57), iodobenzene (PDB code: 3DN4) , p-xylene (PDB code: 187L), and o-xylene (PDB code: 188L). There are no crystal structures available in the RCSB Protein Data Bank for L99A complexed with 3-iodotoluene, 4-iodotoluene, and benzylacetate. We manually created benzylacetate in Chimera based on the structure of butylbenzene (PDB code:4w57) and the receptor structure prepared from the L99A:butylbenzene complex was used to form the L99A:benzylacetate complex. The starting conformation of the complex L99A:3-iodotoluene-b was taken from Gill et al. 2018 (9). For L99A:4-iodotoluene, we used the same PDB file of L99A:3-iodotoluene (Gill et al., 2018) for the receptor structure, and to generate the 3D structure of 4-iodotoluene based on that of 3-iodotoluene, using Chimera. For L99A:3-iodotoluene, we have also prepared a second complex, where we used the PDB structure of L99A:toluene (PDB code: 4W53) to

manually generate the structure of 3-iodotoluene using Chimera, with respect to the receptor structure of the same PDB file (4w53).The populations of the conformational state during MD were calculated as described by Lim et. al. [30], by computing the RMSD of the protein backbone atoms spanning the F-helix relative to their positions in the reference structures of the closed (PDB code 4W51), intermediate (PDB code 4W55), and open (PDB code 4W59) F-helix conformations.

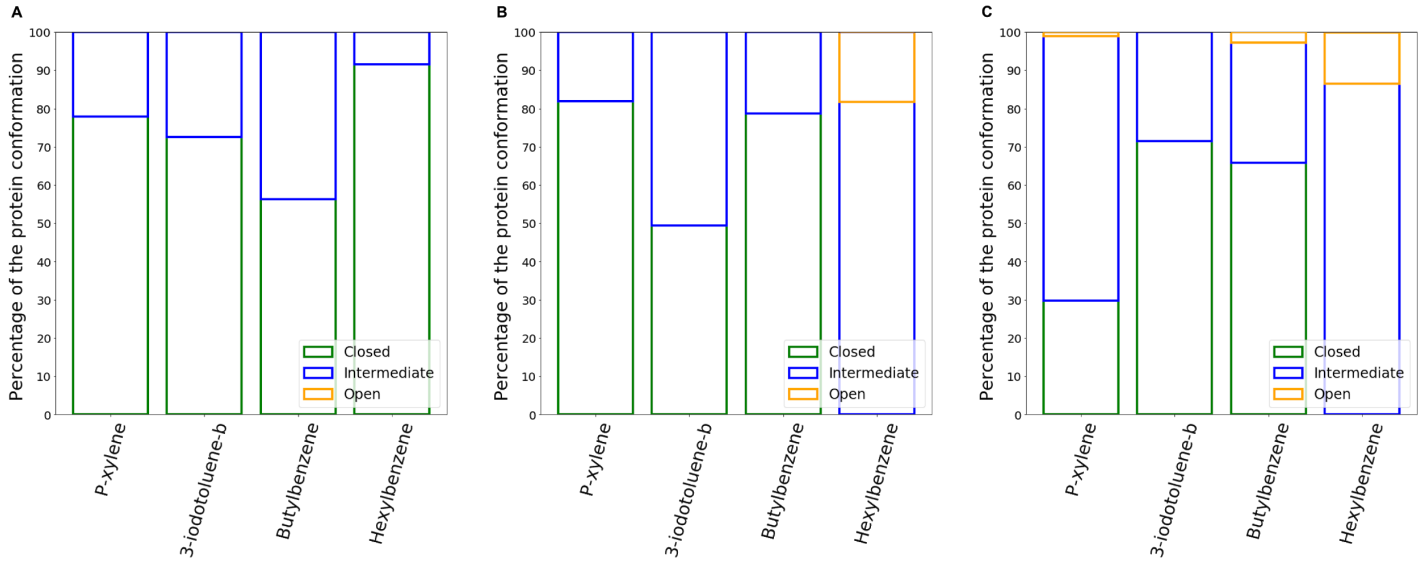

Figure S28. The F-helix conformational state depends on the starting conformation for L99A bound to p-xylene, 3-iodotoluene, butylbenzene, and hexylbenzene. Histograms representing the percentage of the F-helix conformational states for L99A complexed with p-xylene, 3-iodotoluene, butylbenzene, and, hexylbenzene during 100 ns of MD simulations starting with: A) L99A with a closed F-helix conformation (PDB code 4W51), B) L99A with an intermediate F-helix conformation (PDB code 4W55), and C) L99A with an open F-helix conformation (PDB code 4W59). The binding mode of 3-iodotoluene was taken from a BLUES study published previously [3]. The populations of the conformational state during MD were calculated as described by Lim et. al. [30], by computing the RMSD of the protein backbone atoms spanning the F-helix relative to their positions in the reference structures of the closed (PDB code 4W51), intermediate (PDB code 4W55), and open (PDB code 4W59) F-helix conformations.

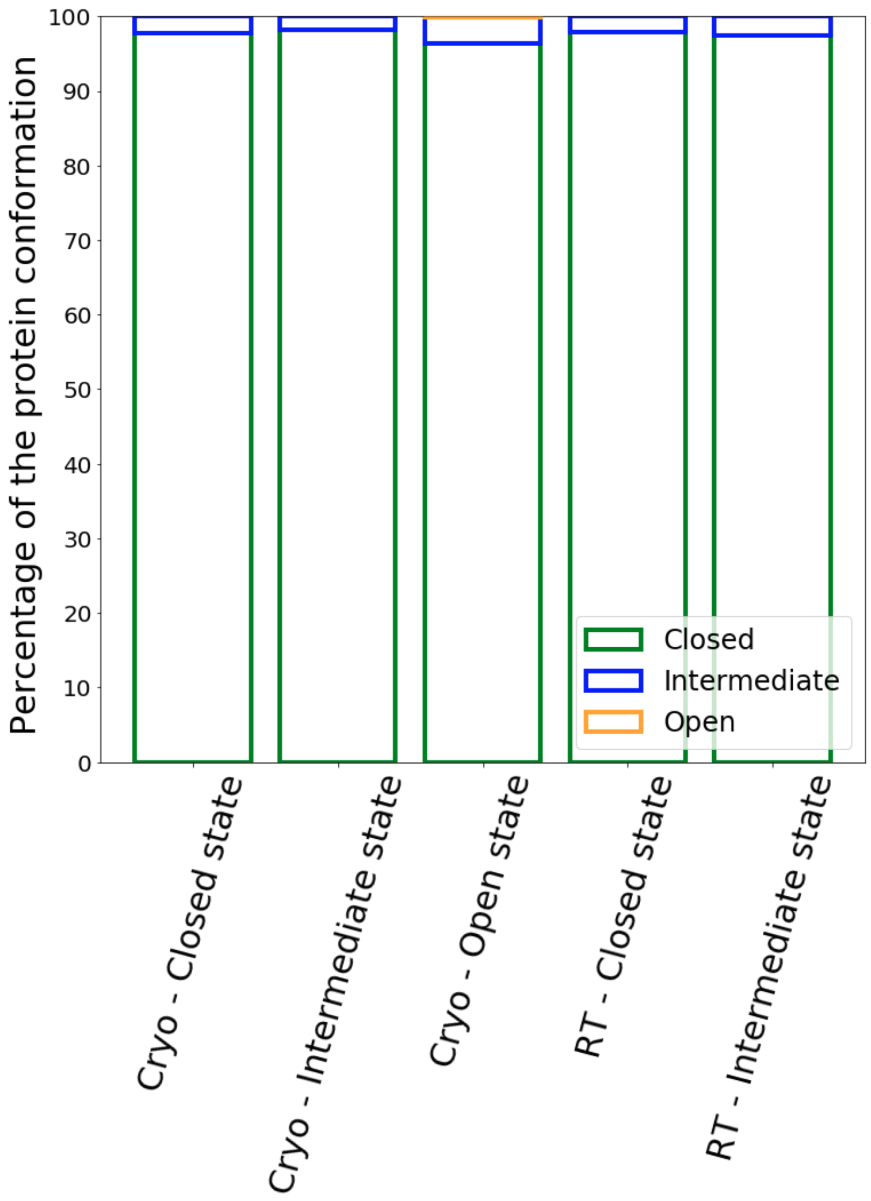

Figure S29. A dominant closed F-helix conformation was detected during all the simulations performed on apo L99A systems. Histogram representing the percentage of the F-helix conformational states for apo L99A during 1us of MD simulations starting with: L99A with a closed F-helix conformation (PDB code 4W51), L99A with an intermediate F-helix conformation (PDB code 4W55), and L99A with an open F-helix conformation (PDB code 4W59). The open conformation was observed only when starting the MD simulations with an open F-helix conformation during 0.14% of the simulations. Also, we performed MD simulations (100 ns) on the RT structure of apo L99A starting with a closed and an intermediate F-helix

conformation. The populations of the conformational state during MD were calculated as described by Lim et. al., “by computing the RMSD of the protein backbone atoms spanning the F-helix” relative to their positions in the reference structures of the closed (PDB code 4W51), intermediate (PDB code 4W55), and open (PDB code 4W59) F-helix conformations.

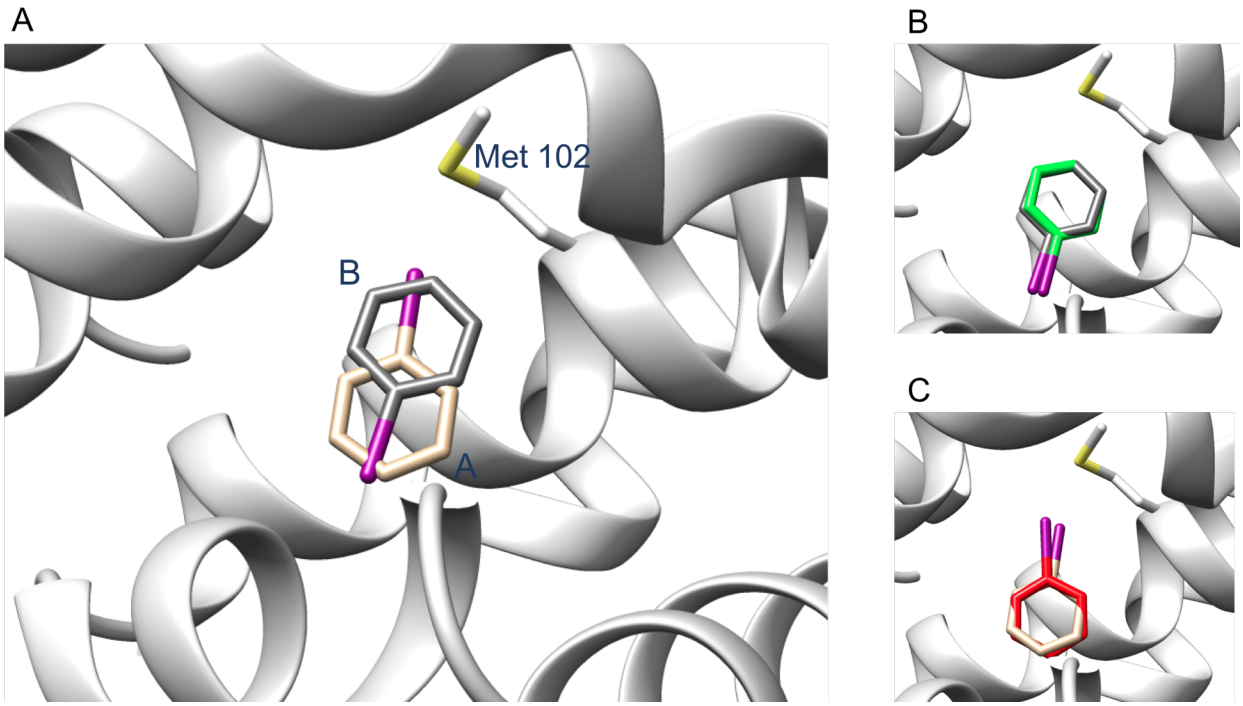

Figure S30. Starting with the binding mode A, BLUES simulations sampled the two crystallographic binding modes A and B. A) Figure showing the two crystallographic binding modes A (in beige) and B (in grey) of iodobenzene complexed with L99A (PDB code: 3dn4). Starting with the binding mode A, BLUES simulations sampled the two crystallographic binding modes A and B. Here, we extracted from the BLUES simulations: B) the binding pose which is closest to the crystallographic binding mode A as shown in red with a minimum RMSD of 0.52 Å and C) the binding pose which is closest to the crystallographic binding mode B as show in green with a minimum RMSD of 0.39 Å. (We have also calculated the RMSD of the binding poses shown in B and C relatively to the binding modes B and A of the room temperature structure and obtained 0.48 Å and 0.59 Å, respectively).

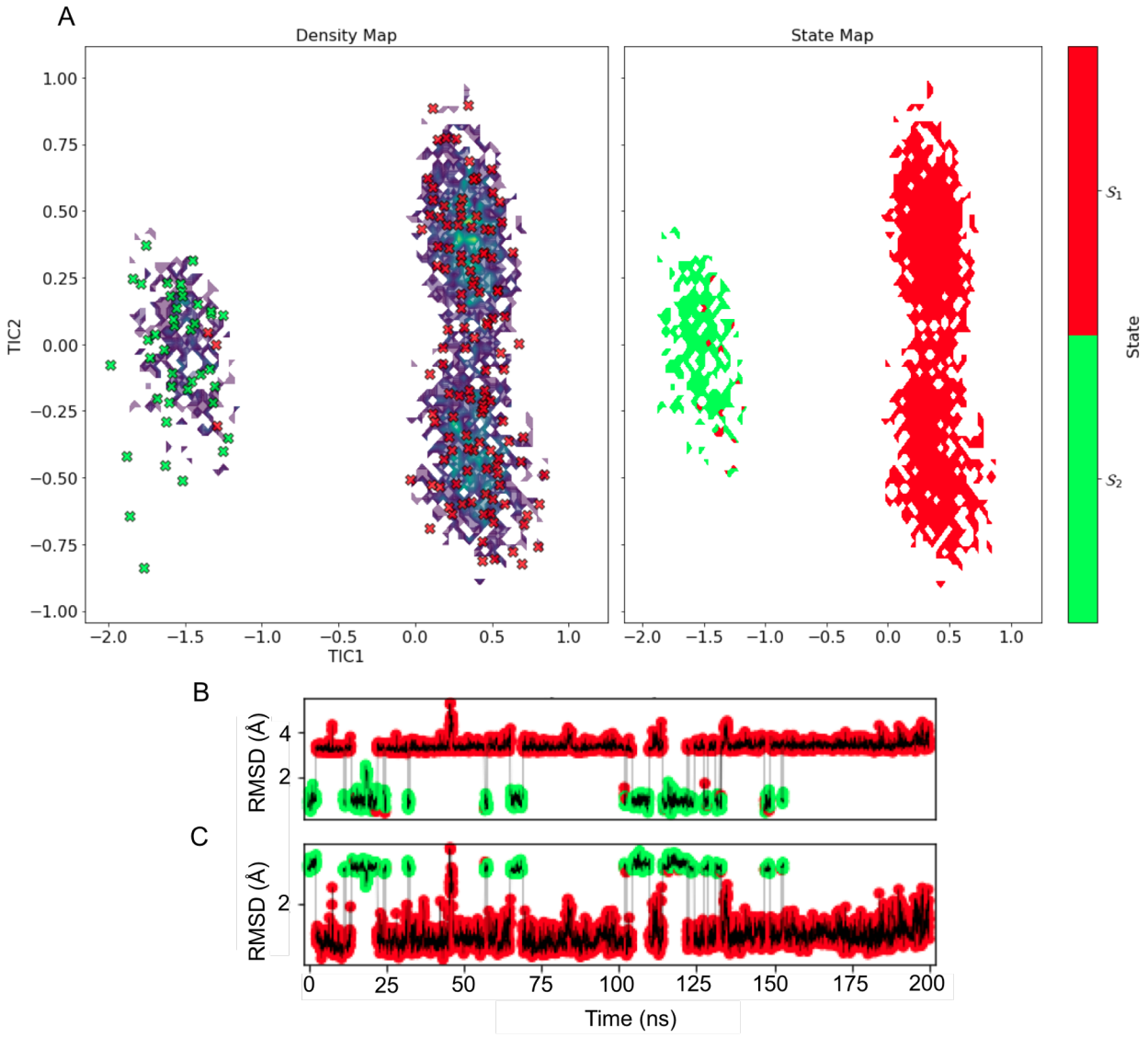

Figure S31. BLUES simulations on L99A complexed to iodobenzene sampled the two crystallographic binding modes. A) Shows time-lagged independent component analysis (TICA) plot for binding modes of iodobenzene in L99A using the first two TICA components from our BLUES simulations. Microstates are marked by Xs. We used PCCA to assign microstates to macrostates which define the stable binding modes identified during 200 ns of BLUES simulations. Macrostates represent different kinetically stable potential binding modes or structures that we observe, whereas microstates are local, structurally-similar states that may interconvert very rapidly. Using TICA (Time-lagged independent component analysis), we cluster the simulations frames into discrete microstates using k-means clustering. Then, we assign each

microstate to a number of macrostates or metastable binding modes, using PCCA (perron-cluster cluster analysis). Also shown are calculated RMSD values relative to the crystallographic binding modes. Panel (B) shows the RMSD values relative to the binding mode B, and panel (C) shows the RMSD values relative to the binding mode A. The crystallographic binding modes A and B are shown in tan and grey, respectively on Figure S30. Here the binding mode which is closest to the first crystallographic binding mode (A) is shown in red with a minimum RMSD of 0.52 Å and the binding mode which closest to the second crystallographic binding mode (B) is shown in green with a minimum RMSD of 0.39 Å. We started our BLUES simulations from crystallographic binding mode A. The PDB structure used to run BLUES simulations is 3dn4. Details regarding the tools used for TICA and PCCA approaches can be found in Lim et. al. 2019.

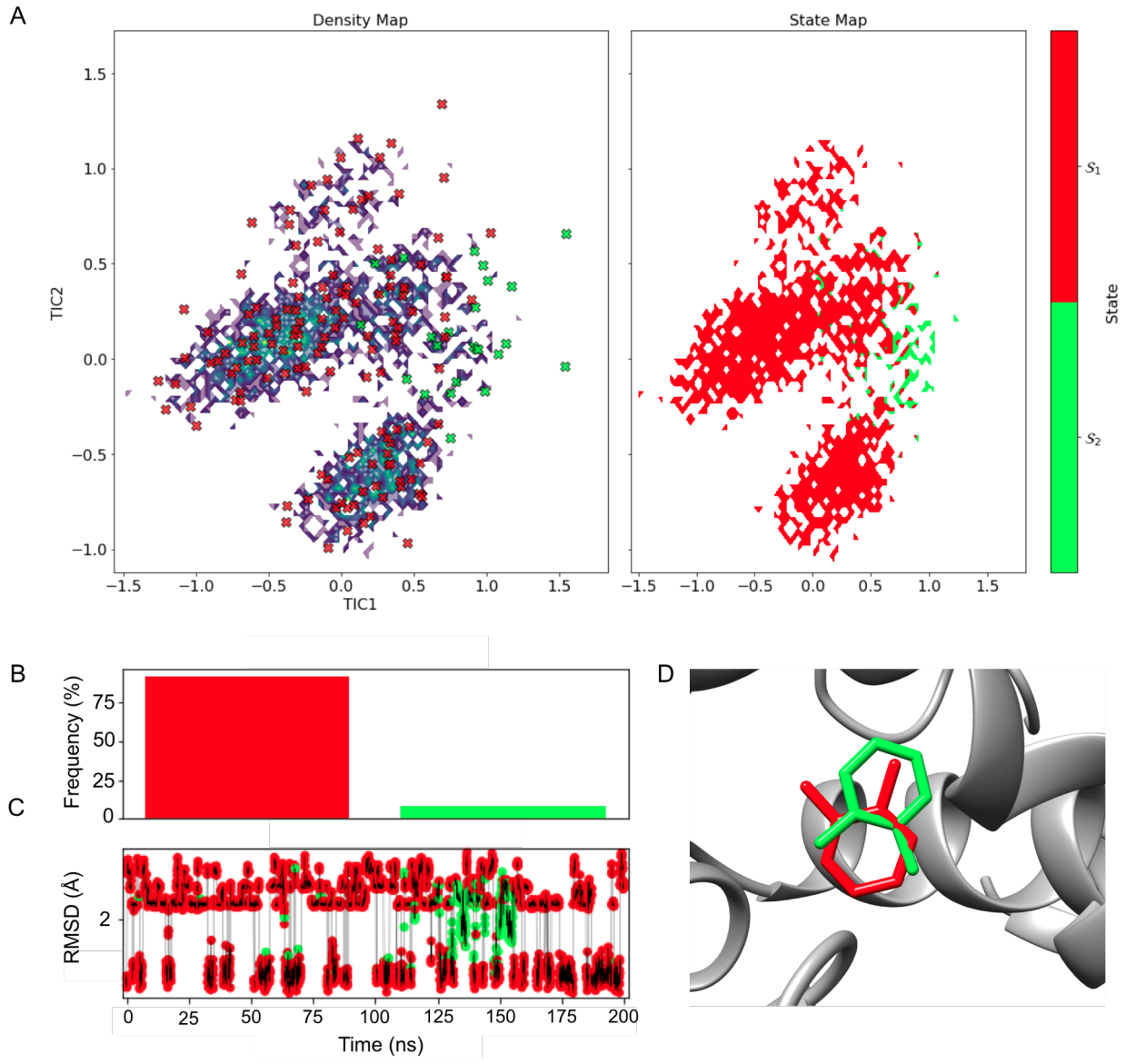

Figure S32. BLUES simulations on L99A complexed to o-xylene sampled two different binding modes. A) Time-lagged independent component analysis (TICA) plot for binding modes of o-xylene in L99A using the first two TICA components from our BLUES simulations. Microstates are marked by Xs. We used PCCA to assign microstates to macrostates which define the stable binding modes identified during 200 ns of BLUES simulations. Macrostates represent different kinetically stable potential binding modes or structures that we observe, whereas microstates are local, structurally-similar states that may interconvert very rapidly. Using TICA (Time-lagged independent component analysis), we cluster the simulations frames into discrete microstates using k-means clustering. Then, we assign each microstate to a number of macrostates or metastable binding modes, using PCCA (perron-cluster cluster analysis). B) Populations of the two binding modes of o-xylene identified during BLUES simulations. C) Calculated

RMSD relative to the crystallographic binding mode and the binding mode which is closest to the crystallographic binding mode is represented in red with a minimum RMSD of 0.39 Å. D) In red, we show the binding mode representing the red cluster and in green we show the binding mode representing the green cluster within L99A. The PDB structure used to run BLUES simulations is 188L. Details regarding the tools used for TICA and PCCA approaches can be found in Lim et al 2019.

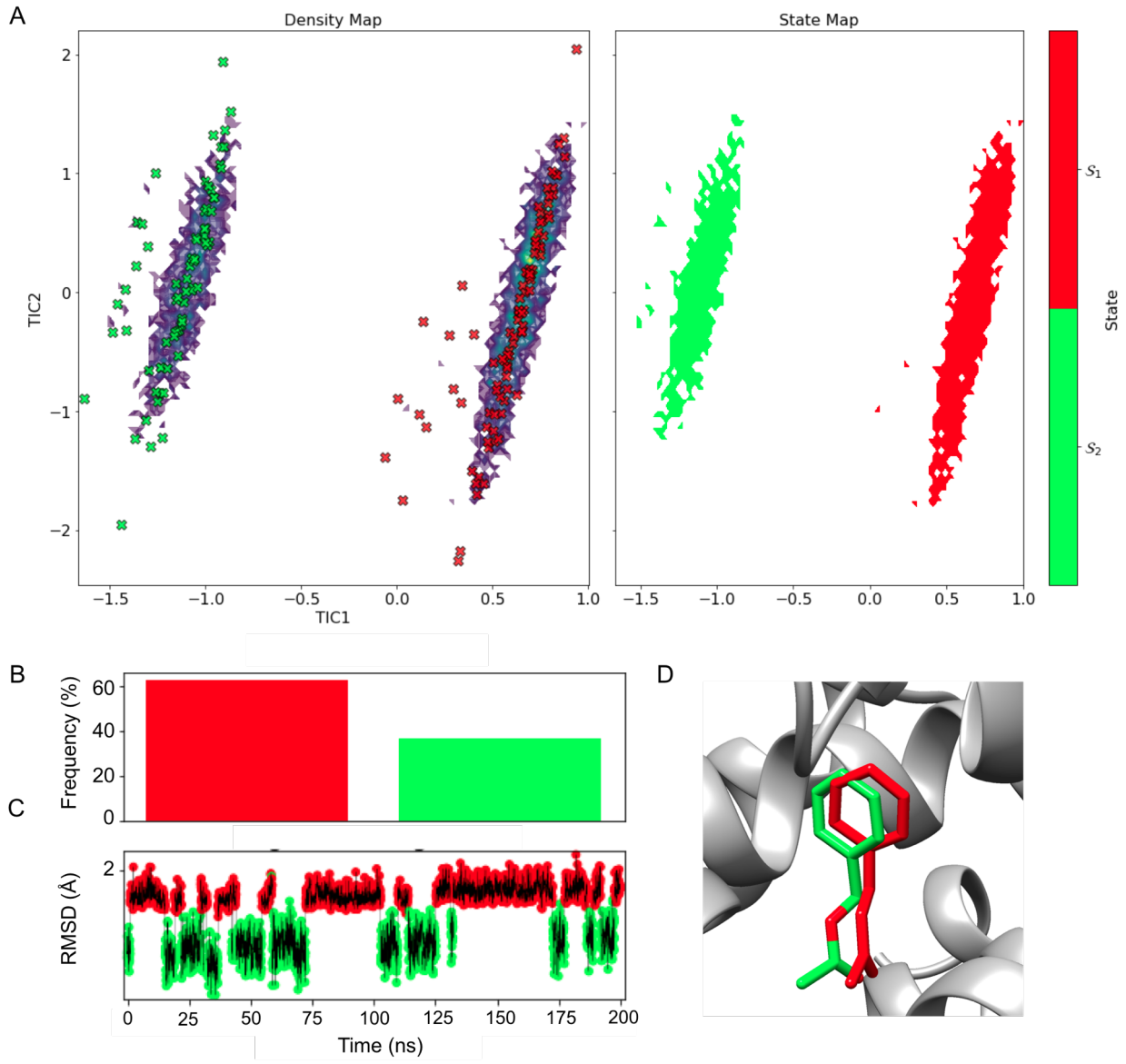

Figure S33. BLUES simulations on L99A complexed to benzylacetate sampled two different binding modes. A) Time-lagged independent component analysis (TICA) plot for binding modes of benzylacetate in L99A using the first two TICA components from our BLUES simulations. Microstates are marked by Xs. We used PCCA to assign microstates to macrostates which define the two stable binding modes of

benzylacetate identified during 200 ns of BLUES simulations. Macrostates represent different kinetically stable potential binding modes or structures that we observe, whereas microstates are local, structurally-similar states that may interconvert very rapidly. Using TICA (Time-lagged independent component analysis), we cluster the simulations frames into discrete microstates using k-means clustering. Then, we assign each microstate to a number of macrostates or metastable binding modes, using PCCA (perron-cluster cluster analysis). Macrostates represent different kinetically stable potential binding modes or structures that we observe, whereas microstates are local, structurally-similar states that may interconvert very rapidly. Using TICA (Time-lagged independent component analysis), we cluster the simulations frames into discrete microstates using k-means clustering. Then, we assign each microstate to a number of macrostates or metastable binding modes, using PCCA (perron-cluster cluster analysis). B) Populations of the two binding modes of benzylacetate identified during BLUES simulations. C) Calculated RMSD relative to the starting binding mode which was manually generated by modifying the 3D structure of butylbenzene (PDB code: 4W55). D) In red, we show the binding mode representing the red cluster and in green we show the binding mode representing the green cluster within L99A. The PDB structure of the receptor used to run BLUES simulations is 4W55. Details regarding the tools used for TICA and PCCA approaches can be found in Lim et al 2019 (15).

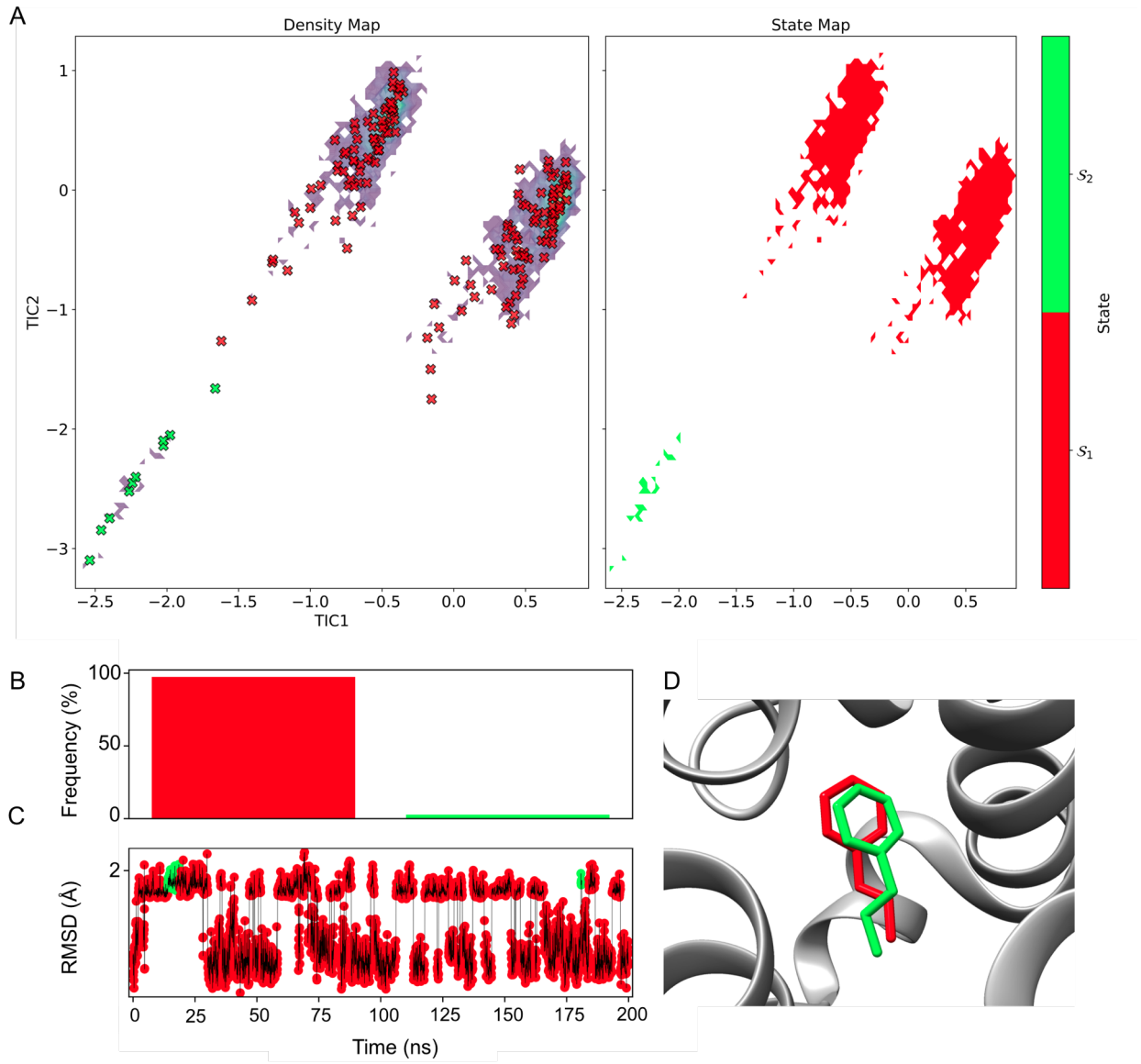

Figure S34. BLUES simulations on L99A complexed to propylbenzene sampled two different binding modes. A) Time-lagged independent component analysis (TICA) plot for binding modes of propylbenzene in L99A using the first two TICA components from our BLUES simulations. Microstates are marked by Xs. We used PCCA to assign microstates to macrostates which define the stable binding modes identified during 200 ns of BLUES simulations. Macrostates represent different kinetically stable potential binding modes or structures that we observe, whereas microstates are local, structurally-similar states that may interconvert very rapidly. Using TICA (Time-lagged independent component analysis), we cluster the simulations frames into discrete microstates using k-means clustering. Then, we assign each microstate to a number of macrostates or metastable binding modes, using PCCA (perron-cluster cluster analysis). B) Populations of the two binding modes of propylbenzene identified during BLUES simulations. C) Calculated

RMSD relative to the crystallographic binding mode and the binding mode which is closest to the crystallographic binding mode is represented in red with a minimum RMSD of 0.75 A. D) In red, we show the binding mode representing the red cluster and in green we show the binding mode representing the green cluster within L99A. The PDB structure of the receptor used to run BLUES simulations is 4W55. Details regarding the tools used for TICA and PCCA approaches can be found in Lim et al 2019 (15).

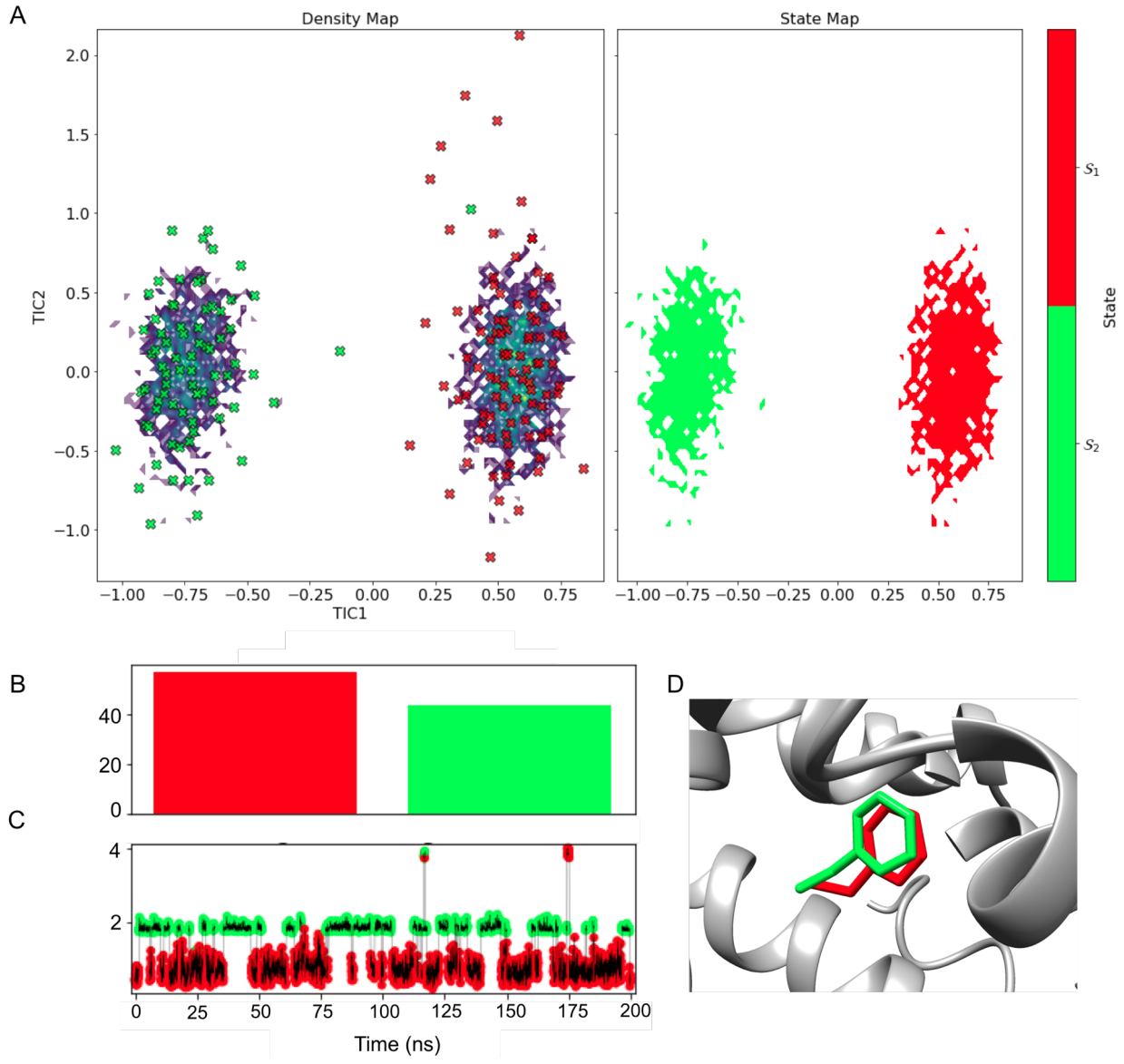

Figure S35. BLUES simulations on L99A complexed to ethylbenzene sampled two different binding modes. A) Time-lagged independent component analysis (TICA) plot for binding modes of ethylbenzene in L99A using the first two TICA components from our BLUES simulations. Microstates are marked by Xs. We used PCCA to assign microstates to macrostates which define the stable binding modes identified

during 200 ns of BLUES simulations. Macrostates represent different kinetically stable potential binding modes or structures that we observe, whereas microstates are local, structurally-similar states that may interconvert very rapidly. Using TICA (Time-lagged independent component analysis), we cluster the simulations frames into discrete microstates using k-means clustering. Then, we assign each microstate to a number of macrostates or metastable binding modes, using PCCA (perron-cluster cluster analysis). B) Populations of the two binding modes of ethylbenzene identified during BLUES simulations. C) Calculated RMSD relative to the crystallographic binding mode and the binding mode which is closest to the crystallographic binding mode is represented in red with a minimum RMSD of 0.66 Å. D) In red, we show the binding mode representing the red cluster and in green we show the binding mode representing the green cluster within L99A. The PDB structure of the receptor used to run BLUES simulations is 4W55. Details regarding the tools used for TICA and PCCA approaches can be found in Lim et al 2019 (15).

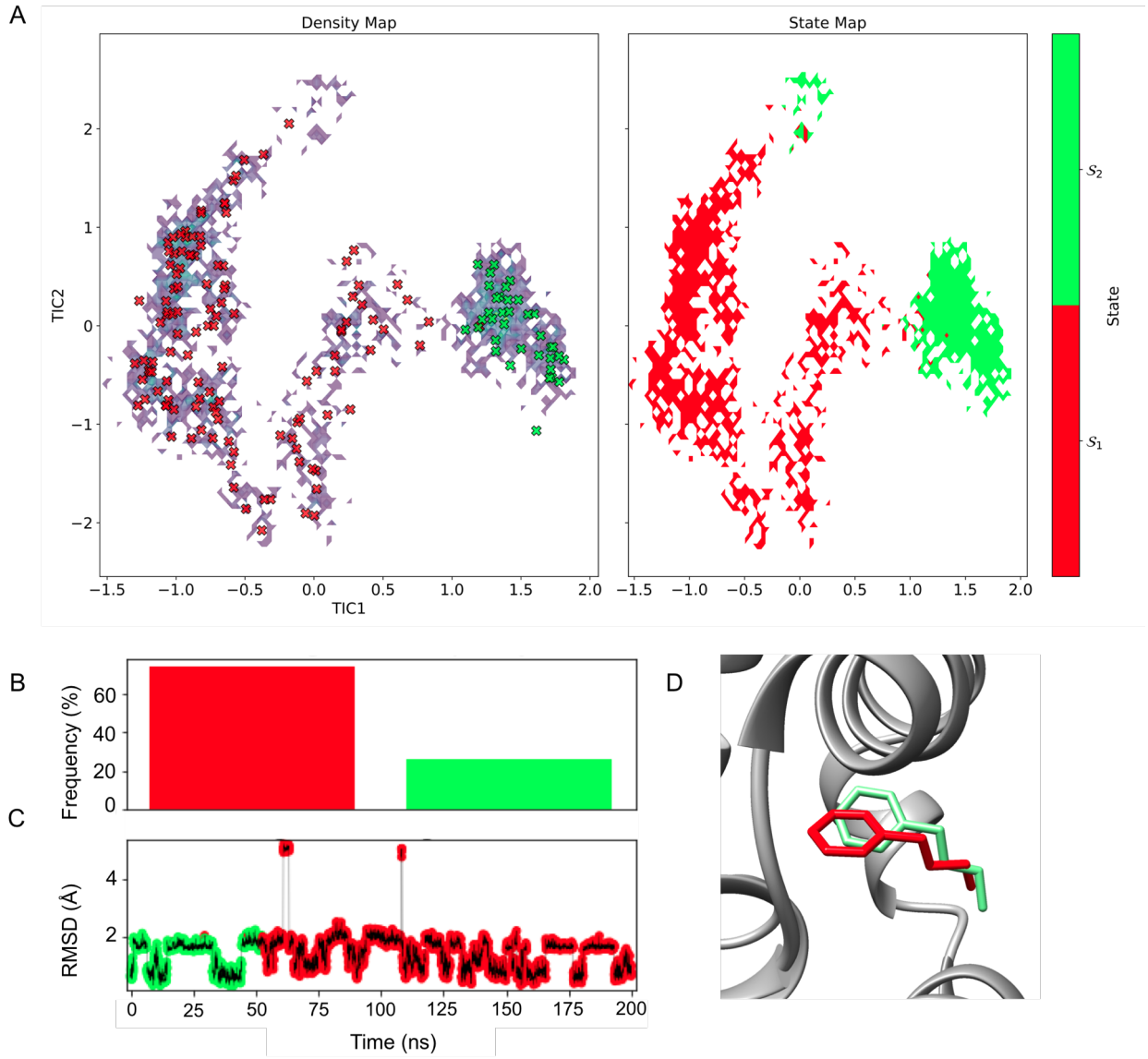

Figure S36. BLUES simulations on L99A complexed to butylbenzene sampled two different binding modes. A) Time-lagged independent component analysis (TICA) plot for binding modes of butylbenzene in L99A using the first two TICA components from our BLUES simulations. Microstates are marked by Xs. We used PCCA to assign microstates to macrostates which define the stable binding modes identified during 200 ns of BLUES simulations. B) Populations of the two binding modes of butylbenzene identified during BLUES simulations. Macrostates represent different kinetically stable potential binding modes or structures that we observe, whereas microstates are local, structurally-similar states that may interconvert very rapidly. Using TICA (Time-lagged independent component analysis), we cluster the simulations frames into discrete microstates using k-means clustering. Then, we assign each microstate to a number of macrostates or metastable binding modes, using PCCA (perron-cluster cluster analysis). C)

Calculated RMSD relative to the crystallographic binding mode and the binding mode which is closest to the crystallographic binding mode is represented in red with a minimum RMSD of 0.8 Å. D) In red, we show the binding mode representing the red cluster and in green we show the binding mode representing the green cluster within L99A. The PDB structure of the receptor used to run BLUES simulations is 4W55. Details regarding the tools used for TICA and PCCA approaches can be found in Lim et al 2019 (15).

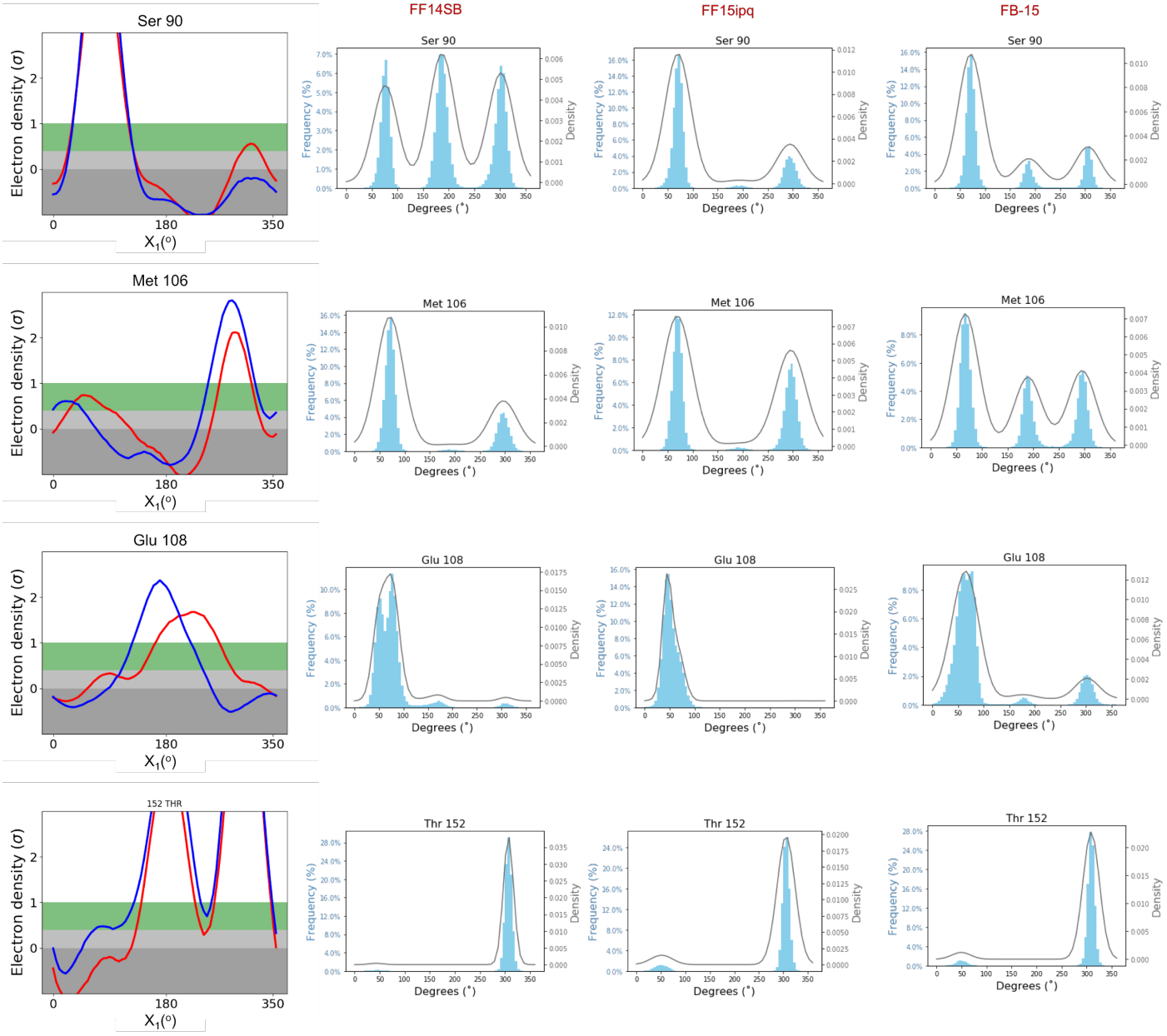

Figure S37. Different rotamer distributions were observed using different AMBER force fields. *Cringer* plots of Ser90, Met106, Glu108, and Thr152 were obtained for 200 ns of MD simulations on apo L99A using: i) AMBER ff14SB protein force field, ii) AMBER ff15ipq protein force field, and iii) AMBER FB-15 protein force field. The rotamer distributions are plotted using Gaussian kernel density estimation. The PDB code used to prepare the apo L99A structures with different protein force fields and run the simulations is 4W51.

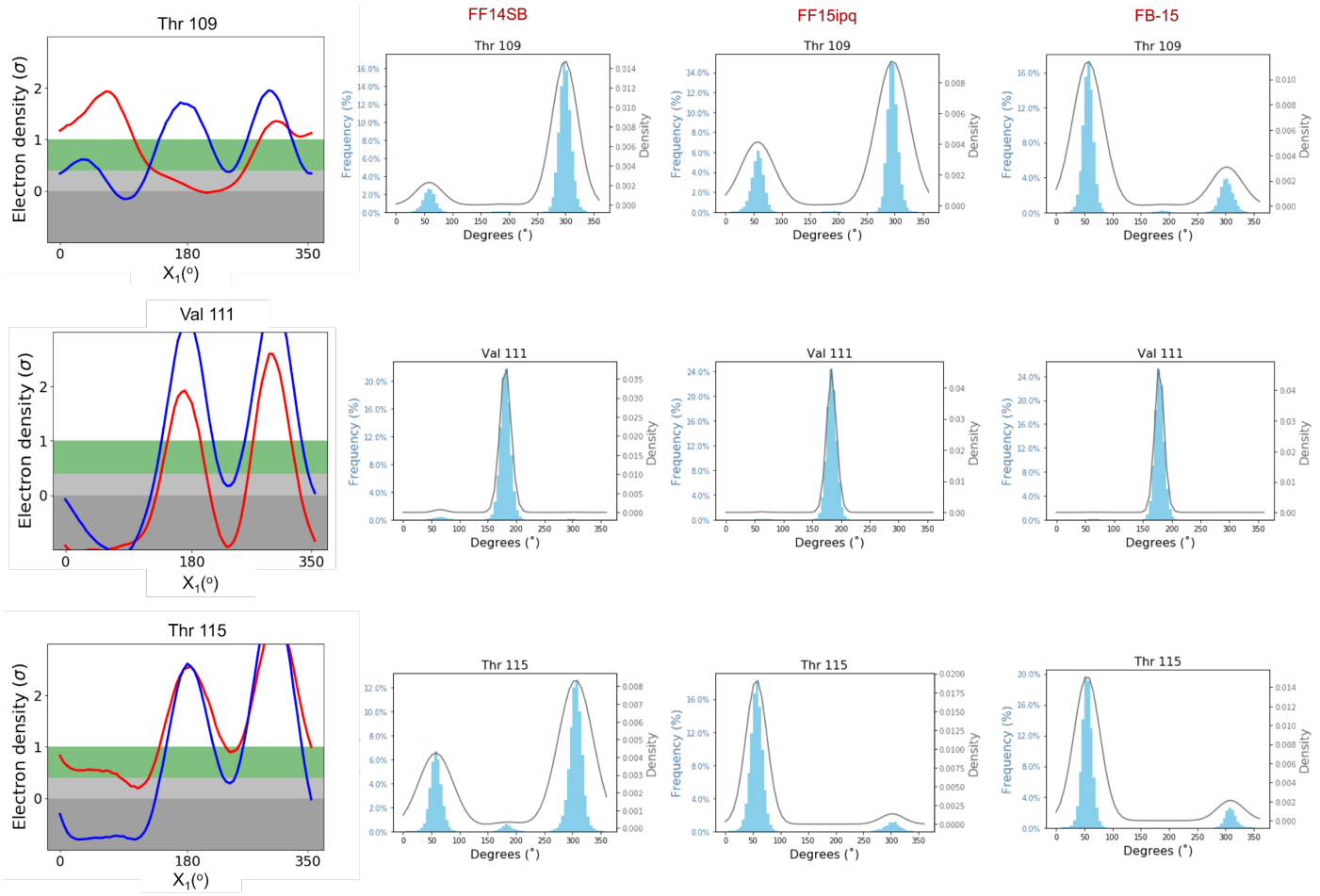

Figure S38. The same rotamers were captured using different AMBER force fields. *Cringers* of Thr109, Val111, and Thr115 were obtained for 200 ns of MD simulations on apo L99A using: i) AMBER ff14SB protein force field, ii) AMBER ff15ipq protein force field, and iii) AMBER FB-15 protein force field. The populations of the rotamers corresponding to each amino acid residue depend on the force field. The rotamer distributions are plotted using Gaussian kernel density estimation. The PDB code used to prepare the apo L99A structures with different protein force fields and run the simulations is 4W51.

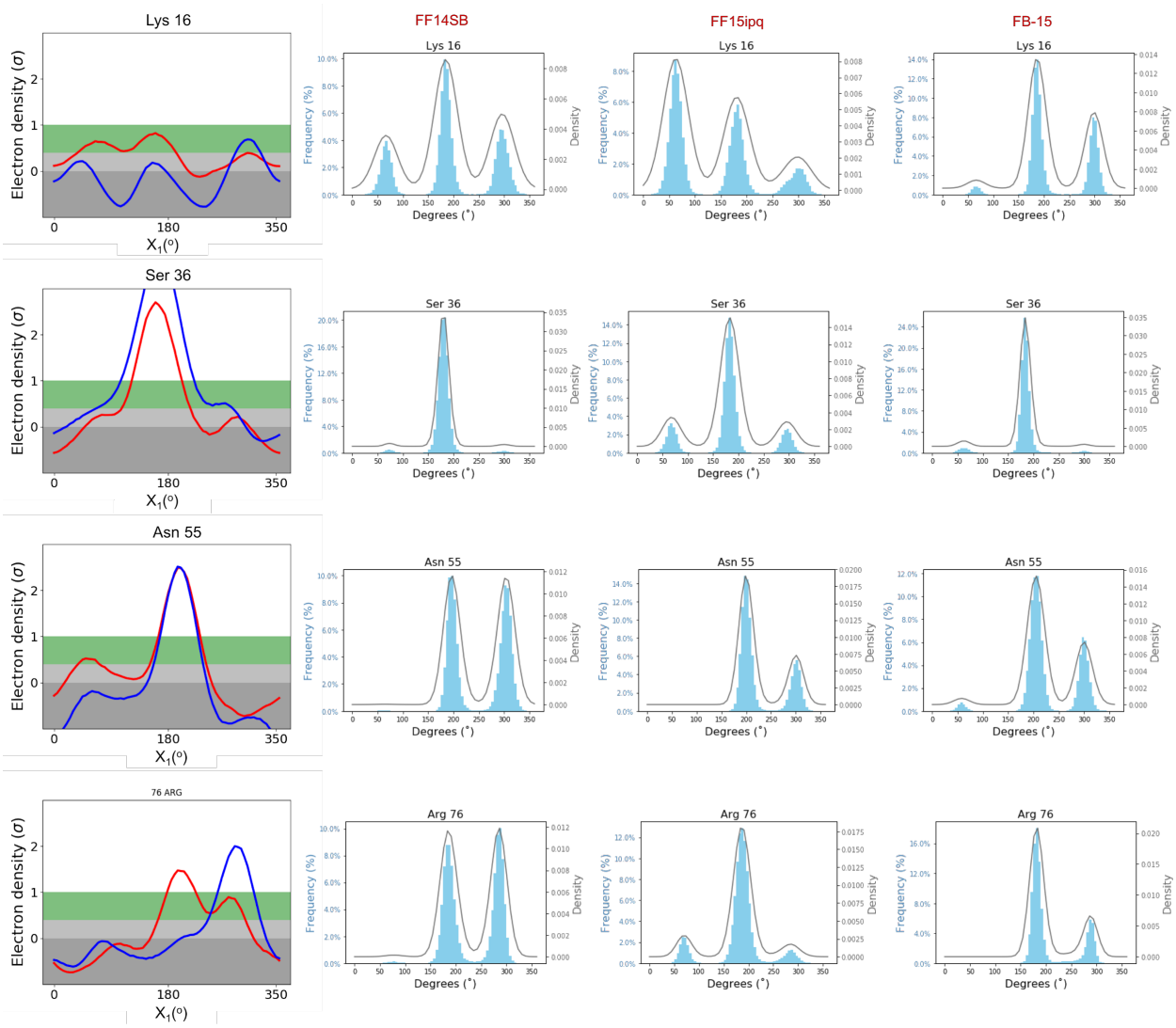

Figure S39. The same rotamers were captured using different AMBER force fields. *Cringers* of Lys16, Ser36, Asn55, and Arg76 were obtained for 200 ns of MD simulations on apo L99A using: i) AMBER ff14SB protein force field, ii) AMBER ff15ipq protein force field, and iii) AMBER FB-15 protein force field. The populations of the rotamers corresponding to each amino acid residue depend on the force field. The rotamer distributions are plotted using Gaussian kernel density estimation. The PDB code used to prepare the apo L99A structures with different protein force fields and run the simulations is 4W51.

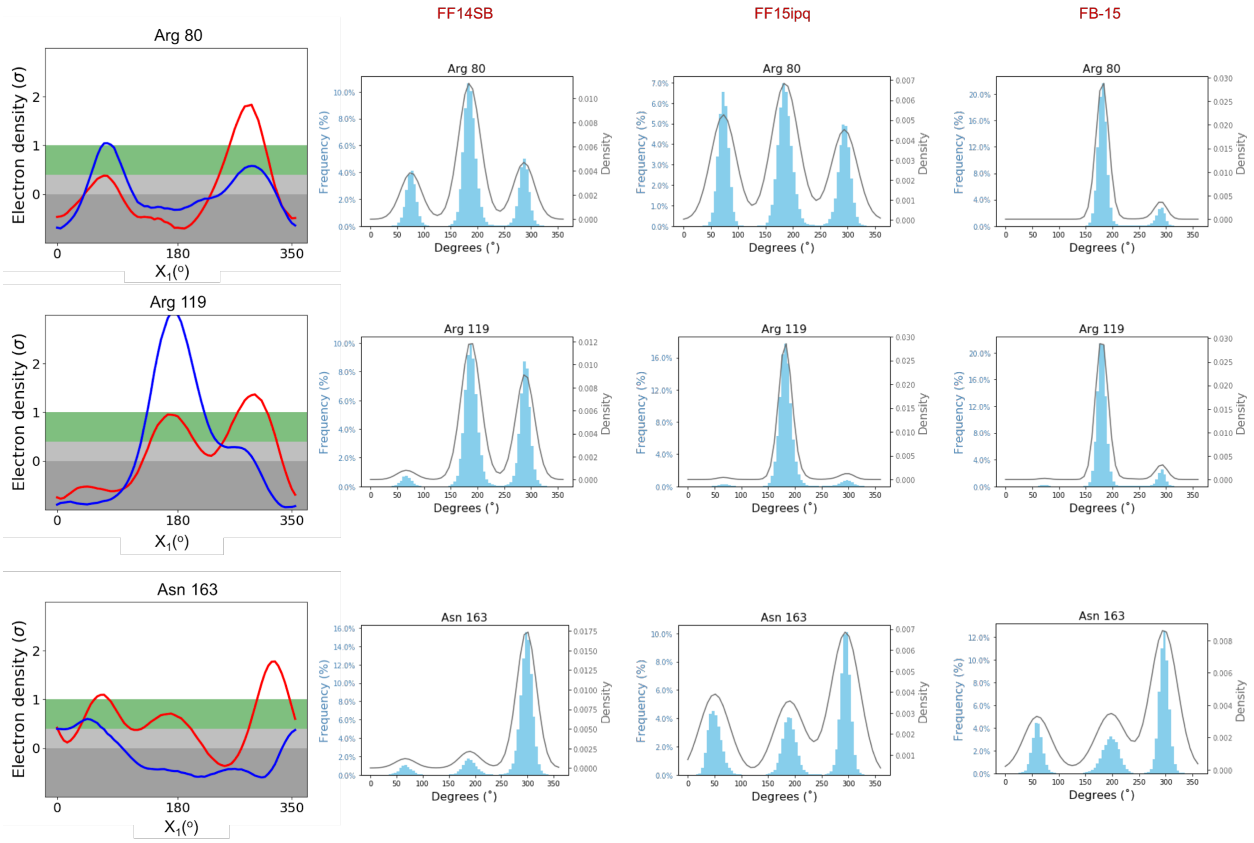

Figure S40. The same rotamers were captured using different AMBER force fields. *Cringers* of Arg80, Arg119, and Asn163 were obtained for 200 ns of MD simulations on apo L99A using: i) AMBER ff14SB protein force field, ii) AMBER ff15ipq protein force field, and iii) AMBER FB-15 protein force field. The populations of the rotamers corresponding to each amino acid residue depend on the force field. The rotamer distributions are plotted using Gaussian kernel density estimation. The PDB code used to prepare the apo L99A structures with different protein force fields and run the simulations is 4W51.

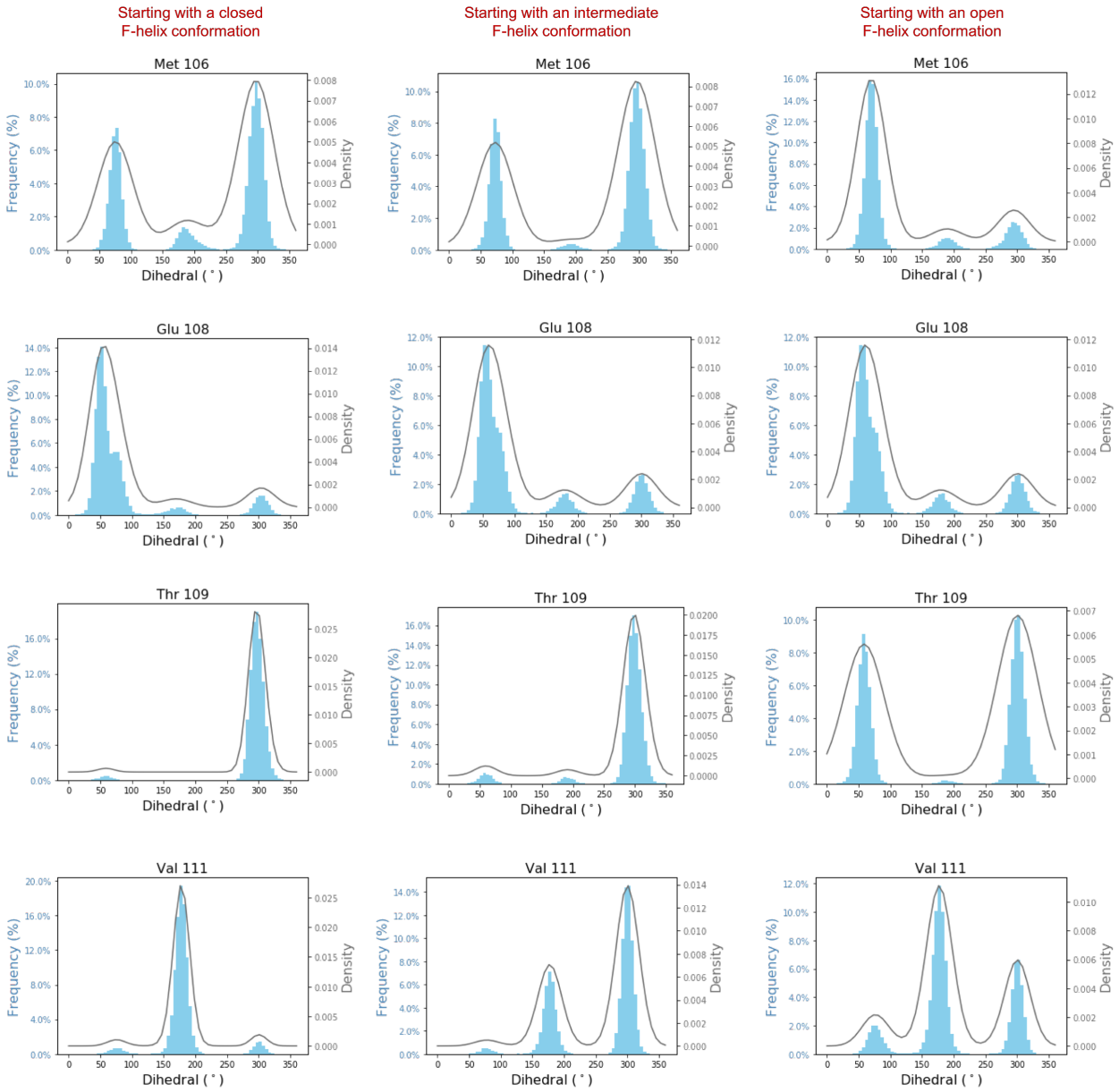

Figure S41. Starting from different F-helix conformations, the rotamers of the same amino acid residue achieve different distributions. *Cringers* of Met106, Glu108, Thr109, and Val111 for o-xylene when starting with: i) a closed F-helix conformation, ii) an intermediate F-helix conformation, and iii) an open F-helix conformation. The rotamers are plotted using Gaussian kernel density estimation. The PDB codes used to prepare L99A with a closed F-helix conformation, L99A with an intermediate F-helix conformation, and L99A with an open F-helix conformation are 4W51, 4w55, and 4W59, respectively.

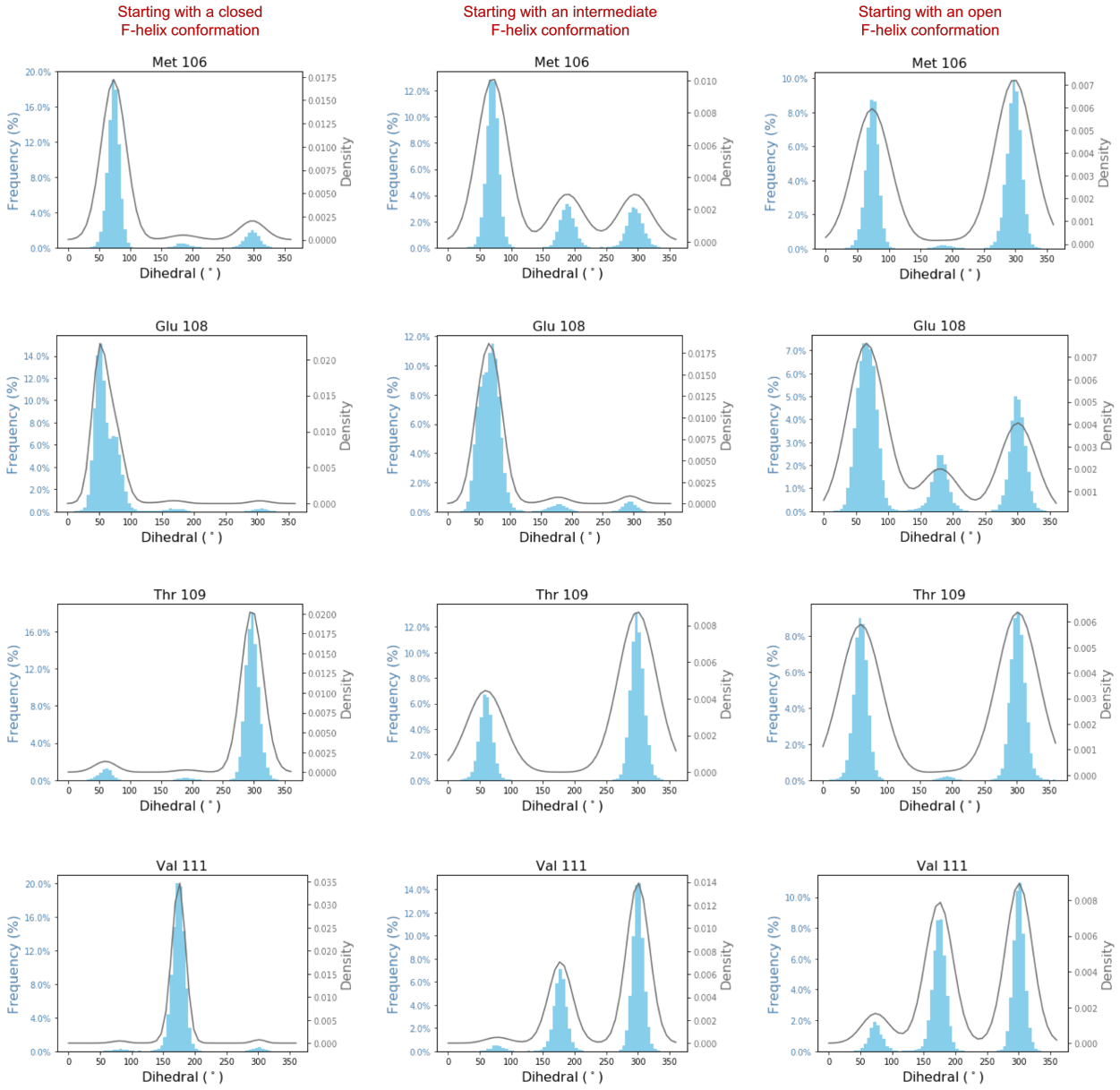

Figure S42. Starting from different F-helix conformations, the rotamers of the same amino acid residue achieve different distributions. *Cringers* of Met106, Glu108, Thr109, and Val111 for p-xylene when starting with: i) a closed F-helix conformation, ii) an intermediate F-helix conformation, and iii) an open F-helix conformation. The rotamers are plotted using Gaussian kernel density estimation. The PDB codes used to prepare L99A with a closed F-helix conformation, L99A with an intermediate F-helix conformation, and L99A with an open F-helix conformation are 4W51, 4w55, and 4W59, respectively.

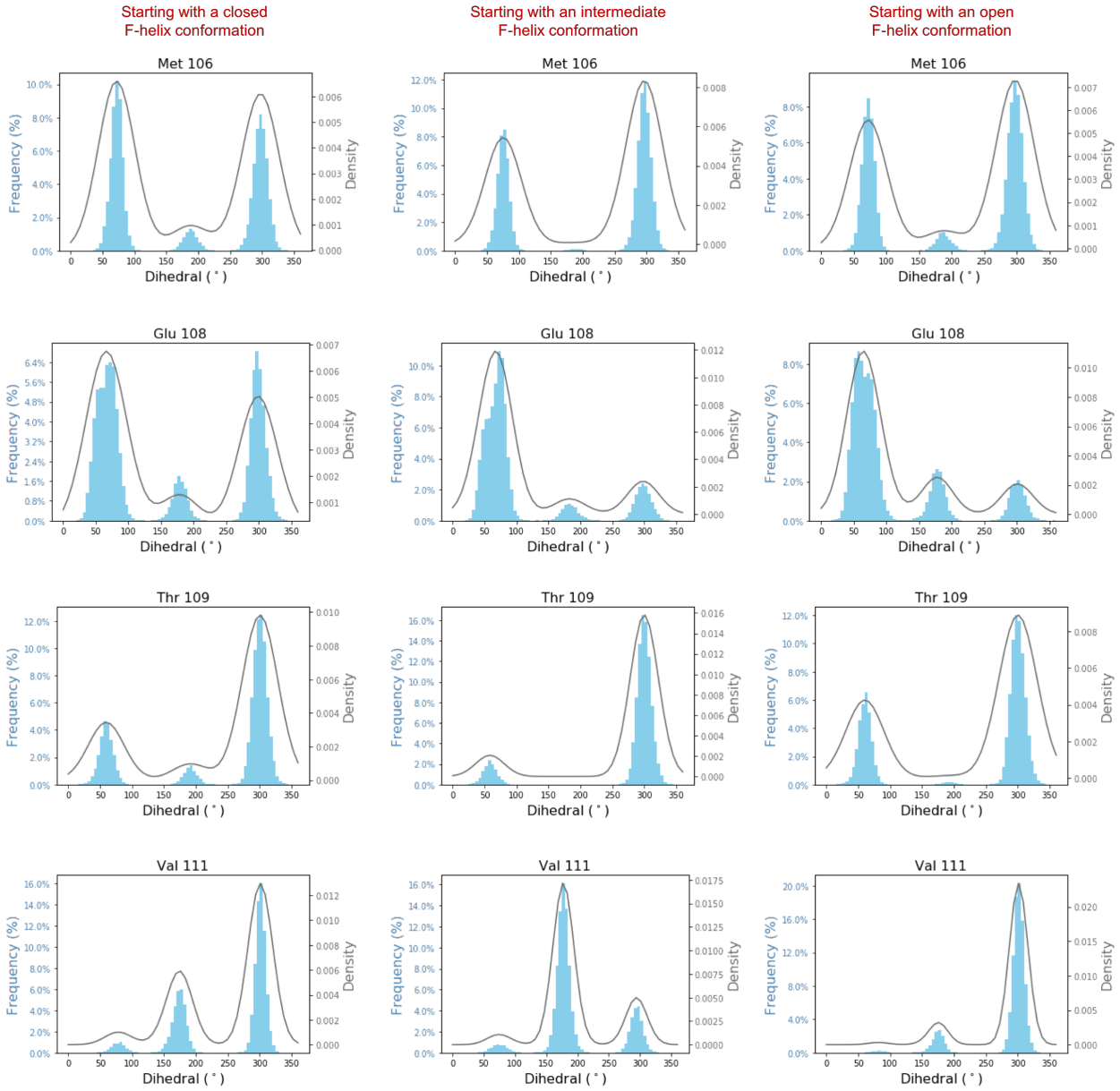

Figure S43. Starting from different F-helix conformations, the rotamers of the same amino acid residue achieve different distributions. *Cringers* of Met106, Glu108, Thr109, and Val111 for 3-iodotoluene when starting with: i) a closed F-helix conformation, ii) an intermediate F-helix conformation, and iii) an open F-helix conformation. The rotamers are plotted using Gaussian kernel density estimation. The PDB codes used to prepare L99A with a closed F-helix conformation, L99A with an intermediate F-helix conformation, and L99A with an open F-helix conformation are 4W51, 4w55, and 4W59, respectively.

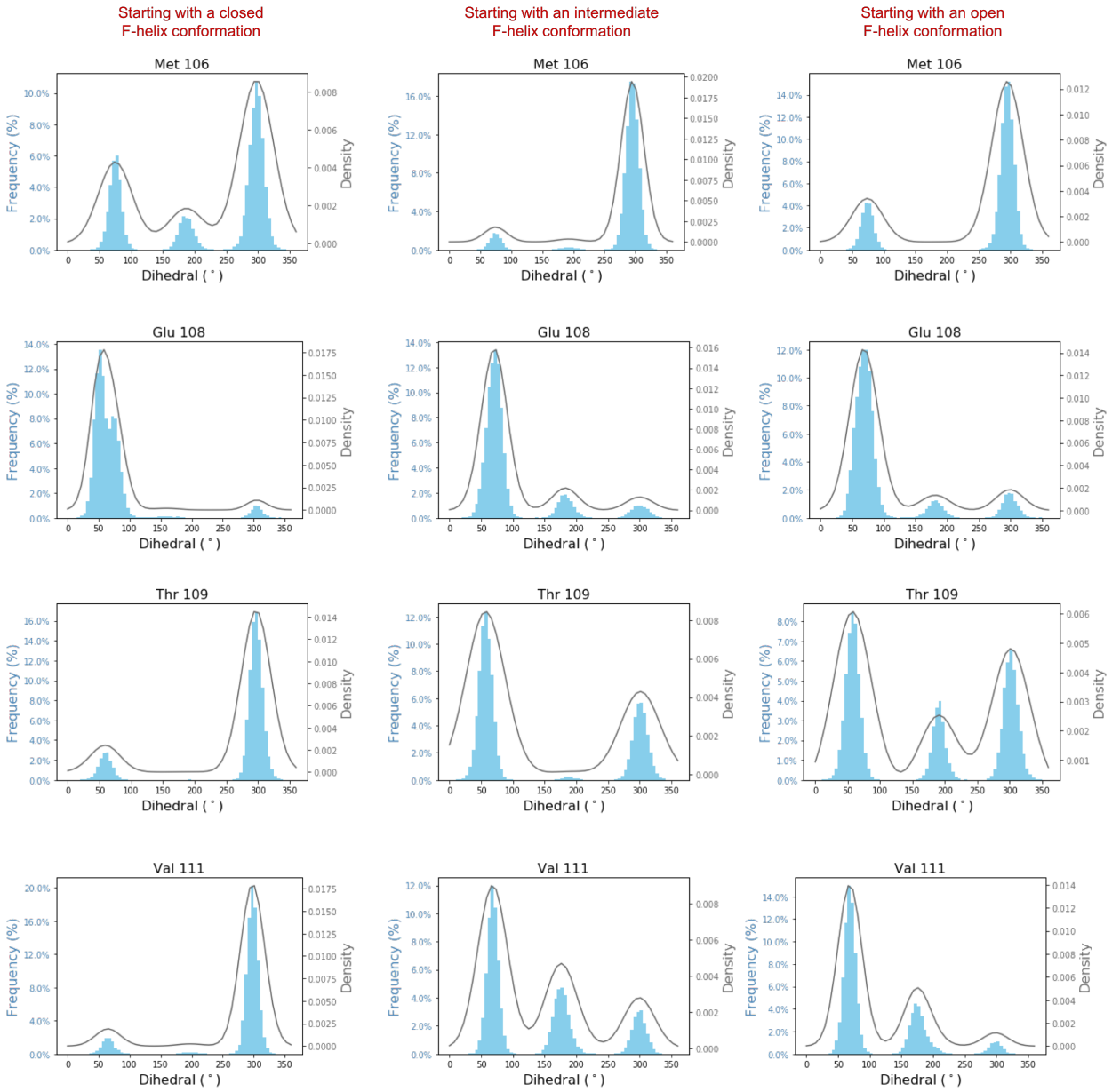

Figure S44. Starting from different F-helix conformations, the rotamers of the same amino acid residue achieve different distributions. Cringers of Met106, Glu108, Thr109, and Val111 for hexylbenzene when starting with: i) a closed F-helix conformation, ii) an intermediate F-helix conformation, and iii) an open F-helix conformation. The rotamers are plotted using Gaussian kernel density estimation. The PDB codes used to prepare L99A with a closed F-helix conformation, L99A with an intermediate F-helix conformation, and L99A with an open F-helix conformation are 4W51, 4w55, and 4W59, respectively.

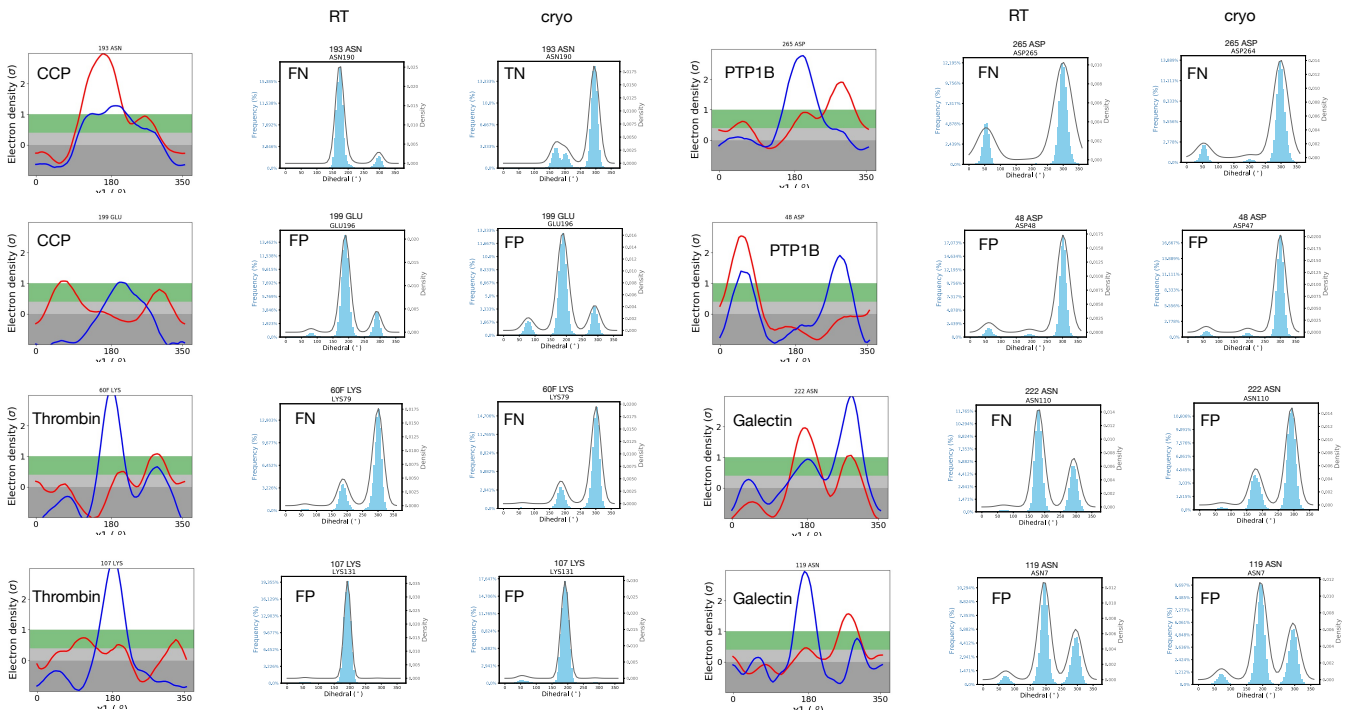

Figure S45. Examples of false positives and false negatives for each . "False positives" are results where the Ringer-*Cringer* comparison shows that MD data agree with cryo data, but disagree with RTX data. "False negatives" are results where the Ringer-*Cringer* comparison shows that MD data agree with RTX data, but disagree with cryo data.

Table S5. Ringer-Cringer comparison reveals high proportion of false positives (FP) and false negatives (FN) of total residues per protein (that have a Chi angle).

Protein	FP (%)	FN (%)	Total (%)
Thrombin	11.5	6.1	*17.6*
PTP1B	6.2	5.8	*12.0*
Galectin-3	2.6	1.7	*4.3*
CCP	0.9	3.4	*4.3*

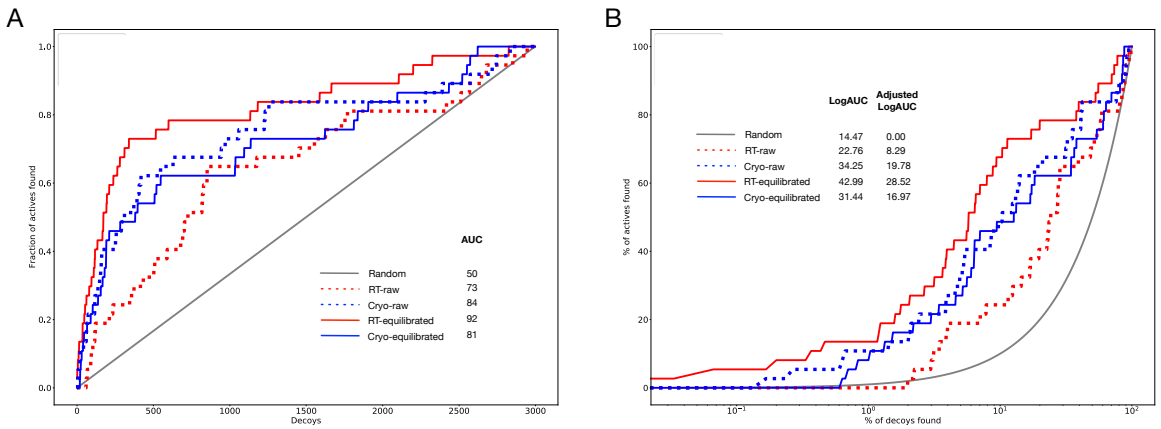

Figure S46. The choice of the protein structure impacts docking. (A) AUC and (B) adjusted LogAUC enrichment plots from docking known thrombin binders against property-matched DUD-E decoys using OEdock. The raw RT and cryo structures and equilibrated structures extracted from MD simulations (after 50 ns) were used.

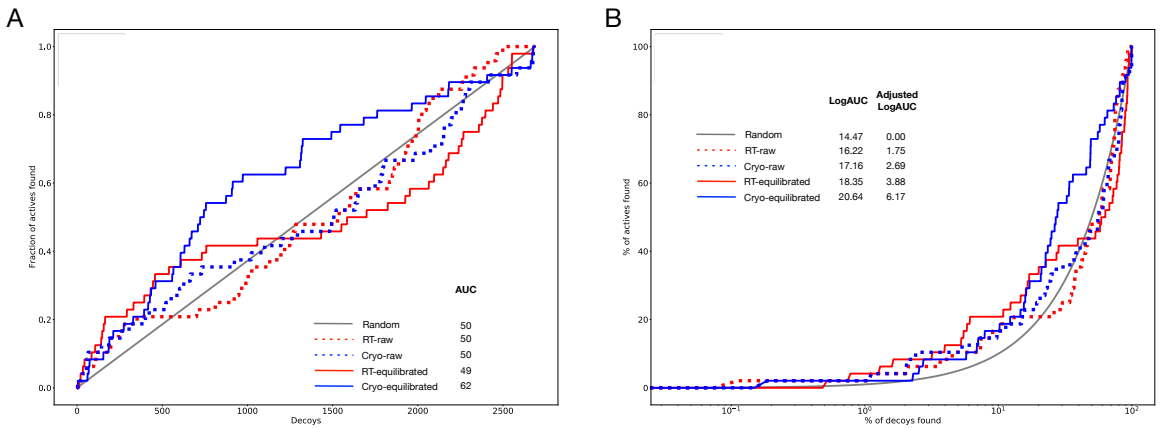

Figure S47. The choice of the protein structure impacts docking. (A) AUC and (B) adjusted LogAUC enrichment plots from docking known PTP1B binders against property-matched DUD-E decoys using OEDock. The raw RT and cryo structures and equilibrated structures extracted from MD simulations (after 50 ns) were used. Performance is not dramatically different here, nor dramatically better than random, though equilibrated structures have modestly better early enrichment.

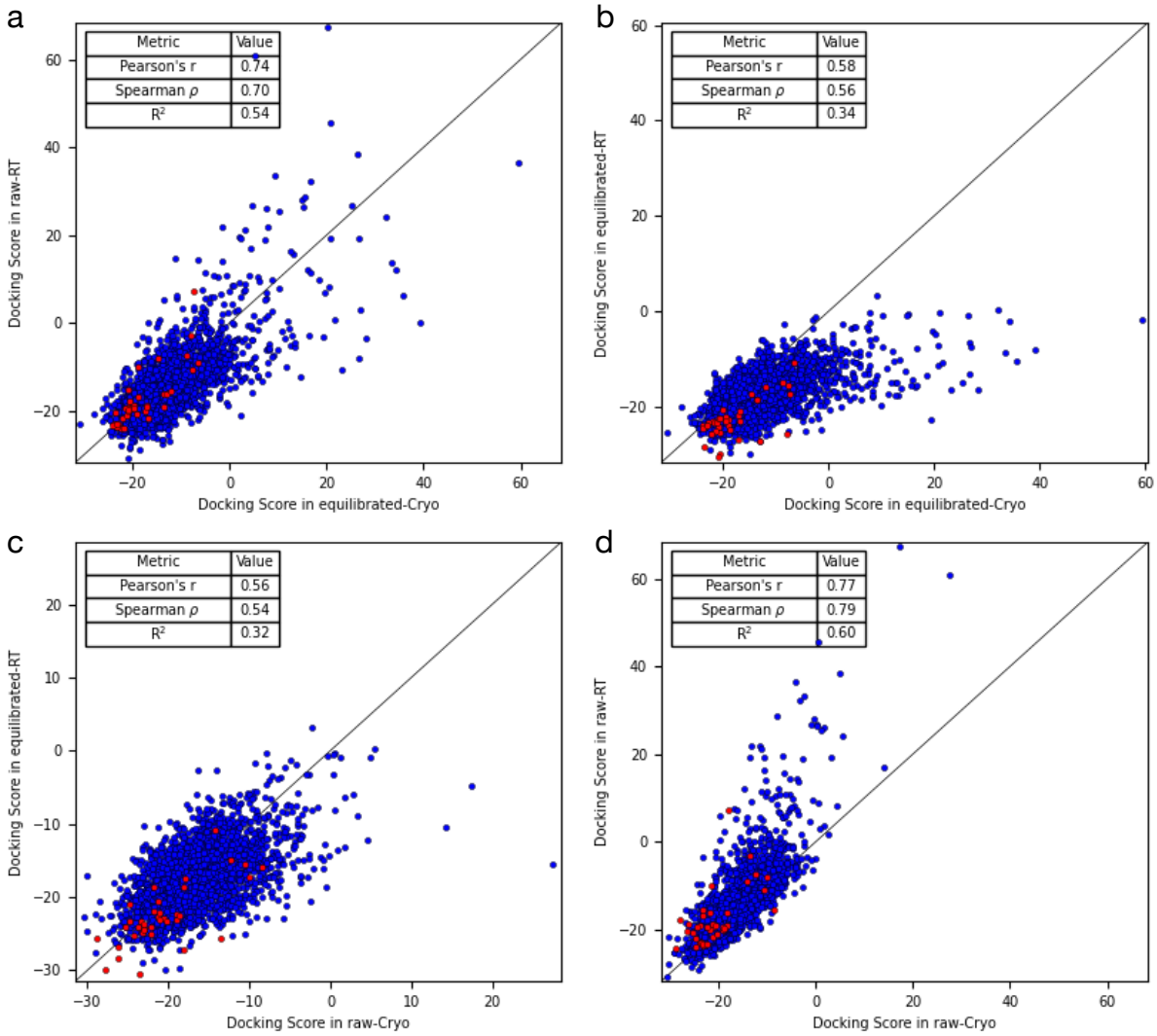

Figure S48. The correlation coefficients show that OEDock scores of the different thrombin structure combinations are positively correlated. Correlation coefficients of the docking scores of thrombin compounds when docked in different structures using OEDock. The plots represent the scores of the docked compounds in structure X vs structure Y with X and Y representing one of the following structures: i) raw RT structure, ii) raw cryo structure, iii) equilibrated RT structure, iv) equilibrated cryo structure. We use "equilibrated" structures in the Figure above to refer to the structures extracted after 50 ns of MD simulations. R^2 is Pearson's correlation coefficient. Known binders are shown in red. In general, the choice of structure impacts docking score substantially and though scores are correlated, the structure plays a major role in the details of the score.

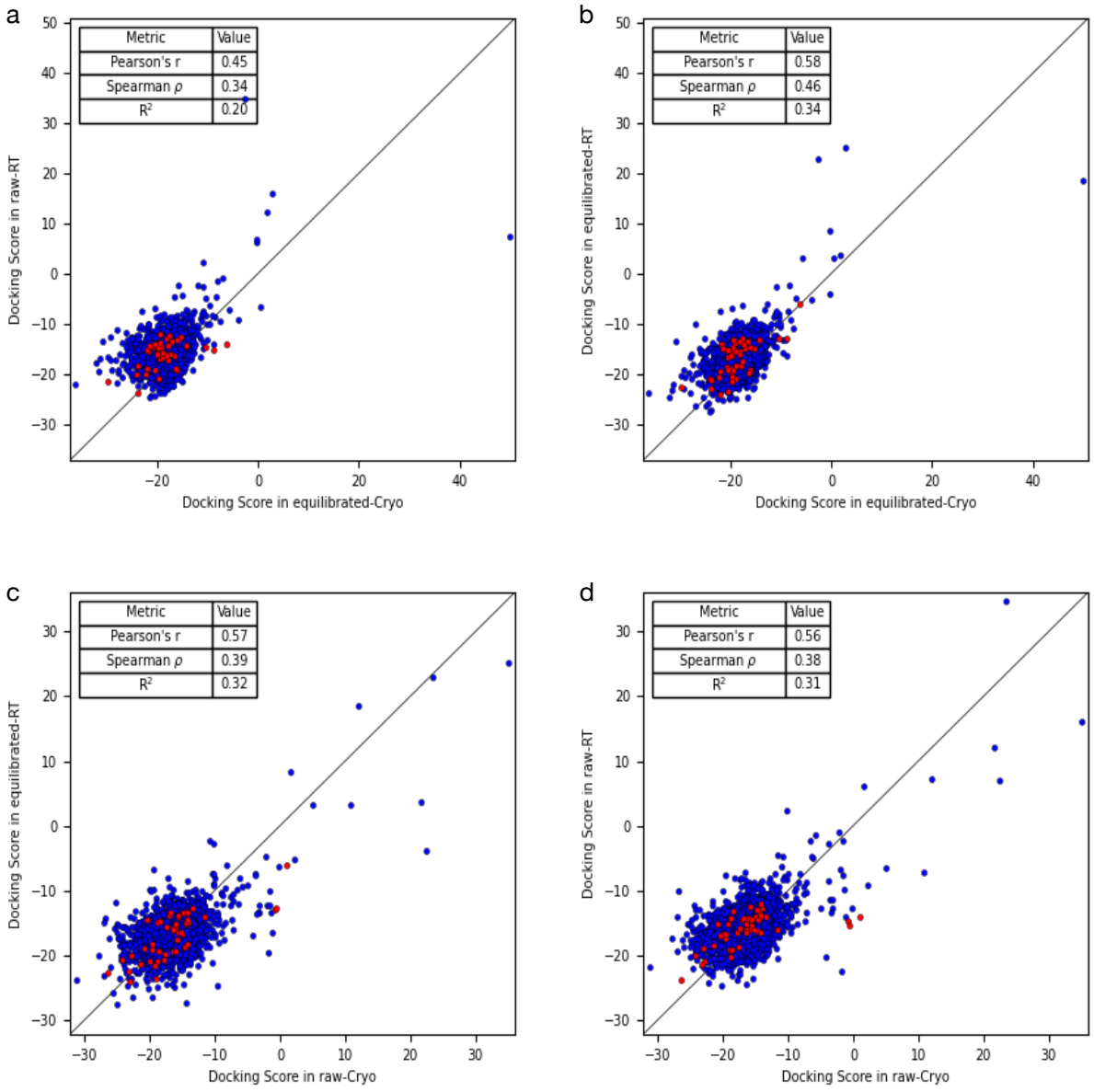

Figure S49. The correlation coefficients show that OEDock scores of the different PTP1B structure combinations are positively correlated. Correlation coefficients of the docking scores of thrombin compounds when docked in different structures using OEDock. The plots represent the scores of the docked compounds in structure X vs structure Y with X and Y representing one of the following structures: i) raw RT structure, ii) raw cryo structure, iii) equilibrated RT structure, iv) equilibrated cryo structure. We use "equilibrated" structures in the Figure above to refer to the structures extracted after 50 ns of MD simulations. R^2 is Pearson's correlation coefficient. Known binders are shown in red. In general, scores are relatively correlated but the choice of structure still plays a role in the exact details of the score.

Table S6. Experimental and calculated relative binding affinities of thrombin complexes. Relative binding free energies ($\Delta\Delta G_{calc}$) and their respective uncertainties (δ_{calc}) for 9 perturbations (11 unique ligands). Across all cryo structures, the average error is 0.46 kcal/mol, and the median is 0.38 kcal/mol. Across all RT structures, the average error is 0.48 kcal/mol, and the median is 0.41 kcal/mol. Color coding: blue = cryo; red = RT.

Perturbation	$\Delta\Delta G_{calc}$ (kcal/mol)	δ_{calc} (kcal/mol)	$\Delta\Delta G_{exp}$ (kcal/mol)	Error (|exp-calc|) (kcal/mol)
1	0.17	0.12	-0.14	0.31
	-0.46	0.19	-0.14	0.32
2	0.78	0.30	0.03	0.75
	0.52	0.22	0.03	0.49
3	0.67	0.26	-0.10	0.77
	0.28	0.17	-0.10	0.38
4	-0.96	0.67	-0.38	0.58
	-0.08	0.71	-0.38	0.30
5	0.48	0.76	0.72	0.24
	0.09	0.43	0.72	0.63
6	0.56	0.24	0.24	0.32
	0.50	0.18	0.24	0.26
7	1.43	0.17	0.77	0.66
	1.78	0.32	0.77	1.01
8	0.85	0.38	0.60	0.25
	1.02	0.31	0.60	0.42
9	-0.39	0.29	0.02	0.41
	-0.27	0.30	0.02	0.29

Table S7. Experimental and calculated relative binding affinities of PTP1B complexes. Relative binding free energies ($\Delta\Delta G_{calc}$) and their respective uncertainties (δ_{calc}) for 9 perturbations (11 unique ligands). Across all cryo structures, the average error is 1.60 kcal/mol, and the median is 0.68 kcal/mol. Across all RT structures, the average error is 1.68 kcal/mol, and the median is 1.58 kcal/mol. Color coding: blue = cryo; red = RT.

Perturbation	$\Delta\Delta G_{calc}$ (kcal/mol)	δ_{calc} (kcal/mol)	$\Delta\Delta G_{exp}$ (kcal/mol)	Error (|exp-calc|) (kcal/mol)
1	0.30	0.61	-0.29	0.59
	0.07	0.19	-0.29	0.36
2	0.44	1.00	0.03	0.41
	-0.47	0.54	0.03	0.50
3	0.69	1.39	-0.10	0.79
	0.28	0.50	-0.10	0.38
4	-0.87	1.5	-4.72	3.85
	-2.90	0.39	-4.72	1.82
5	-0.08	2.14	-2.25	2.17
	2.34	0.56	-2.25	4.59
6	1.16	0.52	-0.42	1.58
	0.10	0.54	-0.42	0.52
7	1.69	0.80	3.67	1.98
	0.28	0.38	3.67	3.39
8	2.07	1.39	1.87	0.20
	1.19	0.60	1.87	0.68
9	0.31	0.89	-3.26	3.57
	-1.08	1.54	-3.26	2.18

References

1. L. Liu, W. A. Baase and B. W. Matthews, *J Mol Biol*, 2009, **385**, 595-605.
2. S. K. Burley, H. M. Berman, C. Christie, J. Duarte, Z. Feng, J. Westbrook, J. Young and C. Zardecki, *Protein Sci*, 2017.
3. S. C. Gill, N. M. Lim, P. B. Grinaway, A. S. Rustenburg, J. Fass, G. A. Ross, J. D. Chodera and D. L. Mobley, *J Phys Chem B*, 2018, **122**, 5579-5598.
4. K. A. Feenstra, B. Hess and H. J. C. Berendsen, *Journal of Computational Chemistry*, 1999, **20**, 786-798.
5. C. W. Hopkins, S. Le Grand, R. C. Walker and A. E. Roitberg, *J Chem Theory Comput*, 2015, **11**, 1864-1874.
6. P. Eastman, M. S. Friedrichs, J. D. Chodera, R. J. Radmer, C. M. Bruns, J. P. Ku, K. A. Beauchamp, T. J. Lane, L. P. Wang, D. Shukla, T. Tye, M. Houston, T. Stich, C. Klein, M. R. Shirts and V. S. Pande, *J Chem Theory Comput*, 2013, **9**, 461-469.
7. J. Wang, R. M. Wolf, J. W. Caldwell, P. A. Kollman and D. A. Case, *J Comput Chem*, 2004, **25**, 1157-1174.
8. K. T. Debiec, D. S. Cerutti, L. R. Baker, A. M. Gronenborn, D. A. Case and L. T. Chong, *J Chem Theory Comput*, 2016, **12**, 3926-3947.
9. L. P. Wang, K. A. McKiernan, J. Gomes, K. A. Beauchamp, T. Head-Gordon, J. E. Rice, W. C. Swope, T. J. Martínez and V. S. Pande, *J Phys Chem B*, 2017, **121**, 4023-4039.
10. K. H. Burley, S. C. Gill, N. M. Lim and D. L. Mobley, *J Chem Theory Comput*, 2019, **15**, 1848-1862.
11. O. Trott and A. J. Olson, *J Comput Chem*, 2010, **31**, 455-461.
12. G. M. Morris, R. Huey, W. Lindstrom, M. F. Sanner, R. K. Belew, D. S. Goodsell and A. J. Olson, *J Comput Chem*, 2009, **30**, 2785-2791.
13. N. T. Nguyen, T. H. Nguyen, T. N. H. Pham, N. T. Huy, M. V. Bay, M. Q. Pham, P. C. Nam, V. V. Vu and S. T. Ngo, *J Chem Inf Model*, 2020, **60**, 204-211.
14. M. McGann, *J Chem Inf Model*, 2011, **51**, 578-596.
15. M. D. Eldridge, C. W. Murray, T. R. Auton, G. V. Paolini and R. P. Mee, *J Comput Aided Mol Des*, 1997, **11**, 425-445.
16. B. Baum, M. Mohamed, M. Zayed, C. Gerlach, A. Heine, D. Hangauer and G. Klebe, *Journal of Molecular Biology*, 2009, **390**, 56-69.
17. D. P. Wilson, Z. K. Wan, W. X. Xu, S. J. Kirincich, B. C. Follows, D. Joseph-McCarthy, K. Foreman, A. Moretto, J. Wu, M. Zhu, E. Binnun, Y. L. Zhang, M. Tam, D. V. Erbe, J. Tobin, X. Xu, L. Leung, A. Shilling, S. Y. Tam, T. S. Mansour and J. Lee, *Journal of Medicinal Chemistry*, 2007, **50**, 4681-4698.
18. M. K. Gilson, T. Liu, M. Baitaluk, G. Nicola, L. Hwang and J. Chong, *Nucleic Acids Research*, 2016, **44**, D1045-1053.
19. M. M. Mysinger, M. Carchia, J. J. Irwin and B. K. Shoichet, *Journal of Medicinal Chemistry*, 2012, **55**, 6582-6594.
20. N. Huang, B. K. Shoichet and J. J. Irwin, *Journal of Medicinal Chemistry*, 2006, **49**, 6789-6801.
21. J. A. Maier, C. Martinez, K. Kasavajhala, L. Wickstrom, K. E. Hauser and C. Simmerling, *Journal of Chemical Theory and Computation*, 2015, **11**, 3696-3713.
22. Y. Qiu, D. Smith, S. Boothroyd, H. Jang and J. Wagner, *ChemRxiv.* , 2020.

23. D. Seeliger and B. L. de Groot, *Biophysj*, 2010, **98**, 2309-2316.
24. V. Gapsys, S. Michielssens, D. Seeliger and B. L. de Groot, *Journal of Computational Chemistry*, 2015, **36**, 348-354.
25. M. Parrinello and A. Rahman, *Journal of Applied Physics*, 1981, **52**, 7182-7190.
26. B. Hess, H. Bekker, H. Berendsen and J. Fraaije, *Journal of Computational Chemistry*, 1997, **18**, 1463-1472.
27. V. Gapsys, D. Seeliger and B. L. de Groot, *Journal of Chemical Theory and Computation*, 2012, **8**, 2373-2382.
28. M. D. Winn, C. C. Ballard, K. D. Cowtan, E. J. Dodson, P. Emsley, P. R. Evans, R. M. Keegan, E. B. Krissinel, A. G. Leslie, A. McCoy, S. J. McNicholas, G. N. Murshudov, N. S. Pannu, E. A. Potterton, H. R. Powell, R. J. Read, A. Vagin and K. S. Wilson, *Acta Crystallogr D Biol Crystallogr*, 2011, **67**, 235-242.
29. P. T. Lang, H. L. Ng, J. S. Fraser, J. E. Corn, N. Echols, M. Sales, J. M. Holton and T. Alber, *Protein Sci*, 2010, **19**, 1420-1431.
30. N. M. Lim, L. Wang, R. Abel and D. L. Mobley, *J Chem Theory Comput*, 2016, **12**, 4620-4631.